

# Transport in Ion Dense Media and Recyclable Polymers

by

Yael Petel

B.Sc., Ben Gurion University of the Negev, 2010

M.Sc., Weizmann Institute of Science, 2014

A THESIS SUBMITTED IN PARTIAL FULFILLMENT OF  
THE REQUIREMENTS FOR THE DEGREE OF

DOCTOR OF PHILOSOPHY

in

The Faculty of Graduate and Postdoctoral Studies

(Chemistry)

THE UNIVERSITY OF BRITISH COLUMBIA

(Vancouver)

August 2020

© Yael Petel, 2020

---

The following individuals certify that they have read, and recommend to the Faculty of Graduate and Postdoctoral Studies for acceptance, the dissertation entitled:

Transport in Ion Dense Media and Recyclable Polymers

submitted by Yael Petel in partial fulfilment of the requirements for  
the degree of Doctor of Philosophy  
in Chemistry

**Examining Committee:**

Carl A. Michal, Associate Professor, Physics and Astronomy, UBC

Supervisor

Suzana K. Straus, Professor, Chemistry, UBC

Supervisory Committee Member

Gren N. Patey, Professor, Chemistry, UBC

University Examiner

Edmond Cretu, Associate Professor, Electrical & Computer Engineering, UBC

University Examiner

Louis A. Madsen, Professor, Chemistry, Virginia Tech

External Examiner

**Additional Supervisory Committee Members:**

Michael O. Wolf, Professor, Chemistry, UBC

Supervisory Committee Member

Andrew W. MacFarlane, Associate Professor, Chemistry, UBC

Supervisory Committee Member

# Abstract

In order to guide the development of innovative materials and their applications, a better understanding of the mechanisms that drive their unique properties is necessary. It has been widely observed that the well-established theory of driven and self-diffusion in highly diluted solutions does not directly apply to higher concentrations. The deviation from the existing theory of transport in high concentration materials is responsible, in part, for some interesting phenomena that present opportunities for innovative applications. Due to a limited number of direct measurement techniques, the mechanisms behind these phenomena remain unknown.

In this dissertation, nuclear magnetic resonance (NMR) is deployed as a tool to track the migration of magnetically visible species in complex systems. We track the transport of chromophores in electro-optical devices that can change their light-transmission properties with the application of voltage. We investigate room temperature ionic liquids and electrolyte salts in piezoionic materials, which are the basis for artificial nerves and muscles. Finally, we explore the initiating factors of crosslinker diffusion in vitrimers, a class of polymers that presents an opportunity for truly recyclable plastics.

We use the well-established technique of pulsed field gradient NMR (PFG-NMR) to measure self-diffusion and extend our measurements to electrophoretic mobility by using a new, low-cost, home-built electrophoretic NMR (eNMR) probe. eNMR development still faces a variety of application challenges. We overcome some of them by setting the driven

diffusion in a direction perpendicular to the majority of undesired flows such as convection currents or bubbles. Using this new probe, we successfully measure electrophoretic mobilities of individual ions which accurately predict conductivities in concentrated solutions.

By measuring both driven and self-diffusion in a variety of materials, we explain some of the transport mechanisms that are behind unique material behaviours. In all the systems investigated, we find that some interaction between the ions, solvent, polymer, or a combination of the three, create interesting phenomena that alter the description of diffusion and mobility from known theory.

# Lay Summary

In order to help guide the development of new materials, we must obtain a better understanding of the mechanisms behind unique material properties. One of the drivers of the unique properties in artificial muscles, electro-optical devices and recyclable polymers, is molecular transport. One difficulty of investigating molecular transport in these unique materials is that we cannot look inside them while they are being used in devices. Nuclear magnetic resonance (NMR) is a tool that can change that; similarly to how an MRI can obtain images of living people to see what is inside, NMR can “look” inside materials, and track how the molecules move inside while a device is operating. Using NMR, we can learn how molecular transport influences the properties of these materials.

My research focuses on the development of this method, extending its ability, and enabling measurements of transport in new materials.

# Preface

Every single part of this dissertation was done with help, supervision and support from Dr. Carl A. Michal.

The home-built PFG self-diffusion probe and resonance driver circuit used in chapter 4-7 were originally built by Tso and Michal [1] and improved by Michan [2]. I have repaired and improved the gradient coil of the probe, increasing the maximal pulse field gradient strength by 17.8%. The self-diffusion pulse sequences were written by Carl Michal and Alison Michan.

The eNMR probe described in chapter 3 and used in chapter 5 was designed and built by me. The eNMR sample holder was designed and built by me. The applied voltage driving circuit was designed by Carl Michal and built by me. The eNMR pulse sequences and the connected micro-controller program were written by me.

Chapter 4 of this dissertation is based on the published paper: [3] V. Woehling, G.T.M. Nguyen, C. Plesse, Y. Petel, Y. Dobashi, J.D.W. Madden, C.A. Michal and F. Vidal, *Multifunctional Materials*, 2, 045002 (2019) <https://doi.org/10.1088/2399-7532/ab56a2> Figures 4.1, 4.2 and 4.8 are used with permission from Woehling *et al.* (2019) of which I am an author. In this work, the experiments were suggested by Carl Michal and Giao T. M. Nguyen of Université de Cergy-Pontoise. Samples were all prepared by Vincent Woehling of Université de Cergy-Pontoise. All NMR experiments were performed and analyzed by me. Carl Michal and I developed the data interpretation together.

Chapter 5 of this dissertation is a collaboration between the Michal lab and Madden group of Electrical Engineering at UBC. The ideas for these experiments are a result of an ongoing discussion between all collaborators. All samples were prepared by Yuta Dobashi and me. The vast majority of voltage measurements presented in this dissertation were done by Yuta. All NMR and eNMR experiments were performed and analyzed by me. Great discussions between all collaborators have led to the mechanism descriptions in this chapter. Viscosity measurements were done by me with the help of Anindya Lal Roy from Dr. Konrad Walus's lab at Quantum Matter Institute, UBC. The experimental work presented in this chapter was done during 2018 and presented in a conference on April 2019. A similar lithium conduction mechanism was suggested in a research paper from another group, published in April 2019 [4], including computational work and conductivity data. We were not aware of this paper until the final stages of this dissertation preparation and reached a similar suggested mechanism independently. We believe our experimental work, which directly measures lithium mobility, strengthens the conclusions reached by both groups.

Chapter 6 was done in collaboration with SWITCH Materials Inc. All sample materials were prepared by Dr. Glen Bremner of SWITCH Materials Inc. All NMR experiments and analysis were done by me. The applied voltage set-up was designed and constructed by me with the help of Carl Michal. Measurements of transitions time for the optical filters that are presented in Table 6.2 were done by Dr. Glen Bremner. Interpretation of the data was done by me and Carl Michal, with consultation from SWITCH Materials Inc.

Chapter 7 of this dissertation is a collaboration between the Michal lab and the Wolf group of Chemistry at UBC. The idea for the initial experiments came from Taylor D. Wright and his advisor, Dr. Michael Wolf. All samples have been synthesized by Taylor and the procedure has been published in [5]. Schemes 7.1, 7.2, A.1 and Figure 7.7 are used

## *Preface*

---

with permission from Taylor D. Wright. All NMR experiments were performed by me. Sample preparation and sealing have been done by me with assistance from Taylor. All interpretation of the data has been done by me and Carl Michal, with discussions with Taylor and Dr. Wolf leading to further suggested experiments.

To help produce the final version of this dissertation, comments to the draft have been made by committee members Dr. Suzana Straus and Dr. Andrew MacFarlane.

# Table of Contents

<b>Abstract</b> . . . . .	iii
<b>Lay Summary</b> . . . . .	v
<b>Preface</b> . . . . .	vi
<b>Table of Contents</b> . . . . .	ix
<b>List of Tables</b> . . . . .	xiii
<b>List of Figures</b> . . . . .	xiv
<b>List of Schemes</b> . . . . .	xviii
<b>List of Abbreviations</b> . . . . .	xix
<b>List of Symbols</b> . . . . .	xxi
<b>Acknowledgements</b> . . . . .	xxiv
<b>Dedication</b> . . . . .	xxv
<b>1 Introduction</b> . . . . .	1
1.1 High Concentration Solutions and Room Temperature Ionic Liquids . . . . .	2

*Table of Contents*

---

1.1.1	Ion Interactions in Media . . . . .	4
1.1.2	Diffusion . . . . .	9
1.1.3	Electrophoresis . . . . .	13
1.1.4	Relation Between Electrophoresis and Self-Diffusion . . . . .	16
1.2	Research Aims and Outline . . . . .	19
<b>2</b>	<b>Magnetic Resonance Transport Measurements: Theory and Background</b>	<b>22</b>
2.1	Pulsed Field Gradient-NMR . . . . .	23
2.2	eNMR . . . . .	26
2.2.1	Signal Evolution . . . . .	27
2.2.2	eNMR Limitations and Probe Design Solutions . . . . .	29
2.2.3	Pulse Sequence Based Solutions . . . . .	35
<b>3</b>	<b>Magnetic Resonance Transport Measurements: Methods</b>	<b>39</b>
3.1	NMR Spectrometers . . . . .	39
3.2	Home built PFG Probe and Driving Circuit . . . . .	40
3.3	Data Interpretation . . . . .	41
3.3.1	Temperature Control . . . . .	42
3.4	Bruker Imaging 3-axes Gradient Set . . . . .	44
3.5	eNMR Probe Construction and Validation . . . . .	45
3.5.1	Introduction . . . . .	45
3.5.2	Methods . . . . .	45
3.6	Data Interpretation . . . . .	49
3.6.1	Conclusions . . . . .	50
<b>4</b>	<b>Diffusion of EMI-TFSI Dilutions in Propylene Carbonate</b>	<b>52</b>
4.1	Introduction . . . . .	52

*Table of Contents*

---

4.2	Methods . . . . .	56
4.3	Results and Discussion . . . . .	57
4.4	Conclusions . . . . .	68
<b>5</b>	<b>Ion Transport in Touch Sensor Electrolytes . . . . .</b>	<b>70</b>
5.1	Introduction . . . . .	70
5.2	Methods . . . . .	72
5.2.1	Sample Preparation . . . . .	72
5.2.2	Viscosity Measurements . . . . .	72
5.2.3	Self-Diffusion Measurements . . . . .	73
5.2.4	eNMR Measurements . . . . .	73
5.2.5	Conductivity and Piezoionic Measurements . . . . .	75
5.3	Results and Discussion . . . . .	76
5.3.1	Self-Diffusion in Electrolyte Samples . . . . .	77
5.3.2	Self-Diffusion in Polymer Electrolyte Samples . . . . .	84
5.3.3	Driven Diffusion in Solution Electrolyte Samples . . . . .	88
5.3.4	Driven Diffusion in Polymer Electrolyte Samples . . . . .	96
5.4	Conclusions . . . . .	98
<b>6</b>	<b>Chromophore Diffusion in Optical Filter Devices . . . . .</b>	<b>100</b>
6.1	Introduction . . . . .	100
6.2	Methods . . . . .	102
6.3	Results and Discussion . . . . .	106
6.4	Conclusions . . . . .	118
<b>7</b>	<b>Vitrimers - Transport of Thermally Exchangeable Molecules . . . . .</b>	<b>120</b>
7.1	Introduction . . . . .	120

*Table of Contents*

---

7.2	Methods . . . . .	122
7.3	Results and Discussion . . . . .	127
7.4	Conclusions . . . . .	138
<b>8</b>	<b>Conclusions and Future Work . . . . .</b>	<b>139</b>
8.1	Conclusions . . . . .	139
8.2	Recommended Future Work . . . . .	142
8.2.1	eNMR Probe Construction and Validation . . . . .	142
8.2.2	Diffusion of EMI-TFSI Dilutions in Propylene Carbonate . . . . .	142
8.2.3	Ion Transport in Touch Sensor Electrolytes . . . . .	143
8.2.4	Chromophore Diffusion in Optical Filter Devices . . . . .	144
8.2.5	Vitrimers - Transport of Thermally Exchangeable Molecules . . . . .	145
8.3	Outlook . . . . .	146
	<b>Bibliography . . . . .</b>	<b>147</b>
	 <b>Appendices</b>	
<b>A</b>	<b>Vitrimer Sample Preparation . . . . .</b>	<b>170</b>

# List of Tables

4.1	Ratio of D coefficients ( $\frac{D_+}{D_-}$ ) for EMI-TFSI in solution and IPN . . . . .	62
6.1	D comparison of selected chromophores in crosslinked samples . . . . .	112
6.2	Transition time and D comparison . . . . .	113
6.3	Chromophore D comparison with and without applied V . . . . .	118
7.1	D of vitrimer sample PD1a vs. temperature and time. . . . .	127
7.2	Initial Ds in PDMS backbone vitrimers . . . . .	131
7.3	D of heterogeneously loaded vitrimer vs. time . . . . .	133
7.4	Ds of vitrimer sample PD1c under different mechanical stress . . . . .	136

# List of Figures

1.1	Structure of common RTILs . . . . .	3
1.2	Types of ion pairs . . . . .	6
1.3	Supra-molecular ionic structures . . . . .	7
2.1	Pulsed Field Gradient(PFG)-echo pulse sequence diagram . . . . .	23
2.2	Pulsed Field Gradient Stimulated Echo (PFG-STE) pulse sequence diagram	25
2.3	Spin echo eNMR pulse sequence diagram . . . . .	28
2.4	Conventional arrangements for eNMR sample cells . . . . .	30
2.5	Conventional arrangements for eNMR sample cells with capillary tubes . .	33
2.6	Artifact flow suppression CPMG-eNMR pulse sequence diagram . . . . .	36
2.7	Double Stimulated Echo-eNMR pulse sequence diagram . . . . .	37
3.1	Signal intensity vs. magnetic field gradient for calibration measurements . .	42
3.2	Temperature control set-up illustration . . . . .	43
3.3	Diagram of constructed eNMR probe . . . . .	47
3.4	Charged particle distribution diagram . . . . .	48
3.5	eNMR pulse sequence diagram . . . . .	49
3.6	Measured phase shift under applied voltage . . . . .	51
3.7	Zero <sup>th</sup> order phase vs. constant current . . . . .	51
4.1	Experimental setup for sensor characterization . . . . .	54

*List of Figures*

---

4.2	EMI-TFSI sensor and actuator mode measurements . . . . .	54
4.3	EMI-TFSI ionic conductivity vs concentration . . . . .	55
4.4	Structural formula of RTIL EMI-TFSI and co-solvent PC . . . . .	56
4.5	$^{19}\text{F}$ spectra of 3 M EMI-TFSI/PC in PEO-NBR IPN . . . . .	57
4.6	Solution and IPN $^1\text{H}$ spectra comparison for 3 M EMI-TFSI in PC . . . . .	58
4.7	2.50 M EMI-TFSI/PC self-diffusion sample of TFSI $^-$ anion in PEO-NBR IPN	59
4.8	Self-diffusion summary for EMI-TFSI/PC solution and IPN . . . . .	60
4.9	Estimated conductivity derived from self-diffusion measurements. . . . .	65
4.10	Ratio of directly measured conductivity $\sigma_{\text{mes}}$ to estimated $\sigma_{\text{NMR}}$ . . . . .	66
4.11	Co-solvent PC self-diffusion vs. RTIL concentration . . . . .	67
5.1	Structures of Li $^+$ and bis(trifluoromethane)-sulfonimide (TFSI $^-$ ) ions . . . .	72
5.2	Structure of Propylene Carbonate (PC) . . . . .	73
5.3	Poly(vinylidene fluoride-co-hexafluoropropylene) (PVDF-HFP) co-polymer .	73
5.4	Voltage response to deformation of PVDF-HFP with varying LiTFSI conc.	76
5.5	2 M LiTFSI/PC self-diffusion sample of TFSI $^-$ anion in solution . . . . .	79
5.6	2 M LiTFSI/PC self-diffusion sample of Li $^+$ cation in solution . . . . .	79
5.7	D of LiTFSI vs. electrolyte concentration . . . . .	80
5.8	Dynamic viscosity and derived effective $r$ of LiTFSI solutions vs. concentration	81
5.9	Total conductivity derived from PFG-NMR self-diffusion measurements of LiTFSI vs. salt concentration in PC . . . . .	83
5.10	Transport number derived from self-diffusion measurements of LiTFSI vs. salt concentration in PC . . . . .	84
5.11	2 M LiTFSI/PC self-diffusion sample of TFSI $^-$ anion in polymer . . . . .	85
5.12	2 M LiTFSI/PC self-diffusion sample of Li $^+$ cation in polymer . . . . .	86

*List of Figures*

---

5.13	Self-diffusion measurements of LiTFSI vs. electrolyte concentration embedded in PVDF-HFP co-polymer . . . . .	87
5.14	Total conductivity and transport numbers derived from PFG-NMR self-diffusion measurements of LiTFSI vs. salt concentration in Gel samples . . . . .	88
5.15	NMR spectra of 2.0 M LiTFSI in PC as a function of applied electric field . . . . .	90
5.16	Electrophoretic mobility measurements for LiTFSI vs. salt concentration in PC as measured by eNMR . . . . .	91
5.17	Transport numbers vs. salt concentration in PC derived from eNMR . . . . .	95
5.18	$z_{\text{eff}}$ derived from eNMR measurements vs. salt concentration in PC . . . . .	96
5.19	Total conductivity derived from eNMR mobility measurements of LiTFSI vs. salt concentration in PC . . . . .	97
6.1	Chromophore inter-conversion general structure . . . . .	101
6.2	Chromophores structure . . . . .	103
6.3	Schematic and wiring diagram of gelled sample between electrodes . . . . .	105
6.4	General molecular structure of blue chromophore and 1D $^{19}\text{F}$ NMR spectra of S158 for both light and partially dark state . . . . .	106
6.5	$^{19}\text{F}$ NMR measurements of S164 chromophore in the open state dissolved in Rhodiasolv <sup>®</sup> IRIS/BC . . . . .	109
6.6	General structure of the open state chromophore in parallel and anti-parallel arm positions . . . . .	110
6.7	S164 $^{19}\text{F}$ NMR measurements vs. temperature . . . . .	111
6.8	Self-diffusion measurements vs. temperature for 4 chromophores . . . . .	113
6.9	Uncrosslinked full formulation sample S164 left at 250 K overnight . . . . .	114
6.10	Chromophore diffusion example for S109 . . . . .	115
6.11	Chromophore diffusion example with applied voltage of S109 . . . . .	116

*List of Figures*

---

7.1	PDMS-NH <sub>2</sub> polymer structure . . . . .	124
7.2	Exchangeable crosslinker 1,12-dodecane-bis- $\beta$ -ketoenamine <i>n</i> -butyl . . . . .	124
7.3	Non-exchangeable crosslinker triethylene glycol dimethacrylate. . . . .	124
7.4	Exchangeable tag 2,2,2-Trifluoroethylacetoacetate . . . . .	124
7.5	Nonexchangeable tag 2,2,2-trifluoroethyl methacrylate . . . . .	124
7.6	4-trifluoromethyl-4'-methylacetoacetate azobenzene tag . . . . .	125
7.7	Steps of heterogeneously loading a sample with coloured tag molecule . . . . .	126
7.8	Sample PD1a D as heated from room temperature to 100 °C . . . . .	128
7.9	Sample PD1b D at 60 °C before and after 10 hours . . . . .	130
7.10	Relaxation times of sample PD1 vs temperature . . . . .	132
7.11	Explanation of the mechanical stress in the sample at different steps . . . . .	136
7.12	Pictures of sample PG1 before and after physical stress application . . . . .	137
A.1	2,2,2-Trifluoroethylacetoacetate. . . . .	170
A.2	1,12-dodecane-bis- $\beta$ -ketoenamine <i>n</i> -butyl . . . . .	170
A.3	4-trifluoromethyl-4'-methylacetoacetate azobenzene . . . . .	171
A.4	PDMS-NH <sub>2</sub> polymer structure . . . . .	172

# List of Schemes

7.1	General mechanism of thermally exchangeable covalent bonds in vitrimers.	122
7.2	Vinylogous urethane exchange reaction of a pendant molecule . . . . .	123
A.1	Synthesis steps for F labelled tag . . . . .	172

# List of Abbreviations

**BC** butylene carbonate

**DLS** dynamic light scattering

**eNMR** electrophoretic NMR

**FID** free induction decay

**IPN** interpenetrating polymer network

**LN<sub>2</sub>** liquid nitrogen

**MRI** magnetic resonance imaging

**NBR** nitrile butadiene rubber

**NMR** nuclear magnetic resonance

**NOE** nuclear Overhauser effect

**PC** propylene carbonate

**PEO** poly(ethylene oxide)

**PFG-NMR** pulsed field gradient NMR

**RF** radio frequency

*List of Abbreviations*

---

**RMS** root mean square

**RPM** restrictive primitive model

**RTIL** room temperature ionic liquid

**SNR** signal to noise

**STE** stimulated echo

**TEAP** tetramethylammonium hexafluorophosphate

# List of Symbols

$\alpha$  Correction parameter to electrophoretic migration used for ionic conductivity calculation (Eq. 1.10 )

$b$  Parameter from Stoke-Einstein equation (Eq. 1.5). Reflects the boundary conditions for the velocity of the surrounding at the surface of the solute. Depends on the friction between the solvent and solute

$B_0$  Static magnetic field

$\chi$  Ionic strength

$C$  Concentration

$\Delta$  Diffusion time: the time delay between the magnetic field gradient pulses

$\delta$  Magnetic field gradient pulse duration

$D$  Self-diffusion coefficient

$E$  Electric field

$e$  Electron charge

$\epsilon$  Dielectric constant

$\epsilon_0$  Permittivity of vacuum

$\eta$  Kinematic viscosity

$\mathcal{F}$  Faraday constant

F Force

f Friction drag factor

g Magnetic field gradient strength

$\gamma$  Gyromagnetic frequency

I Current

J Particle flux

$\kappa^{-1}$  Debye length

$k_B$  Boltzmann constant

$\lambda_B$  Bjerrum length

$\mu$  Electrophoretic mobility coefficient

$N_A$  Avogadro's number

$\nu$  Drift velocity

$\omega$  Larmor frequency

q Electric charge

Q Heat

r Effective radius

*List of Symbols*

---

R Resistance

$\sigma$  Ionic conductivity

$T_1$  Spin-lattice relaxation time

$T_2$  Spin-spin relaxation time

$\tau$  Echo time

T Temperature

t Time

$t_i$  Transport number for a particular ionic species

U Electric potential

v Velocity

V Voltage

z Charge valence

$z_{\text{eff}}$  Effective charge

# Acknowledgements

First and foremost, I would like to thank my advisor Carl. Your knowledge knows no limits and it was a pleasure learning from someone who is a specialist in so many fields. You combine professionalism with kindness and patience in a way that very few can. I feel lucky to have had the chance to learn from you. You are truly an amazing mentor.

To all the past and present students of Room 100, thank you for always being there to lend a hand, be a shoulder to cry on, and to be quick to hand over a beer. The conversations we had were sometimes ridiculous and sometimes enriching, but they were always a pleasure.

To my Vancouver friends, thank you for welcoming me so quickly into your lives and for pronouncing hummus the proper way (at least when I'm around).

To my friends back home, thank you for supporting me through this adventure. I still wish for a direct flight between us, but sadly, that's not part of my research.

Dave, your love is the thing that got me here in one piece. I am so happy we found each other.

To my dearest family, I owe every single accomplishment to your love, support, and faith in me. You are the ones who made me believe that nothing is impossible.

And to Pippin, thanks for all the licks.

# Dedication

מוקדש להורים היקרים שלי, אילנה ויוסי פטל.  
הראתם לי שהכל אפשרי הודות לאהבתכם.

# Chapter 1

## Introduction

Many interesting and useful properties seen in new materials are based on the transport of molecules and ions. An understanding of this transport is essential to guide the development of innovative materials. To achieve better control over mechanical properties, reaction rates, and conductivities one must obtain better understanding of the molecular mechanisms which result in such properties. Many experimental and theoretical studies have been devoted over the last century to the diffusivity of dilute solutions [6, 7, 8, 9, 10] yet, much less to the investigation of concentrated solutions. Although it has been widely observed that classical theory does not directly apply to the diffusion of particles outside the realm of infinitely diluted solutions [11, 12], a lot remains unknown due to the relatively small number of experimental techniques by which diffusion may be measured [13, 14].

In this dissertation, nuclear magnetic resonance (NMR) is deployed as a tool to track the migration of magnetically visible molecules and ions, in a variety of media, to try and isolate the mechanisms of both self and driven diffusion. We will discuss the thermally and electrically driven diffusion of ions in varying concentration solutions and electrolyte swollen polymer gels, the diffusion of chromophore molecules in novel optical devices, and the stress induced diffusion of crosslinker molecules in a new class of recyclable polymers.

The experiments presented in the following chapters were performed in collaboration with several research and industry groups that produce unique polymer-based materials for a variety of applications. The samples contain solutions that are soaked or embedded

in semi-solids such as polymers, gels, and gel electrolytes. These semi-solids combine behaviours of solids and liquids, having relatively fast diffusion and a firm physical structure. This combination of properties enables the production of flexible, transparent conductive devices such as solar cells, batteries, screens and sensors. Still, due to strong interactions between the ions and their surrounding environment, many questions remain unanswered regarding the diffusion and conduction mechanisms in this type of medium. With the ever-increasing importance of technology based on these materials, a detailed understanding of the microscopic mechanisms of mass transport is essential.

In all of these projects, some interaction between the ions, solvent, polymer or a combination of the three create interesting phenomena that alter the diffusion and mobility of the dissolved species. By combining strong magnetic field gradients and short gradient pulses, pulsed field gradient NMR can provide measurements of diffusion coefficients for a high range of concentrated solutions and semi-solid samples. Using this technique to obtain specific diffusion coefficients for each species in a variety of polymer based materials will help to better explain some of the underlying phenomena. Applying an electric field to the samples allowed us to measure mobility constants and observe ionic conductivity *in-situ* and help shed light on the mechanisms and interactions driving them.

## 1.1 High Concentration Solutions and Room Temperature Ionic Liquids

Many applications of electroactive gels, including some of the materials to be investigated herein, are based on one of the most interesting types of ion-dense materials: ionic liquids. Room temperature ionic liquid (RTIL), such as EMI-PF<sub>6</sub>, EMIM-BF<sub>4</sub> (see structures in Fig. 1.1, EMI-TFSI (Fig. 4.4), and many others, are salts that have melting points lower

than room temperature. Most of the interest in RTILs has been due to their negligible vapour pressure and low flammability. This, among other unique properties, makes them good candidates as non-aqueous polar solvents that are also non-coordinating [15]. These properties have made RTILs candidates to replace organic solvent based electrolytes in electrochemical technologies such as super capacitors, batteries, organic dye sensitized solar cells, and actuators. However, although RTILs are comprised of ions entirely, the room temperature conductivity of pure RTILs is currently too low for them to become profitable replacements for existing organic electrolyte solutions. By introducing a co-solvent, the ionic conductivity of RTILs can be tuned and improved. Common existing electrolytes are made from salts dissolved in organic solvents. These mixtures usually suffer from limited salt solubility, which also limits the working temperature range [16, 17]. The fact that RTILs are completely miscible with organic solvents presents an advantage that also allows for a wider range of stable working temperatures.

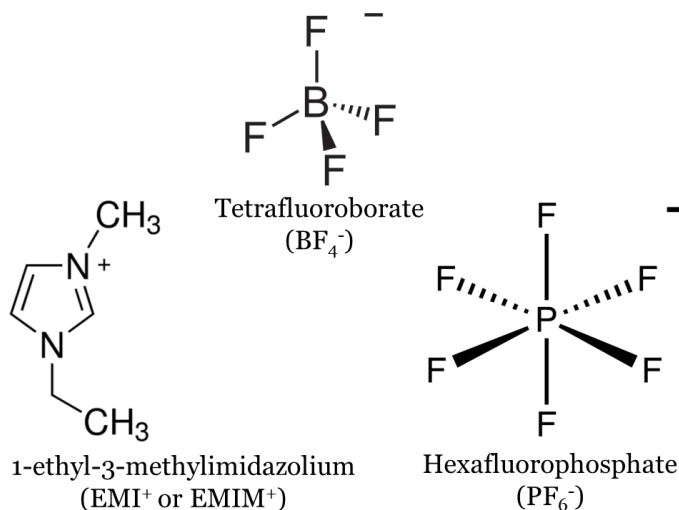


Figure 1.1: The structure of commonly used room temperature ionic liquids (RTILs).

One of the advantages of RTILs as a group is the large variety of physio-chemical properties they have. By choosing the correct combination of ions, it is possible to change

chemical and physical properties, optimizing them specifically for a desired use [18]. Yet, predicting the physio-chemical properties from the chemical structure is complicated. One of the current challenges results from the complexity of interactions between the ions of RTILs. These unique interactions distinguish the physical behaviour of RTILs from traditional solvents and consequently, makes their design difficult.

In general, solvents are classified according to their polarity and dielectric constant. These scales are helpful in predicting the solvent's properties such as its ability to dissolve ionic solute. RTILs have shown contradictory results, depending on the method used to measure polarity and their solvent behaviour does not follow the polarity scale [19]. It is agreed upon that a quantitative description of the ion association can be used as a useful indicator to characterize RTILs. A good correlation was shown between "ionicity" (level of ionic association) and physio-chemical properties such as polarity, surface tension, density, and conductivity [20]. RTILs' relatively low conductivity and its dependence on dilution leads to the assumption that they form ion pairs or higher-order supramolecular structures [21, 22].

In order to enable optimization of ionic conductivity, an accurate technique is needed for measuring microscopic diffusive transport. This method must be usable with different combinations of co-solvents and RTILs, under a variety of physical and chemical conditions.

### 1.1.1 Ion Interactions in Media

In order to better understand ion transport in electrolyte solutions, a variety of interactions must be considered. Interactions between ions, solvents and other components in solution will affect the motion of ions and will play a major part in determining the transport. This section will present some of the existing theories of interactions of ions in solution and porous media.

### Ion-Solution Interactions

When describing an electrolyte solution, one must think of the local electric field distribution around each ion and how it affects the surrounding molecules. As known from basic electrostatics, any charged particle creates an electric potential that decays with distance. The extent of this electric potential depends on both the charge distribution of the particle itself as well as the surrounding dielectric constant. The Debye length, or electrostatic screening length, is a measure of the electrostatic effect a charged particle has in solution (see Eq. 1.1). This measure of distance arises from the Poisson-Boltzmann equation solved for a spherical charge in a continuous medium under the restrictive primitive model (RPM) [23]. In this classical model, equal numbers of positive and negative ions in solution are modelled as hard spheres [24]. The Debye length describes the scale for the exponential drop of potential with distance from the ion due to the dielectric screening effect of the media [25]. For electrolyte solutions, the Debye length is usually noted as  $\kappa^{-1}$  and for a monovalent symmetrical electrolyte is given as

$$\kappa^{-1} = \sqrt{\frac{\epsilon_0 \epsilon k_B T}{2 N_A e^2 \chi}} \quad (1.1)$$

where  $\epsilon_0$  is the permittivity of vacuum,  $\epsilon$  the solution dielectric constant,  $k_B$  the Boltzmann constant,  $T$  the absolute temperature,  $e$  the electron charge,  $\chi$  the ionic strength, and  $N_A$  is Avogadro's number.

Keeping the RPM in mind, the potential from a central ion attracts counterions in a sphere with radius equal to  $\kappa^{-1}$ . This sphere surrounds the ion with a “cloud” of molecules with a total effective charge opposite to that of the central ion. This “cloud” is composed of both solvent and counterions that screen the electric potential from the central ion. The counterions in this cloud are in constant movement and only have an average, effective

charge; they are not fixed to the molecule [26]. In a highly diluted solution, this cloud consists entirely of solvent molecules and is termed a solvation layer. Together with the ionic radius, the Debye length determines the size of the solvation layer around an ion, which in turn will determine the ion effective size, weight, and its tendency to aggregate with other ions in solution.

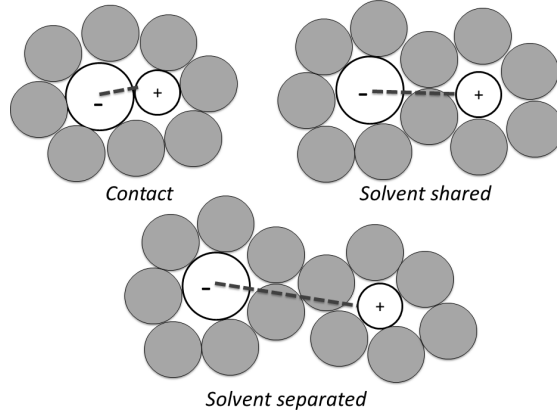


Figure 1.2: Types of ion pairs. Dark circles represent solvent molecules and light circles represents ions. The Debye lengths of the ions must be at least as long as the distance between the ions in order for the ion-pairs to exist. Therefore, the Debye length for an ion in a contact ion pair can be short, while it must be much longer for ions in a solvent separated pair. An illustration of the Debye length for the anion is marked as a grey dashed line.

In addition to the interactions with the solvation layer, ions also experience long-range electrostatic forces. The counterions attract each other according to Coulomb's law, making it possible for ion-pairs to form. This attraction is masked by the permittivity of the solution. One of the theories to define ion pairs was suggested by Bjerrum [27]. The Bjerrum length,  $\lambda_B$ , given by

$$\lambda_B = \frac{z_- z_+ e^2}{4\pi\epsilon_0\epsilon k_B T} \quad (1.2)$$

determines the cut-off distance at which associated ions with charges  $z_+$  and  $z_-$  are consid-

ered paired.  $\lambda_B$  is the distance at which the electrostatic interaction energy is comparable to the thermal energy. If the distance between the ions is smaller than  $\lambda_B$  the ions are considered paired and will form a long-lasting aggregate.

This means the ions are arranged in a non-rigid structure, such as those in Fig. 1.3, in which the ions' motion is correlated for a time longer than would be taken for non-associated species to diffuse over the distance between them [28, 29]. In this range of distance, the solvation layers might be present to varying extent and several types of ion pairs, as described in Fig. 1.2, can be distinguished. In case of a highly concentrated solution, such as an RTIL, ion pairs might form bigger, supramolecular structures consisting of more than two ions as can be seen in Fig. 1.3. When ions are bound in these structures, their effective radius,  $r$ , changes to some combination of the ions and solvent. The net charge of this entity is the sum of its ionic components and, as for an ion-pair, might be neutral. For water at room temperature with 1 M ionic strength  $\lambda_B \approx 2\kappa^{-1}$ .

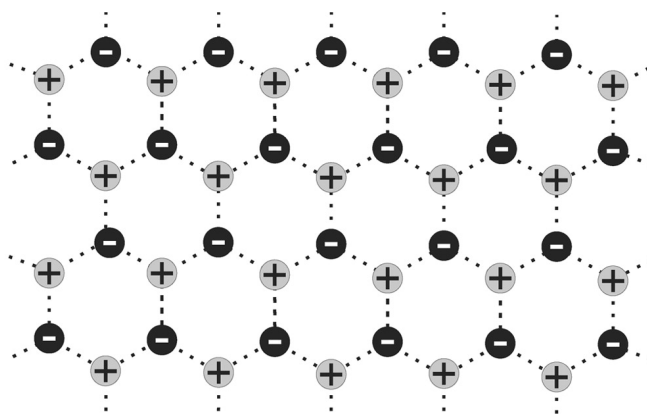


Figure 1.3: Supra-molecular ionic structures. Dark circles represent anions and light circles represents cations which are held together by electrostatic forces represented by dotted lines. Figure adapted from Dupont *et al.* [22] with permission.

## Ion-Polymer Interactions

Since the discovery of the first ion conducting polymer four decades ago [30], and the demonstration of an all-solid-state battery cell [31], significant effort has been spent developing efficient polymer electrolytes. Polymer electrolytes are a safer, more durable replacement for liquid electrolytes in electrochemical devices. Polymer electrolytes can be described as membranes with transport properties comparable to liquid ionic solutions, which are used in the vast majority of current Li-ion batteries. The interactions between the ions and the polymer alter the ion motion, affecting conductivity and device performance.

Polymer gel electrolytes are cross-linked polymers swollen with solvent and therefore possess both the physical firmness of a solid and the diffusive properties of liquid. The major interactions between polymers and small molecules in these materials arise from polymer solvation. Depending on the polymer and the solvent, these interactions vary from weaker van der Waals bonds to stronger electrostatic-based bonds or even coordination bonds in some cases [32]. In some cases, polymers are directly charged and therefore produce a surrounding electric field. For example, polyelectrolytes are polymers that lose a charged group when dissolved, leaving the backbone of the polymer charged [33]. Another example is conjugated polymers. This family of organic polymers are considered conductors when doped and semiconductors when undoped. The process of doping usually involves an oxidation reaction that increases the mobility of electrons in the conjugated  $\pi$ -orbital. When maximally-doped, they may hold up to one charge per three monomer units. Applying an electric potential may lead to a total positive charge on the polymer backbone that corresponds to a capacitance of up to 100 F/g [34]. In order to balance this charge, negative ions from the solution will bond with the polymer and, if the conditions allow it, an influx of negative ions will penetrate the polymer, causing it to swell. The interaction between polymer chains and the ions is electrostatic and is similar to the ion-

solution forces that were previously described. However, even neutral polymers have some charge distribution that causes molecular binding of ions from the solution.

Depending on the solvent, the ion charge and size, and the polymer charge distribution, polymer-ion interactions will have different effects on the distribution of ions in solution. Some interactions might be strong enough to leave the ions immobile while others may not be strong enough to create a long-lasting association.

### 1.1.2 Diffusion

Now that the interactions ions experience in solution have been considered, it is possible to discuss ion motion in different media. Diffusion is generally divided into two major types—driven by a potential gradient or by thermal energy. In the following sections we will discuss thermally driven self-diffusion and diffusion that is driven by an electric potential gradient: electrophoresis.

#### Self-Diffusion

Translational diffusion, or self-diffusion as it will be referred to in this dissertation, is diffusion under zero chemical potential gradient, that is, under conditions of uniform concentration [35]. It arises from random, thermal motions and collisions, and is characterized through the self-diffusion coefficient,  $D$ . Self-diffusion, or Brownian motion, results in the increasing displacement of particles as a function of time. While the mean displacement is zero in an isotropic medium, the mean squared displacement after time  $t$  is given by [36]:

$$\langle d^2 \rangle = 2DNt. \tag{1.3}$$

where  $N$  is the dimensionality of the motion. Microscopically,  $D$  is given by the Einstein-Smoluchowski-Sutherland equation [36, 37, 6],

$$D = \frac{k_B T}{f}. \quad (1.4)$$

where  $f$ , the friction drag factor, describes the drag force on a particle moving with a velocity  $v$  in a viscous fluid,  $f = -F_{\text{drag}}/v$ .  $f$  depends on all the interactions mentioned in Section 1.1.1, and is unique to any solution and physical condition.

In its more common form, Eq. 1.4 is known as the Stokes-Einstein equation for a spherical molecule [25]:

$$D = \frac{k_B T}{b\pi\eta r} \quad (1.5)$$

where  $\eta$  is the kinematic viscosity of the medium,  $r$  is the effective radius of the diffusing particle, and  $b$  is a dimensionless number that reflects the interactions between the molecule of interest and its surroundings.  $b$  ranges from 4 (no interaction) to 6 (strong interaction) [37]. When considering the strong interaction limit, this equation is known as Stokes' Law.

Even though Eq. 1.5 is widely used to describe self-diffusion, experimental data has shown  $b$  to be outside the predicted range of 4-6. This is a result of several approximations that are not necessarily obeyed in certain solutions. Eq. 1.5 assumes the actual shape of the ion is spherical, the solvation layer rigid, and a solute/solvent size ratio of at least 4 [8]. In addition, it assumes all interactions between the solute molecules are negligible. For most diluted salt solutions, these approximations are accurate enough. Yet, as discussed, there are a number of interactions in an ionic solution that affect both the ion and the medium in question. For those solutions which diverge from these assumptions, the Stokes-Einstein equation does not hold and diffusion coefficients cannot be predicted accurately.

### **Effect of Media on Diffusion**

As expected, polymer chains retard any diffusive motion. How this happens has been investigated but is still an area of active research. Many of the proposed mechanisms have either an unexplained empirical factor or are only applicable to a narrow range of solvents and polymers. The models that have been proposed for calculating the diffusion factor of solutes in a polymer network can be combined into three general families of models. These are known as the ‘Average Free Volume’, ‘Hydrodynamic’ and ‘Obstruction’ model families [38].

Diffusive motion primarily occurs within and between the solvent-filled regions bounded by the polymer chains. The free volume models are unique in that they do not consider diffusion as a molecular, thermally-activated process. Instead, they assume diffusion is a result of random redistribution of free volume spaces within the polymer mesh, a property of the polymer dynamics. Molecules can move from one free space to another if their effective cross-section is smaller than the opening between spaces. The existence of voids arises from a statistical redistribution of the free volume. The more general description defines the free volume as the volume of a system at a given temperature minus the volume of the same system at 0 K, where there is no polymer motion [39]. The empirical ratio that determines the free volume effect on the diffusion coefficient is dependent on many factors, depending on the specific theory, but is mostly the size of the diffusive molecule in relation to the size of the passage between pores— a factor that is dependent on the density of cross links between the polymer chains.

In the ‘Obstruction’ family of models, the diffusion of the polymer molecules is assumed to be negligible. The path of solute molecules is highly tortuous, due to the mesh of polymer chains obstructing their path. Consequently, the relevant parameters for these models are the volume fraction of the solute and polymer and the solvent’s volume and shape [40, 41].

In addition, an empirical factor is added to some of those models to include solvent polymer interactions that may bind the solvent molecules to the polymer[38]. The tortuous nature of the path means that the diffusion length may no longer scale with the square root of time so that the diffusion measured depends on the duration of the measurement.

The hydrodynamic models consider the hydrodynamic drag force experienced by the solute and are based on the Stokes-Einstein equation, taking into account the interactions present in the whole system to determine the friction drag factor. According to these models, the polymer chains increase the drag on the molecules by slowing the solvent flow in the proximity of the polymer. Some of the models do take into account the binding of ions to the charged groups on the polymer chains [42]. By summing all the friction factors between any molecule and the total polymer, a ratio between the free solution diffusion to the diffusion in a polymer network is determined.

To summarize, the effect a polymer network has on solute diffusion is complicated and hard to predict, especially when taking into account the numerous factors that affect both the solute molecule and the polymer mesh. The models that exist today are helpful, but not sufficient to present the full picture.

## **Diffusion Measurements**

Because self-diffusion is a process that takes place even at equilibrium, it does not necessarily result in an observable change in the system. In order to follow the self-diffusion motion, some kind of labelling is required to allow tracking of a molecule. In NMR, the spatial labelling of molecules is achieved by using a magnetic field gradient in a non-invasive manner. By combining NMR's ability to distinguish chemical environments with spatial resolution, the tracing of different components in solution is possible. As NMR can observe magnetically-visible nuclei in any phase, it has become a popular technique to measure dif-

fusion for gases, liquids and solids. This well-established method is known as pulsed field gradient NMR (PFG-NMR) and it will be discussed in Section 2.1.

Another method that can measure self-diffusion is dynamic light scattering (DLS). This technique can measure the velocity at which particles move by measuring the time dependent fluctuations in the intensity of scattered light. This method is widely used and can measure self-diffusion of particles and micelles easily [13]. For the case of RTIL and other solvated molecules, DLS cannot separate between similar sized species and therefore measures an average diffusion constant termed “Mutual Diffusivity” [43, 44].

### 1.1.3 Electrophoresis

In contrast to self-diffusion, electrophoresis describes particle motion that is driven in a directional, non-random manner. Electrophoresis describes the migration of charged particles in a spatially uniform electric field [36] and can be described as a “directed diffusion process” [45]. This mobility of charged ions is of high interest as it depends on both the charged species properties and the chemical environment, and so can give information on both.

A particle of charge  $q$  experiences force,  $F$ , due to an electric field,  $E$ , according to the following relation:

$$F = qE. \tag{1.6}$$

The particle is accelerated to velocity  $v$  by this force and will experience a drag force from the medium, denoted by the friction drag factor  $f$  which was introduced in Eq. 1.4. These combined forces result in a constant drift velocity  $\nu$ ,

$$\nu = \frac{F}{F_{\text{drag}}} = \frac{qE}{f} = \frac{zeE}{f}, \tag{1.7}$$

where  $z$  is the charge number of the particle in solution. To characterize this motion a coefficient is defined:  $\mu$ , the electrophoretic mobility. This transport quantity describes the motion in question with units of  $\frac{\text{m}^2}{\text{s}\cdot\text{V}}$  and is defined as the drift velocity,  $\nu$  of an ion in solution in response to an electric field of unit strength:

$$\mu = \frac{\nu}{E} = \frac{ze}{f}. \quad (1.8)$$

The electrophoresis friction drag factor  $f$  is affected by the same interactions as the self-diffusion, only, in addition, we need to consider the external electric field and the effect it has on the charge “cloud” that is surrounding the ion (see Section 1.1.1). The external potential has a tendency to alter the charge distribution around the ion and to move the ionic cloud itself in addition to the ion. Being oppositely charged, the cloud will tend to move in the opposite direction from the ion, and, because of the attractive forces between them, the migration of the ion will be attenuated by this effect, called the Asymmetry Effect [25].

### Ionic Conductivity

Ionic conductivity describes the ability of a solution to carry electric current. It arises from the motion of charge carriers in solution, and therefore depends on  $\mu$ , the electrophoretic mobility. The total ionic conductivity,  $\sigma$ , is the sum of each charge carriers’ specific conductivity in solution:

$$\sigma = \sum_i \mathcal{F}C_i|z_i|\mu_i, \quad (1.9)$$

where  $\mathcal{F}$  is the Faraday constant,  $C$  the concentration, and  $\mu$  is the specific mobility for each species and is denoted by the subscript  $i$ .

Yet, it is known that some interactions in the solution affect the charge each ion carries.

Some even create charge neutral aggregates that have no contribution to the total conductivity. Weaker ion associations that are not strong enough to create persistent aggregates can lead to correlated ion motion that similarly reduces the effective charge an ion carries. Eq. 1.9 needs to be adjusted to include a correcting factor that takes into account the ratio of the ions that are charged and contribute to the conductivity,

$$\sigma = \sum_i \alpha_i C_i \mathcal{F} |z_i| \mu_i. \quad (1.10)$$

Here the correction parameter  $\alpha$  is unique to electrophoretic migration measurements. It arises from the fact that only charged particles will migrate in response to an electric potential.  $\alpha$  can be combined with  $z$  to give the effective charge,  $z_{\text{eff}}$ . This correction factor can shed some light on ionic solution behaviour as it depends on the ratio of free ions to associated ones. Another common description of this correction parameter, most often found in the solid-state ionic conductor literature, is called the Haven ratio, which is the ratio between the conductivity derived from self-diffusion coefficients and the actual ionic conductivity [46, 47, 48, 49].

Due to the difference in charge contribution and the potentially different mobility of each ion in solution, the current is not necessarily carried equally by the different ionic species. The transport number,  $t_i$  is defined as the fraction of the current that is carried by a particular species [50]. It describes the contribution each species has to the total current:

$$t_i = \frac{\alpha_i C_i \mathcal{F} |z_i| \mu_i}{\sum_i \alpha_i C_i \mathcal{F} |z_i| \mu_i}. \quad (1.11)$$

The sum of transport numbers from all the charge carriers in solution is unity  $\left( \sum_i t_i = 1 \right)$ . Transport numbers are important design parameters for an electrolyte solution and can

help determine its potential applications. For example, a strong single-ion conductive polymer requires that one of the ions remain immobilized while the current is carried by the counterions alone—in other words, a transport number of unity for one of the ions [51]. In contrast, for an efficient capacitor, similar transport numbers for each of the ions would be an advantage [52, 53].

### **Electrophoresis Measurements**

The majority of today’s existing methods to measure mobility and transport number are only useful for liquid solutions and/or are not selective in their detection. They are not useful for multi-component solutions or polymer based electrolytes. The most famous methods to measure transport numbers are the moving boundary and Hittorf methods. Both of these fail when it comes to porous media (extensively discussed in [54, 55]). An additional problem is the inability to distinguish between ions in a polyelectrolyte solution. DC and AC methods rely on the relation between conductivity and mobility. They are useful for porous media, but do not distinguish between the different ionic species. A method which is both selective and allows for measurement in polymer networks is the radio tracer method, but it adds the complication of nuclear labelling [14]. DLS can be used to measure the velocity at which particles move by measuring the time dependent fluctuations in the intensity of scattered light. By applying a voltage to the sample, DLS can measure the electrophoretic mobility of particles and solvated molecules, but cannot separate between similar sized species [13, 43, 44].

#### **1.1.4 Relation Between Electrophoresis and Self-Diffusion**

It is straightforward to relate migration due to electrophoresis and diffusion. According to the Boltzmann distribution, in equilibrium the number of particles with charge  $q$  at

temperature  $T$  under an electric potential  $U$  is

$$N = N_0 \exp\left(\frac{qU}{k_B T}\right). \quad (1.12)$$

The particle spatial gradient is

$$\nabla N = \frac{qU}{k_B T} \nabla U \cdot N_0 \exp\left(\frac{qU}{k_B T}\right) = \frac{qU}{k_B T} \nabla U \cdot N, \quad (1.13)$$

and according to Fick's first law, the flux of particles  $J$  due to thermal energy is  $-D\nabla N$ .

The flux of particles under an electric field is the number of particles times their velocity.

The total flux in the system is equal to

$$J_{\text{total}} = J_{\text{drift}} + J_{(D)} = \mu \nabla U \cdot N - D \nabla N. \quad (1.14)$$

This is zero at equilibrium. By plugging in Eq. 1.13 we derive the Nernst-Einstein relation for charged particles:

$$D = \frac{k_B T}{z_{\text{eff}} e} \cdot \mu. \quad (1.15)$$

This relation between self-diffusion and electric mobility is completely general and is valid for any isothermic system and chemical condition.

Currently, accurate  $D$  values obtained by PFG-NMR are used to estimate mobility using the Nernst-Einstein relation. Plugging the relation in Eq. 1.9, results in an estimation for ionic conductivity and transport numbers:

$$\sigma = \sum_i \frac{z_i^2 C_i e \mathcal{F} D_i}{k_B T}. \quad (1.16)$$

These equations are often used under the assumption that  $z_{\text{eff}}$  is equal to the ion valence.

This assumption includes an inherent error that increases with the ionic strength of the solution. It is therefore expected that this assumption does not hold for the case of RTILs.

And, as expected, ionic conductivity measurements of RTILs deviate by up to  $\approx 70\%$  from conductivities derived from measured self-diffusion coefficients and the Nernst-Einstein relation, indicating the existence of ion-ion associated species [56, 57, 58]. By rearranging Eq. 1.15, it is possible to gain new knowledge of the level of ion association in solution. Using a combination of self-diffusion and mobility measurements enable determination of  $z_{\text{eff}}$ , the effective charge of the ion in question

$$\frac{\mu}{D} = \frac{z_{\text{eff}}}{k_{\text{B}}T}. \quad (1.17)$$

This parameter gives us a direct indication of the level of association of a specific ion species in solution.

Tokuda *et al.* [59] have measured a similar ratio and shown it to be a useful characterization parameter for the physical properties for RTILs. It was also shown to explain some of the unusual behaviour of ion transport in RTILs in solution with aprotic co-solvents [21]. In both of these papers,  $z_{\text{eff}}$  was obtained by measuring the ratio between conductivity, measured by electrochemical impedance, and conductivity derived from  $D$ , using Eq. 1.16.  $D$  was obtained accurately, using PFG-NMR, but the impedance measurements are highly non-selective and can only be used for a single ion with a non ionic solvent. Therefore their method is limited by the conductance measurement to an electrolyte with only one pair of charge carriers.

## 1.2 Research Aims and Outline

The work done in this dissertation aims to directly measure both self and driven diffusion in order to study the transport mechanisms of molecules in several unique materials. The materials investigated all show transport divergence from known theory which affects their physical properties. By selectively tracking both self and driven diffusion of molecules in a variety of materials we learn how transport contributes to their interesting mechanical, optical, and electrical behaviour. As discussed in this introduction, we expect the transport of molecules in concentrations above the highly diluted regime will diverge from the Stokes-Einstein equation (Eq. 1.5). This divergence is predicted to be the source of the unusual behaviour found in these materials. We expect the interaction between molecules in concentrated materials to decrease their ability to diffuse as well as their ability to conduct current. By directly measuring these properties, we aim to increase our understanding of transport mechanisms in concentrated materials and guide the further development of materials with interesting and useful properties.

Chapter 2 provides an overview of existing magnetic resonance techniques that were either used in this dissertation or inspired new technique development. The purpose of this chapter is to provide the reader with an understanding of the methods used, necessary for the discussion of results presented.

In Chapter 3, we describe the development of a simple eNMR probe within a horizontal magnetic field gradient set to allow for direct and selective measurements of electrophoretic mobility of magnetically visible species. This probe aims to measure mobility in a direction perpendicular to the majority of undesired flows such as convection currents or bubbles, resulting in accurate electrophoretic mobility measurements.

Chapter 4 aims to investigate the “piezoionic effect” observed in ionic electroactive polymer based soft strain sensors. As the mechanism behind the piezoionic effect is ambigu-

ous, a more in-depth investigation of molecular transport is necessary. By utilizing the well-established technique of PFG-NMR, we aim to explore how self-diffusion is affected by the concentration of RTIL in both solution and polymer samples.

The eNMR probe described in Chapter 3 is used in Chapter 5, along with PFG-NMR, to measure both self-diffusion and electrophoretic mobility of anions and cations in an electrolyte used for potential artificial muscles and nerves. Combining these measurements, we calculate the effective charge ( $z_{\text{eff}}$ ) for each of the ions in order to shed light on the unique conduction mechanism seen in lithium based salts. We observe how  $\text{Li}^+$  conductivity depends dramatically on concentration, contributing only a small fraction at low concentration, but completely dominating at high concentration. To explain this dramatic change in conductivity, we suggest a potential mechanism that explains this unique behaviour.

Chapter 6 describes transport measurements of electro-photochromic molecules embedded in polymer films which are used as optical filters which modulate solar energy absorption in vehicle sunroofs. Using PFG-NMR, we measure self-diffusion of these chromophores in a variety of conditions. These measurements were done in an effort to understand the performance limitations of these films and guide the development of the automotive glazing industry.

In Chapter 7, we again utilize PFG-NMR to investigate the stress relaxation mechanism observed in a new class of recyclable polymers. These thermoset polymers, called vitrimers, present an opportunity for efficient recycling via a thermally activated exchange of molecular cross-links. The transport of crosslinker molecules in vitrimers is investigated in this chapter, with emphasis on the driving force behind it. Through this investigation, we hope to learn of usage limitations for vitrimers and learn of the necessary conditions required for easy recycling.

Chapter 8 summarizes the lessons learned from these studies and how significant di-

## *1.2. Research Aims and Outline*

---

rect measurements of transport properties are for a full understanding of both conduction mechanisms and unique physical properties seen in concentrated materials. The chapter contains suggestions for additional experiments that would help to further our understanding of transport in these concentrated systems and closes with an outlook to the future.

## Chapter 2

# Magnetic Resonance Transport Measurements: Theory and Background

The purpose of this chapter is to provide an overview of the existing magnetic resonance methods for measuring self-diffusion and electrophoretic mobility. The reader should have basic knowledge of magnetic resonance theory in order to understand the majority of the coming chapter. If this knowledge is missing, we advise to review the first two chapters of Spin Dynamics by Malcolm H. Levitt [60]. For the case of electrophoretic mobility, this chapter describes several approaches and methods, each with its own advantages and disadvantages. As electrophoretic NMR (eNMR) is still an emerging technique, there is no industry standard agreed upon and research labs are still experimenting with different approaches to voltage application methods, sample holder set-ups, and pulse sequences.

This chapter begins with an overview of pulsed field gradient methods that will be used in Chapters 4, 5, 6, and 7. An understanding of this technique is crucial to the interpretation of the results presented in the mentioned chapters. This overview is followed by a review of the state-of-the-art of eNMR techniques. Not all methods described in this chapter were used in the work of this dissertation, but they inspired ideas for experimental set-ups and pulse sequences used in Chapters 3 and 5.

## 2.1 Pulsed Field Gradient-NMR

The well-established method of pulsed field gradient NMR (PFG-NMR) relies on similar principles to those underlying magnetic resonance imaging (MRI). An additional dimension that provides spatial information is encoded by introducing a magnetic field gradient, thereby making the Larmor frequency  $\omega$  location-dependent:

$$\omega_z = \gamma B(z) = \gamma(B_0 + gz) = \omega_0 + \gamma gz, \quad (2.1)$$

where  $\gamma$  is the gyromagnetic ratio of the isotope,  $g$  is the magnetic field gradient strength (in  $\frac{\text{G}}{\text{cm}}$ ) and  $B_0$  is the static magnetic field.

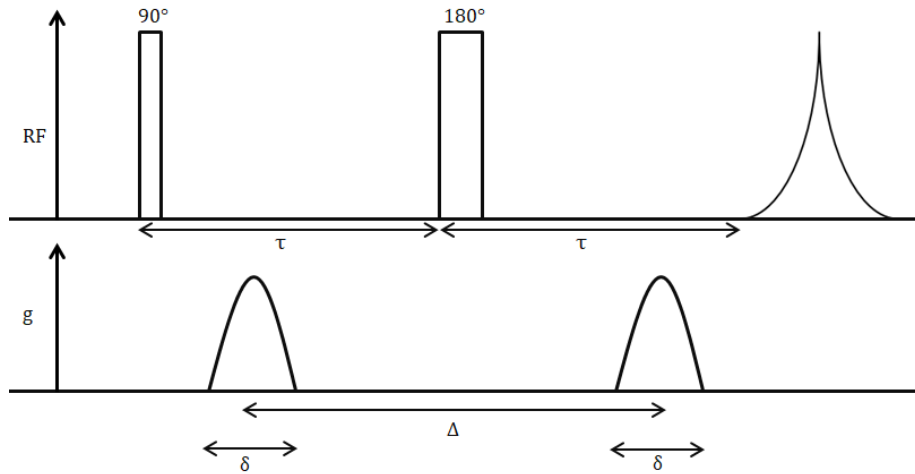


Figure 2.1: Pulsed Field Gradient(PFG)-echo pulse sequence diagram. The row labelled as RF represents the radio frequency channel and the row labelled  $g$  represents the magnetic field gradient channel, both against time.  $\delta$  is the sinusoidal gradient pulse duration and  $\Delta$  is the time delay between the magnetic field gradient pulses and is termed “diffusion time”.

By applying a magnetic field gradient in the  $z$  direction, each nuclear spin is labelled according to its position along the  $z$ -axis. Over time as diffusion takes place and the spins

move, they will develop a phase that is related to their displacement. This phase change will enable the determination of the self-diffusion coefficient. A simplified pulse sequence for diffusion measurements with PFG-NMR is illustrated in Fig. 2.1 based on the Stejskal and Tanner pulse sequence [61]. We will now elaborate on the phase progression of the spins during this pulse sequence. The initial  $\frac{\pi}{2}$  pulse tips the entire magnetization of the nuclei to the transverse plane, where it will begin precessing according to the Larmor frequency. By applying a short gradient pulse of duration  $\delta$ , each spin will acquire a phase according to its position  $\phi = \omega_z \delta$ . This initial position is now encoded to the spin's phase [62]. The total magnetization is weighted by spin-spin relaxation,  $T_2$ , and at the end of the first  $\tau$  is  $S_{(\tau-)} = \sum S_{(0)} e^{-i\omega_z \delta} e^{-i\omega_0 \tau} e^{\left(\frac{-\tau}{T_2}\right)}$  where the  $z$  dependence represented in the phase is seen explicitly. By applying a  $\pi$  pulse, the phase will be reversed and the magnetization will be  $S_{(\tau+)} = \sum S_{(0)} e^{+i\omega_z \delta} e^{+i\omega_0 \tau} e^{\left(\frac{-\tau}{T_2}\right)}$ . By reintroducing the gradient pulse of the same duration and strength, any spin that has not changed position will acquire the exact same phase as it did in the first section resulting in  $S_{(2\tau)} = \sum S_{(0)} e^{-i\omega_z \delta} e^{+i\omega_z \delta} e^{\left(\frac{-2\tau}{T_2}\right)} = \sum S_{(0)} e^{\left(\frac{-2\tau}{T_2}\right)}$ . This means the signal arising from spins that did not change their position is completely refocused. In contrast, any spin that changed location will have a total phase that depends on the magnitude of that position change.  $\phi = +\omega_{z_1} \delta - \omega_{z_2} \delta = \omega \delta \gamma g (z_1 - z_2)$ . Integrating over all trajectories will result in a signal that is attenuated by a diffusion factor. For a sinusoidal gradient pulse, this factor depends on  $\delta$ ,  $g$ ,  $\Delta$  and the self-diffusion coefficient  $D$  according to

$$S_{(2\tau)} = S_0 \exp\left(-\frac{4}{\pi^2} \gamma^2 g^2 \delta^2 \left(\Delta - \frac{\delta}{4}\right) D\right) \exp\left(-\frac{2\tau}{T_2}\right). \quad (2.2)$$

In order to allow the measurement of samples with short  $T_2$ s, as is the case of most viscous or solid samples [63], a stimulated echo (STE) RF pulse sequence may be used (see Fig. 2.2). This pulse sequence stores the magnetization along the  $z$ -axis (where no

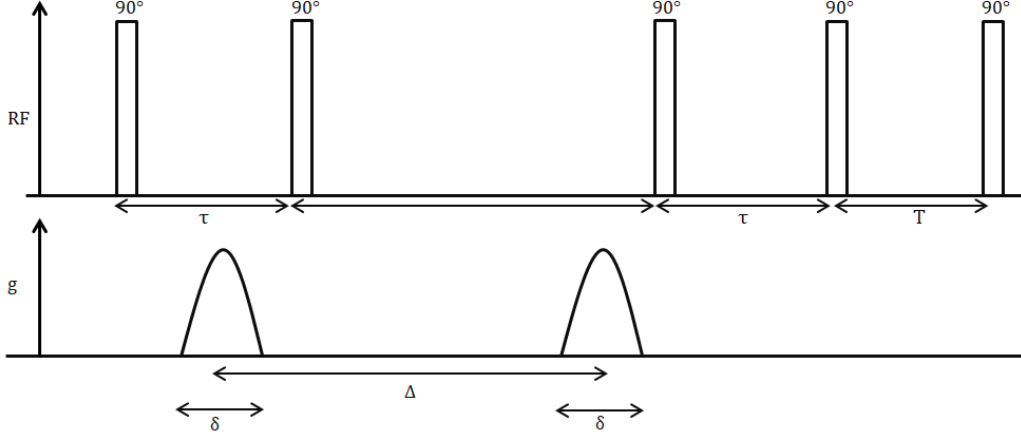


Figure 2.2: Pulsed Field Gradient Stimulated Echo (PFG-STE) pulse sequence diagram. An additional acquisition delay of duration  $T$  was inserted to allow eddy currents to decay.

spin-spin relaxation occurs) in between gradient pulses. As long as  $\Delta$  is larger than  $T_2$ , no magnetization will survive on the transverse plane, eliminating the dephasing effect of  $T_2$  relaxation during the diffusion time. As a result,  $T_2$  relaxation will only be affecting the spins during  $\tau$ . This allows for longer diffusion times  $\Delta$  to be used. Storing the magnetization along the  $z$ -axis does create a factor of two loss in signal and the magnetization undergoes spin-lattice relaxation with time constant  $T_1$  during the diffusion time. The duration of  $\tau$  is limited by the gradient pulse duration  $\delta$ . The total signal at the end of PFG-STE NMR pulse sequence is given by

$$S_{(2\tau)} = S_0 \exp\left(-\frac{4}{\pi^2} \gamma^2 g^2 \delta^2 \left(\Delta - \frac{\delta}{4}\right) D\right) \exp\left(-\frac{2\tau}{T_2} - \frac{\Delta - \tau}{T_1}\right). \quad (2.3)$$

To isolate the attenuation of the signal by the diffusion factor we normalize it. Normalizing the signal with respect to that obtained with the gradient off will result in the Stejskal and

Tanner equation [61]:

$$\frac{S_{(g)}}{S_{(0)}} = \exp\left(-\frac{4}{\pi^2}\gamma^2 g^2 \delta^2 \left(\Delta - \frac{\delta}{4}\right) D\right). \quad (2.4)$$

In order to validate the diffusion measurements obtained by PFG-NMR, many researchers use the Nernst-Einstein relation (Eq. 1.15) to calculate molar conductivity by using the measured  $D$  coefficient. These derived conductivities are compared to measured conductivity values from impedance measurements. These values are typically in agreement for highly diluted solutions. In the case of higher concentration solutions ( $< \sim 0.5$  M) NMR diffusion typically predicts higher conductivity values because, as stated before, without knowing  $z_{\text{eff}}$  the Nernst-Einstein relation does not account for associated ionic species that do not contribute to the conductivity [56].

## 2.2 eNMR

The concept of using NMR to measure field assisted transport was initially recognized by Packer in 1969 [64]. But the first successful experiments were made more than a decade later in 1982 by Holtz *et al.* [65]. Experimental limitations, especially artifact currents, have left the field of electrophoretic NMR (eNMR) to slowly develop. eNMR has almost exclusively been developed for solution NMR, mostly because of the difficulty in measuring long diffusion times for samples with short  $T_2$ . In addition, diffusion in solids is in general much slower and requires higher gradient strengths to be observed [66].

The measurement of ionic mobility under an electric field is slowly developing and has just recently been commercialized (2013- solutions only [67], based on Hallberg *et al.* [68, 69]). It is still considered an exotic technique that is performed in only a handful of labs around the world.

### 2.2.1 Signal Evolution

By adding the electric field to the diffusion time of diffusion NMR pulse sequences, it is possible to measure the drift velocity ( $\nu$ ) as a coherent flow like motion with  $\nu$  determined by the electric field strength and  $\mu$ . As in the PFG-NMR experiment, the spatially dependent Larmor frequency is  $\phi = \omega_0 + \gamma g \delta z_{(t)}$  only now the position,  $z_{(t)}$ , is dependent on the velocity of the spins according to  $z_{(t)} = \nu t$ , so the phase accumulated over time is  $\phi = \omega_0 + \gamma g \delta \nu t$ .

The signal amplitude is then affected by both the flow process and thermal diffusion, and is given by [65]:

$$\frac{S_{(g)}}{S_{(0)}} = \exp\left(-\frac{4}{\pi^2} \gamma^2 g^2 \delta^2 \left(\Delta - \frac{\delta}{4}\right) D\right) \times \cos(\gamma g \Delta \delta \nu), \quad (2.5)$$

or by plugging in the definition of  $\mu$  from Eq. 1.8

$$\frac{S_{(g)}}{S_{(0)}} = \exp\left(-\frac{4}{\pi^2} \gamma^2 g^2 \delta^2 \left(\Delta - \frac{\delta}{4}\right) D\right) \times \cos(\gamma g \Delta \delta \mu E). \quad (2.6)$$

In order to extract the electrophoretic mobility,  $\mu$ , the measured phase shift from the presented eNMR pulse sequence (Fig. 2.3) is isolated to:

$$\phi = \gamma g \Delta \delta \mu E \quad (2.7)$$

As we've seen in the previous section, the stochastic process of self-diffusion causes a dephasing of the signal and therefore results in attenuation. In the case of coherent flow, driven by the electric field, the flow is constant, directional, and time dependent and therefore results in phase modulation. This phenomenon can be compared to a constant, slow rotation of the NMR signal, similar to chemical shift, and therefore the result is a

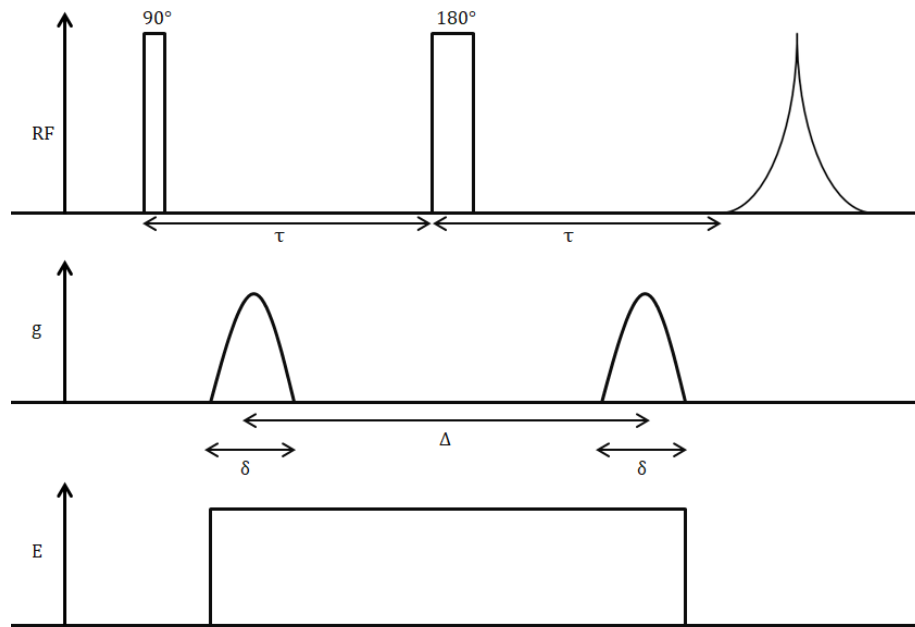


Figure 2.3: Spin echo eNMR pulse sequence diagram. An electric field is applied for the duration of  $\Delta$  can be seen in row E. [65]

phase modulation. As the spins are moving to a slightly different position in the magnetic field gradient, they have a slightly different Larmor frequency, similar to the explanation of a phase shift from the receiver being offset from the rotating frame. From this signal phase modulation, we can learn both the extent and directionality of the ion's motion.

As both self-diffusion and driven diffusion occur at the same time, an optimization of the evolution time  $\Delta$  is necessary. Other than the applied electric field, all the parameters that affect the magnitude of the phase modulation are also responsible for the loss of signal resulting from self-diffusion. Increasing the applied field time will, therefore, decrease the signal to noise ratio and might leave us with unmeasurable data. The same will happen when increasing the gradient strength or gradient pulse time. In order to achieve a useful eNMR measurement, a minimal drift velocity  $\nu$  must be obtained and other time related

parameters need to be carefully optimized.

### 2.2.2 eNMR Limitations and Probe Design Solutions

One of the major challenges in obtaining accurate eNMR data lies in the presence of artifact flows. Any flow that does not arise from the electrophoretic process is considered an artifact. Due to the integrative nature of NMR, it acquires an average of all the spins present in the detection volume. Therefore, all motions present in the coil in between the two gradient pulses are averaged and any non-electrophoretic currents are also averaged into the NMR signal. Overcoming this challenge has led to the design of several eNMR-specific sample cells and pulse sequences to help reduce typical artifact flows or minimize their effects on the signal. Both the common artifact flows and typical methods to overcome them are described in this section.

There are two common approaches to a sample holder for the suppression of non-electrophoretic motion, each with its own advantages and disadvantages. One is based on a U-tube cell that holds the electrodes above the RF coil. This set-up is useful for several reasons but suffers from a low fill factor and an inherent mixture of the mobilities' direction. Because both arms of the U-tube are inside the RF coil, the charged ions move in opposite directions in each of the arms, making it impossible to distinguish the direction they are moving (see Fig. 2.4a, [70, 71, 72]). The other successful approach is based on a vertical capillary tube array (see Fig. 2.4b, [73, 58]). This set-up does not require unique glasswork and has a much higher fill factor. It can distinguish directionalities of  $\mu$  but suffers from other artifact flows as the electrodes pass through the detection volume. In this section, the challenges will be further described together with solutions that are based on these sample cells.

An inherent problem when adding any currents near the RF coil is the noise pick up

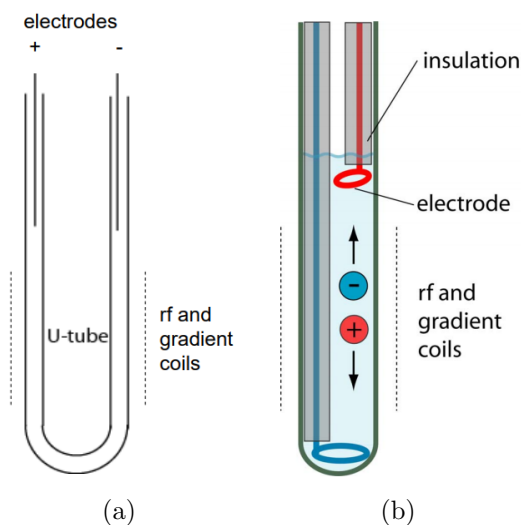


Figure 2.4: Conventional arrangements for eNMR sample cells. (a) U-tube sample cell. (b) Vertical sample cell. The distance between the electrodes is roughly 3 cm. Taken from Furó *et al.* [74]

because the probe acts as an antenna. The closer any part of the leads or the electrode are to the RF coil, the more noise the antenna will pick up. Usually, this is a major issue as most eNMR probe designs require the electrodes to be inside the RF coil area. The U-tube cell design overcomes this issue by setting the electrodes as far from the RF coil as possible, and by not having any leads pass through it. In comparison, the vertical sample cell has an insulated lead passing through the coil. This set-up still works well by setting the electric field axis as coaxial to the RF coil and thus perpendicular to the RF radiation direction, minimizing the noise pick up by the coil [75]. Another solution to overcome some of the noise pick up in a vertical sample cell is the usage of an RF interference filter, as made by Hallberg *et al.* [73, 68]. This filter system consists of a large ground box that is similar to a one-point ground for the leads transferring the electrophoretic inducing current and a low pass filter.

Artifact flows arising from thermal convection are one of the major issues of using the

*eNMR* technique. Even in a standard solution NMR experiment, a temperature gradient will result in uneven relaxation processes throughout the sample and results in distorted spectral lines. In *eNMR* experiments, the electrophoretic current passing through the sample will cause resistive heating according to Joule's first law: [45]

$$Q = I^2Rt = IVt \quad (2.8)$$

where  $Q$  is the produced heat,  $I$ ,  $R$  and  $V$  are the current, resistance and voltage respectively and  $t$  is the current duration. This tends to be an important source of heat in comparison to heat resulting from RF and gradient pulses. Although they can be important, those tend to be small due to low duty cycles while the duty cycle of the applied electric field is often much greater.

There are two major sources of resistive heat in an *eNMR* sample cell. In the point of contact between the sample and the electrode there is an increase in resistance as a result of the edge properties of both materials and the change between two types of current conductors. The second source of heating comes from the conductivity of the sample. Higher conductivity samples can support an increased current,  $I$ , when a given voltage is applied. They therefore can produce an increased amount of heat in the sample. Although resistive heating is relatively even throughout the sample, due to contact with the tube glass walls, which serve as a heat sink, the temperature of the sample in contact with the tube may not be equal to the centre of the sample. The variety of areas with increased heating or increased heat capacity create a temperature gradient along the sample. This temperature gradient causes a viscosity ( $\eta$ ) and a density gradient in the sample which lead to artifact flow, mostly in the direction parallel to gravity. In addition, the change in  $\eta$  will cause a change of both self-diffusion and mobility coefficients which will not be consistent for the entire sample, resulting in erroneous results. This is a significant limiting

factor for eNMR and until recently, the voltages used were very high (up to 1 kV [76, 72]) and therefore samples were usually preferred to not exceed 50 mM in concentration to limit their conductivity [77, 78]. One of the solutions to this uneven cooling is setting the sample in a polymer. By setting the sample in a polymer network, a mesh of heat sink that is in direct contact with the entire sample is created. This has two major benefits: 1) The higher thermal conductivity of the polymer helps to keep the temperature across the sample uniform and 2) the polymer reduces bulk flow from any remaining sources. The method of setting the sample in a stabilizing gel to minimize convection and heating of the sample has proved to be effective but can only provide mobility coefficients of ions embedded in a polymer network [78].

Another way to minimize the effect of convection currents is the use of capillary tubes. As can be seen in Fig. 2.5, a capillary tube array can be added to either type of conventional eNMR cells. This solution was originally implemented by He *et al.* in an attempt to investigate proteins in highly conductive buffer solutions [70]. This capillary tube array breaks bulk convective current pathways and does not allow them to develop and affect the eNMR signal. When implemented in a vertical cell as was done by Zhang *et al.* [58] and Gouverneur *et al.* [79], the background convective flows are broken. This vertical set-up also helps to increase the fill factor in the coil and by that increase the signal to noise ratio.

In practice, many repetitions of the experiment are needed to achieve sufficient signal to noise ratio. Without care, heat may accumulate along with the accumulation of signal. Precautions such as constant cooling of the sample, increased relaxation delays between experiments, and temperature control in the probe can help minimize the effects of resistive heating by keeping the temperature of the sample constant.

What seems to be the biggest issue in the implementation of eNMR is artifact flow that arises not from convectivity, but from electro-osmosis; bulk solvent motion generated by an

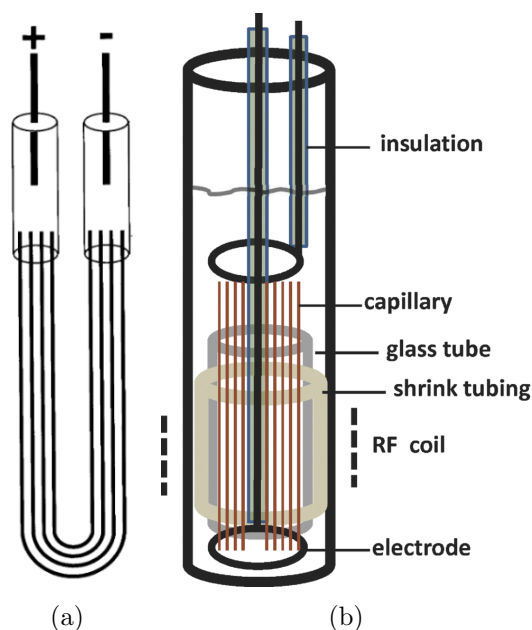


Figure 2.5: Conventional sample cells with capillary tubes added. (a) is taken with permission from [70] and (b) with permission from [58].

externally applied electric field on an ionic solution. As has been discussed in Section 1.1.1, ions in solution interact with solvent molecules to form a Debye layer of counter charge around a charged particle. A similar phenomenon occurs at the interface between charged surfaces and solutions, such as in the case of the sample holder glass wall. Due to Coulomb attractions, a fixed layer of counter-ions is built up against the charged surface of the glass wall. A bit further from the surface, a diffusive layer of ions is formed. This layer also has some net charge but is only loosely attracted to the surface and can diffuse easily. These two layers are called the electric double layer. When an electric field is applied, the diffusive layer will migrate, carrying the solvent molecules with it. Unlike an electrophoretic migration, this will result in bulk flow of the neutral solvent.

There are several techniques to overcome electro-osmosis in eNMR experiments. One is decreasing the glass surface charge by either coating it with an anti-electroosmotic coating

(*e.g.* poly(acrylic acid), polyimide or using a poly(methyl methacrylate) (Perspex) tube instead of glass [75, 79, 80]). The charged surface does not result in electro-osmotic flow beyond 10 nm in high dielectric constant solutions [81]. Therefore, in tubes with large enough volumes, the ratio of surface area to volume is low enough to only affect a small number of molecules and the effect is minimal. For narrow tubes, such as the U-tube sample cell and capillary tubes, the effect is more prominent and a high quality coating is required to suppress such flow.

Another potential issue in eNMR experiments is triggering electrochemistry for the experiment's components. The application of voltage on a chemical sample can induce electrochemistry, depending on the sample itself and the electrodes' material. If the electrochemical window of any of the materials in the sample is exceeded, redox reactions will take place and result in chemical changes to the species themselves, their concentration, or the composition of the electrode. Electrochemistry might also cause the production of gas at the electrodes, resulting in another artifact flow as gas bubbles try to escape the sample in the opposite direction to gravity causing turbulence that is greater than the effects anticipated from the electrophoresis. This is especially an issue for samples containing solvents and does not usually cause an issue when using pure materials, such as pure RTILs. One solution as suggested by Stilbs *et al.*, is using palladium as the electrode. It is known that Pd absorbs hydrogen at interstitial octahedral sites of its face-centered cubic lattice [82, 83]. Using Pd electrodes can trap hydrogen as it is generated at the electrode and by that eliminates bubble formation. Another solution to bubble formation is to have the electrodes above the detection volume, such as in the U-tube shaped sample cell. This will ensure any flow and turbulence caused by the bubbles is above the detection volume and does not affect the NMR signal. In the case of severe bubble formation, a non-conductive gas gap might form in the sample, creating an electric blockage that will

stop the electro-migration. For the specific case of the U-tube cell used with water as a solvent, electrochemistry causes a unique problem. For water, both electrodes will produce gas, but at different volumes. This unbalanced gas production can cause a displacement of the whole water column in a U-tube shaped sample holder. To avoid these issues, both the voltage and the type of electrodes must be selected carefully.

More options for the suppression of bubble formation can be learned from the field of capillary electrophoresis in mass spectrometry as they deal with directional currents as well [84].

### 2.2.3 Pulse Sequence Based Solutions

One of the ideas to suppress artifact flows that do not depend on the direction of the applied current, is to use a convection-compensated eNMR pulse sequence as suggested originally by He and Wei [85] and used by many others [86, 75, 73, 58, 57]. The pulse sequence is shown in Fig. 2.6. This extension of the original eNMR pulse sequence can distinguish between migration that does or does not depend on electric field ( $\nu_E$  vs.  $\nu_{\text{eff}}$ ). By splitting the electrophoresis diffusion time into an even number of sections, while alternating the direction of the applied electric field, one type of migration will cancel out. This pulse sequence is similar in concept to a Carr–Purcell–Meiboom–Gill (CPMG) echo train [87, 88].

The phase after the first diffusion block (see Fig. 2.6) is a result of a combination of the two migrations,  $\phi = \gamma g \delta \Delta (\nu_E + \nu_{\text{eff}})$ . Flipping the magnetization using a  $\pi$  pulse results in a phase of  $\phi_1 = \gamma g \delta \Delta (-\nu_E - \nu_{\text{eff}})$ . At the even numbered diffusion block, the applied electric field is reversed in direction and so does  $\nu_E$ . Any flow that arises from a process that is not-electric field driven will not change direction. The phase for the even diffusion blocks is  $\phi_2 = \gamma g \delta \Delta (-\nu_E + \nu_{\text{eff}})$ . At the end of the pulse sequence, the total phase arising from the flow processes will be a summation of both blocks  $\phi = \phi_1 + \phi_2 = -2\gamma g \delta \Delta \nu_E$  or

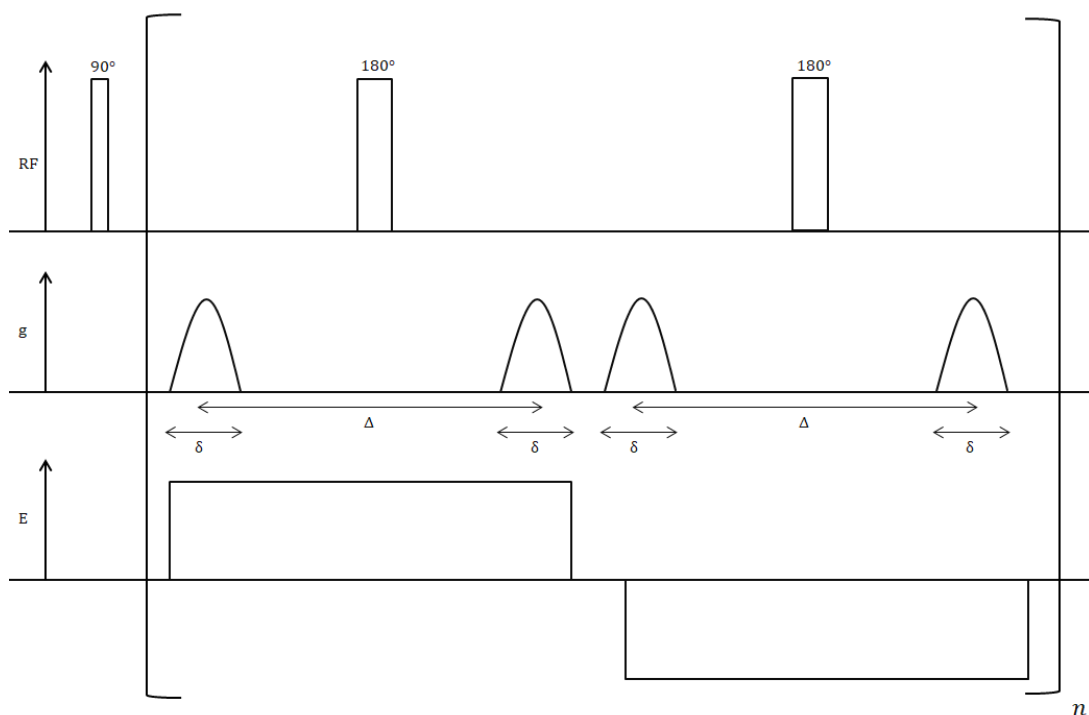


Figure 2.6: Artifact flow suppression CPMG-eNMR pulse sequence diagram.

for  $n$  repetitions-  $\phi = -n\gamma g\delta\Delta\nu_E$ . Notice that the magnitude of the cancelled flow does not matter and can be much larger than the electrophoretic flow. This allows for small motions arising from electrophoresis to be distinguished in a cloud of noise from other migrations. By increasing the number of inversions in the pulse sequence,  $\Delta$  can be decreased. This allows us to avoid acquiring after the flow in the sample has reached an equilibrium state in which the species are no longer flowing.

Because of the extended time the magnetization spends on the transverse plane, CPMG based pulse sequences will not be useful for samples with fast  $T_2$  relaxation. To overcome this limitation, the echo pulse can be replaced with a stimulated echo. This pulse sequence will enable artifact flow suppression for samples with short  $T_2$  in the same manner as CPMG-eNMR. The major downside in using an STE is the loss of signal due to the fact

that with each STE, the signal is reduced by half. For this reason, it is useful only when using a minimal number of repetitions. For the case of  $n=2$ , this pulse sequence is known as the Double STE eNMR pulse sequence (DSTE) [75] and is shown in Fig. 2.7.

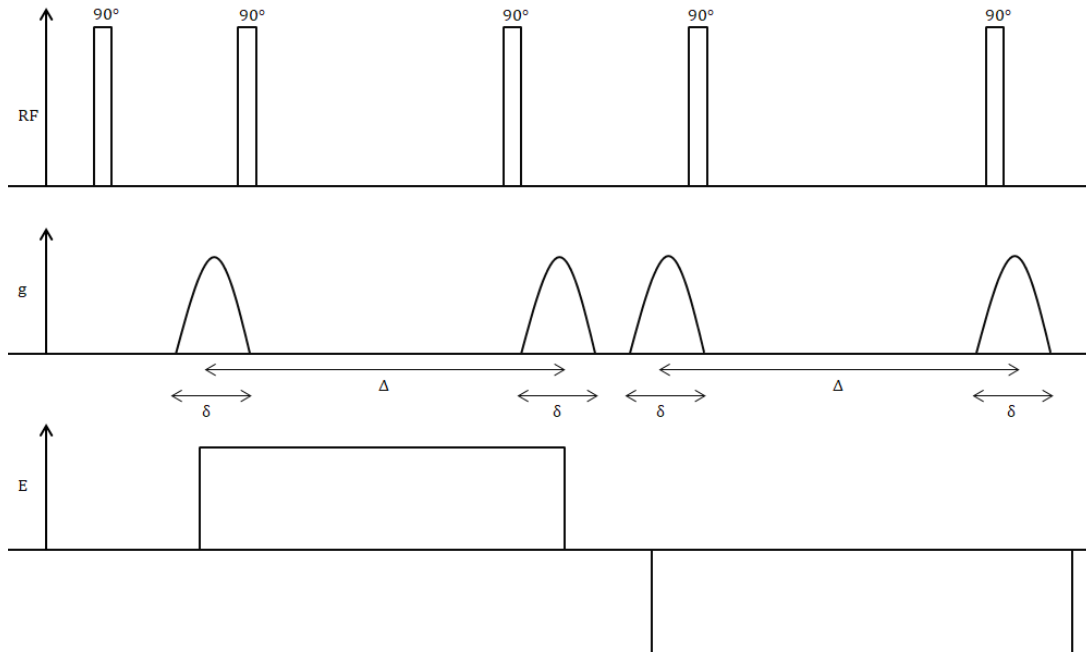


Figure 2.7: Double Stimulated Echo-eNMR pulse sequence diagram.

Although these pulse sequences can theoretically suppress any current artifact that is independent of the electric field, one must remember two hardware limitations. 1) heating is an accumulative process independent of the sign of  $E$ . A temperature difference between the two sections might cause a migration difference 2) an RF coil is far from being completely homogeneous and so the applied pulses are not perfect, that is, not perfectly  $\pi$  or  $\frac{\pi}{2}$  for all the spins in the sample. These limitations will prevent a complete suppression of the artifact flows.

In this chapter, an overview has been presented of the well-established method of PFG diffusion NMR, which is used extensively in the measurements described in Chapters 4-7.

The state-of the art of the emerging technique of *eNMR* has also been reviewed, and lays the foundation for work done in this dissertation to build (Chapter 3), validate (Chapter 3) and apply (Chapter 5) a simple new design of *eNMR* probe that overcomes the most prominent artifacts of previous probe designs by virtue of its geometry.

## Chapter 3

# Magnetic Resonance Transport

## Measurements: Methods

Experiments presented in this dissertation were performed using a variety of NMR probes, spectrometers and magnetic field gradient systems. This chapter describes the systems that were used, the purpose and abilities for each of these set-ups, and their validation. We will start by describing the pre-existing systems, including the PFG-NMR set-up for self-diffusion measurements and in Section 3.5, describe the construction of a new probe and voltage application system for electrophoretic diffusion measurements.

### 3.1 NMR Spectrometers

Three NMR spectrometers were used in the experiments presented in this dissertation. Two of the spectrometers are based upon Oxford Instruments (4.7 T and 8.4 T), 89 mm vertical-bore superconducting magnets with electronics consoles that were designed and built in-house. The console for the 8.4 T system is described in detail in [89]. The wide bore magnets simplified the creation of unique probes and use a variety of magnetic field gradient units that are described in the following sections. Typical  $\frac{\pi}{2}$  pulse widths ranged between  $\sim 2\text{-}5\ \mu\text{s}$  for  $^{19}\text{F}$  and  $^1\text{H}$  to  $\sim 6\text{-}10\ \mu\text{s}$  for  $^7\text{Li}$ . The 8.4 T magnet, which was used for the vast majority of experiments presented, was shut down and recharged during 2017. The

$^1\text{H}$  frequency of the magnet's field was reduced from 363 MHz to 360 MHz. The frequency change was small enough that all probes and frequency generators handled with no issues.

The third spectrometer used is a commercial 9.4 T Varian Unity Inova NMR spectrometer. This spectrometer is equipped with a commercial temperature control unit in addition to a high resolution probe. This combination of temperature control together with a high resolution probe allowed us to acquire a specific set of  $^{19}\text{F}$ -NMR spectra, which is presented in Chapter 6. at varying temperature with relatively high resolution. The  $\frac{\pi}{2}$  pulse widths used in these acquisitions ranged between  $\sim 7$ - $10 \mu\text{s}$ .

## 3.2 Home built PFG Probe and Driving Circuit

The measurement of self-diffusion presented in chapters 4, 5, 6, and 7 was done using an existing PFG probe and resonance driver circuit. These were originally built by Tso and Michal [1] and improved by Michan [2]. This probe and driving circuit combination allows us to change the gradient coil current and, by that, the magnetic field gradient strength in the z-direction. The magnetic field gradient pulses produced by this circuit have a sinusoidal time dependence and are half a period long, as shown in Fig. 2.1. which allows for a complete shut-off at the end of the pulse. This ability minimizes interference and inaccuracies when measuring transport coefficients. Initially, the coil winding allowed for gradient pulses between a complete shut off to  $3090 \frac{\text{G}}{\text{cm}}$ . Rewinding of the coil in a more accurate and tight manner allowed us to increase the number of windings, increasing the maximal magnetic field gradient by about 20% to  $3642 \frac{\text{G}}{\text{cm}}$ . For further information regarding the magnetic field gradient coil design see A. Michan's MASc thesis [2].

The strength of this probe and driver circuit lies in the extremely short and strong gradient pulses. Strong magnetic field gradient is necessary to allow diffusion measurements in semi-solids and high viscosity samples. By using a high g, smaller diffusion coefficients

can be measured. The short gradient pulses allow  $\tau$  in the STE based pulse sequences to be shorter. The signal dependence of  $\tau$  can be seen in Eq. 2.3. By allowing it to be as short as 318  $\mu\text{s}$ , samples with short  $T_2$  can be measured. Combining these two benefits allows for diffusion measurements in semi-solid samples of diffusion coefficients as low as  $\approx 10^{-13} [\frac{\text{m}^2}{\text{s}}]$  [2, 90]. The signal attenuation for experiments performed using this gradient set with sinusoidal gradient pulses follows

$$\frac{S_{(2\tau)}}{S_{(0)}} = \exp\left(-\frac{4}{\pi^2}D\left(\Delta - \frac{\delta}{4}\right)\gamma^2\delta^2B_v^2V^2\right), \quad (3.1)$$

where  $V$  is the programmed voltage to the driver (between 0–30 V), and  $B_v$  is the relation between voltage and the magnetic field gradient. A calibration of the  $B_v$  parameter was done by measuring a known sample of 0.05 M tetramethylammonium hexafluorophosphate (TEAP) in propylene carbonate (PC) and resulted in  $B_v = 121.4 \frac{\text{G}}{\text{cm}\cdot\text{V}}$  or  $32.51 \frac{\text{G}}{\text{cm}\cdot\text{A}}$ . An example diffusion measurement of this calibration can be seen in Fig. 3.1.

### 3.3 Data Interpretation

In order to extract self-diffusion coefficients from the data, the peak of interest from each spectrum was integrated over its finite frequency width so the data points could be plotted as the peak integral vs. the magnetic field gradient strength. The error bars shown on the graphs were calculated as the root mean square (RMS) of the noise from the end of each free induction decay (free induction decay (FID)) measurement multiplied by the square root of the fraction of the spectrum integrated from the total spectral width. This is done to avoid the overestimation of error to the Fourier transformed spectrum. By multiplying the RMS noise with the square root of the fraction of the spectral width, we only account for the noise in the integrated area and not the entire spectrum. The data points were

### 3.3. Data Interpretation

then fitted to a Gaussian curve using MATLAB (2013a, The MathWorks, Inc., Natick, Massachusetts, United States). The self-diffusion coefficient was extracted from the fitted Gaussian curve parameters. In addition, the natural logarithm of each data point and its error was plotted against the magnetic field gradient strength squared to allow us to fit the data to a linear version of Equation 2.4. The linearized data points were fitted to a straight line using linear regression analysis. Fig. 3.1 shows an example for the two types of fits done.

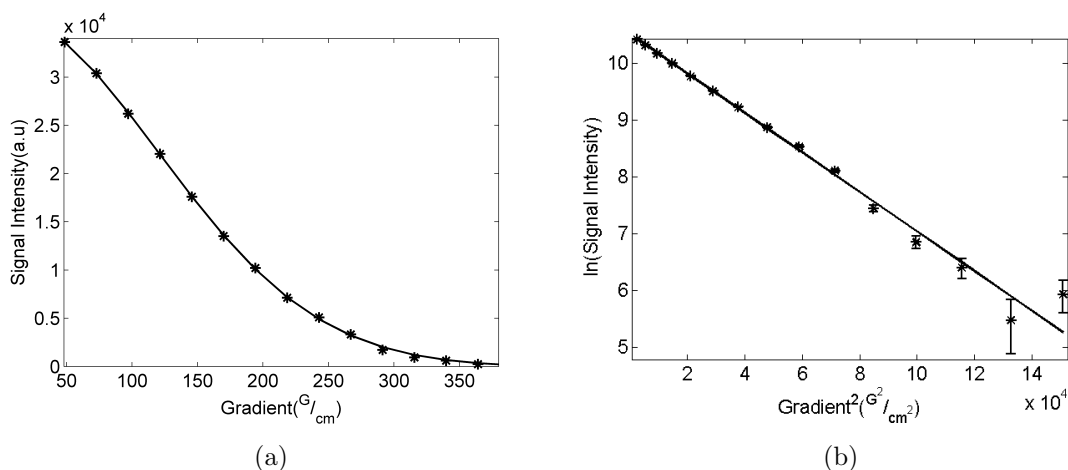


Figure 3.1: Relative signal intensity  $\frac{S_{(2\tau)}}{S_{(0)}}$  vs. magnetic field gradient strength of calibration sample 0.05 M TEAP in PC. The  $B_v$  coefficient was extracted by fitting the data to a Gaussian curve with the known diffusion coefficient [1]. (a) shows the single  $PF_6^-$  fluorine peak intensity vs. magnetic field gradient strength. (b) shows the same data, plotted as the natural logarithm of the signal intensity vs. magnetic field gradient strength squared to linearize the Gaussian behaviour of the Stejskal-Tanner diffusion equation (Eq. 2.4). Both figures show excellent fits to a single diffusion coefficient.

#### 3.3.1 Temperature Control

The probe was used previously for high temperature measurements, but before the work done in this dissertation, no measurements had been done below ambient temperature. In

### 3.3. Data Interpretation

order to perform experiments below room temperature, additional components were added to the temperature control system. The probe was connected to a Bruker temperature control system, B-VT-1000 to allow for temperature control of the samples. A glass dewar in the probe acted as an insulator allowing hot or cold air to travel to the sample without harming the probe body. A thermocouple placed at the end of the dewar, just below the sample, measured the temperature of the air as it reached the sample. This thermocouple was connected to the B-VT-1000 system and allowed for temperature feedback. To account for the difference between the air and the sample temperature, calibrations of the sample temperature were done using a sample of pure methanol ( $\geq 99.9\%$  VWR, CAS 67-56-1) [91].

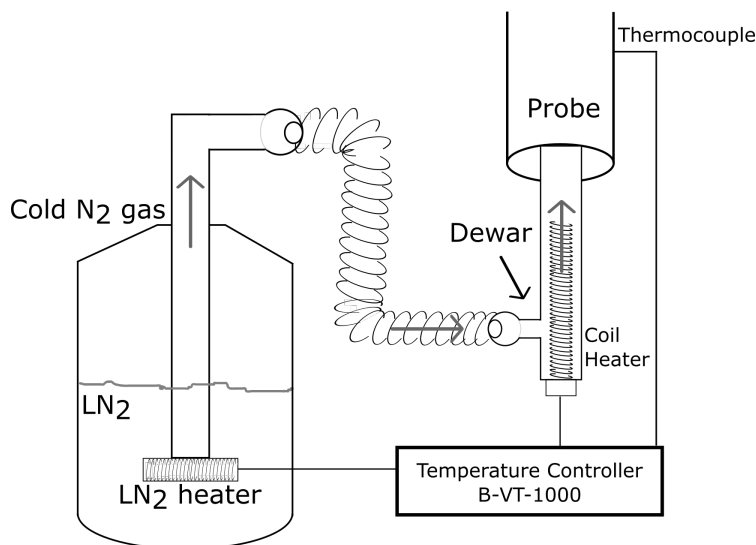


Figure 3.2: An illustration of the temperature control set-up. The cold N<sub>2</sub> gas, labelled as grey arrows, flows to the probe through an insulating glass dewar. B-VT-1000 temperature controller is connected to a thermocouple near the sample holder and controls both the coil heater in the glass dewar and the heater in the LN<sub>2</sub> dewar.

For heating, room temperature air flowing through the glass dewar was heated by a heating coil inside the glass dewar (see illustration in Fig. 3.2). For cooling, an external

liquid nitrogen (LN<sub>2</sub>) dewar was added to the temperature control system. The boil off gas from the LN<sub>2</sub> dewar was connected to the probe and flowed to the sample through the insulating glass dewar. In order to control the amount of nitrogen gas flowing to the probe, a heater attachment was placed inside the LN<sub>2</sub> dewar, controlling the amount of cold N<sub>2</sub> gas to boil off. Both the LN<sub>2</sub> heater and the coil heater in the glass dewar were controlled by the B-VT-1000. This combination of controlled cooling and heating extended the temperature range of the probe and allowed was able to maintain a constant temperature of anywhere between 200 and 380 K.

In order to avoid heating or cooling of the probe shield, an additional source of room temperature air was supplied to the area surrounding the gradient coil and sample. A double walled vent pipe was connected to the top of the probe to carry the hot or cold air out of the spectrometer in order to avoid heat transfer to and from the magnet.

## 3.4 Bruker Imaging 3-axes Gradient Set

An external imaging gradient set made by Bruker allowed us to measure both self and driven diffusion in multiple directions. This set-up was used in all eNMR measurements (see Section 3.5 and Chapter 5). This imaging set is made of a Micro2.5 gradient unit with a gradient sensitivity of  $2.5 \frac{\text{G}}{\text{cm}\cdot\text{A}}$  and a current amplifier system (Bruker BGR-II BAFPA 40) made of three gradient amplifiers capable of 40 A each. This allowed for a maximal  $100 \frac{\text{G}}{\text{cm}}$  magnetic field gradient in each of the three-axes and allowed us to control the shape of the magnetic field gradient pulses, expanding our set-up to more than just a sinusoidal pulse. Utilizing this gradient set allowed us to control the length, magnitude and direction of the magnetic field to high accuracy, but was limited to considerably lower magnetic field gradient strengths.

## 3.5 eNMR Probe Construction and Validation

While preexisting equipment was available for self-diffusion measurements, electrophoretic NMR measurements required the design and construction of a new probe. In this section we will go through the design, construction and validation of a sample holder which allows for eNMR measurements with minimal artifacts, at the expense of magnetic field homogeneity.

### 3.5.1 Introduction

As discussed in Section 2.2, electrophoretic NMR (eNMR) is a slowly developing method that was initially conceptualized by Packer in 1969 [64]. Even today, there is no industry standard for an eNMR probe design and a handful of labs around the world have implemented their own solutions to the common issues presented when trying to measure electrophoretic mobility using magnetic resonance methods. The following section describes the experimental setup constructed and used in all eNMR experiments presented in chapter 5. This setup has a few advantages when compared to other eNMR probes, especially for measuring high conductivity samples such as RTILs at different concentrations. These advantages enable the usage of a relatively simple sample cell, sacrificing magnetic field homogeneity while overcoming most of the known issues of solution eNMR that are described in detail in Section 2.2.2.

### 3.5.2 Methods

In order to overcome eNMR artifact flows and obtain accurate mobility measurements, a horizontal magnetic field gradient component of the Micro2.5 gradient set described in Section 3.4 was utilized. The horizontal gradient, which is perpendicular to gravity and to the direction of the main magnetic field,  $B_0$ , is also perpendicular to convective flows and bubbles that can cause artifacts. This enabled the construction of a probe

which is simple, inexpensive, and free from artifacts at the cost of static magnetic field homogeneity. A diagram of the probe can be seen in Fig. 3.3. In this simple design, two inert electrodes (either carbon glass or Pd wire) were dipped in the electrolyte solution. The sample itself was placed in a cut section of a standard 5 mm NMR tube, providing a large fill factor. In order to withstand high polarity solvents (such as PC), the sample holder was machined from polyoxymethylene which has excellent solvent resistance. The electrodes were positioned 3.4 cm from each other and kept at a relatively large distance from the RF coil (larger than half of the coil size) to minimize noise pick up. A comparison of signal to noise (SNR) between scans with applied current and without has shown an average of 20% decrease in SNR when current was applied. It was concluded that this slight decrease in SNR does not pose a significant issue. The electrodes were connected to a relatively low 50 V power supply with a constant current regulator ( $\sim 1$  mA) and an H-bridge, which allows control of the direction of current through the sample. This low, constant current allowed for steady state electrophoretic flow [58] with minimal heating, and the voltage sign switching, controlled by a micro-controller connected to the pulse programmer, made it possible to avoid the build up of charge at the electrodes which would stop the measurable flow. In order to ensure measurement of flow in the steady state, the electric field was initiated 200 ms before the pulse sequence started and was cut off after the signal acquisition was done. External air cooling was added under the sample to minimize changes in  $\mu$  due to resistive heating which would cause changes to the sample's viscosity. The 3-axis gradient set (Bruker BGU BAFPA 40) had a maximum gradient strength of  $100 \frac{\text{G}}{\text{cm}}$  along each axis and was used in a direction parallel to the direction of the sample cell and electrophoretic motion.

When voltage is applied, the ions in the sample migrate to the oppositely charged electrode. The constant drift velocity for the ions is reached when the drag force is equal

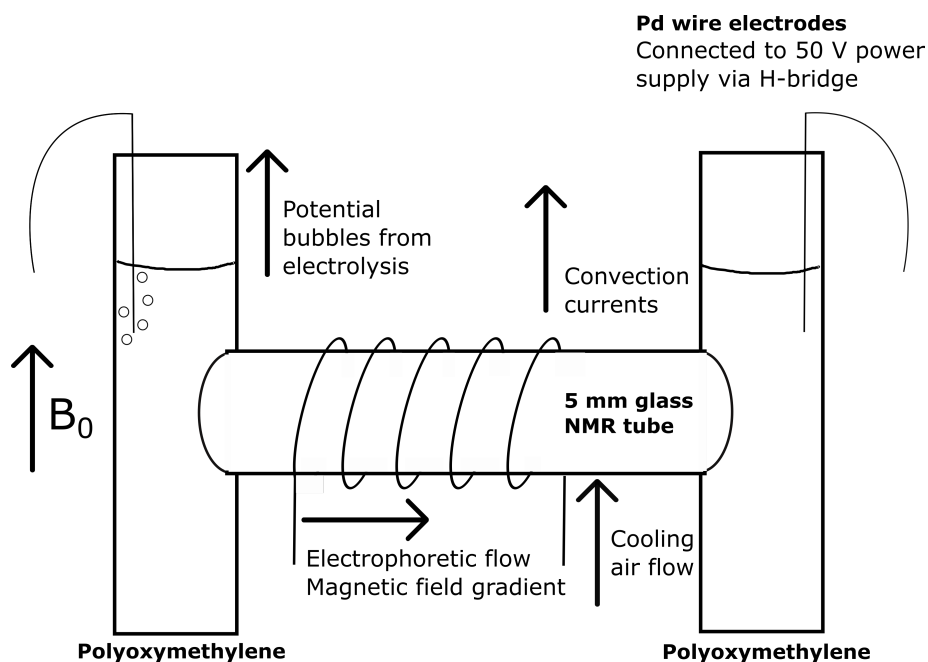


Figure 3.3: Diagram of our simple, horizontal home-built eNMR probe and sample holder.

to the driving force, a very quick process which happens almost instantly (ns) [92]. The ions in the sample continue to flow as long as the electric field is not masked by the ions in solution. As the electric field is applied, the ions begin to migrate in the direction of the oppositely charged electrode (Fig. 3.4). This flow in a direction perpendicular to the static magnetic field,  $B_0$ , may give rise to an ionic Hall effect. This would result in a slight redistribution of the ions in a direction perpendicular to the measured flow, and thus have minimal effect on the measured signal. As the ions flow from one electrode to the other, they accumulate near the electrodes and a concentration gradient grows in the opposite direction of the electrophoretic flow. When the total charge of the ion layer is equal to the charge at the electrode an equilibrium is reached. The diffusion resulting from the concentration gradient is equal to the electrophoretic migration; the total flow of ions will stop [93]. This migration time constant,  $\tau_{eq}$  is unique to each sample as it depends

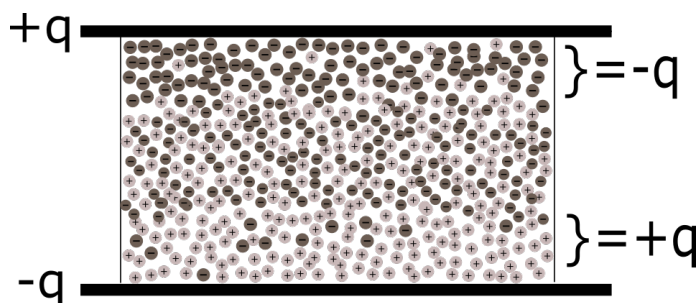


Figure 3.4: Diagram of the charged particle distribution in the sample at the undesired equilibrium state in which no electrophoretic flow occurs.  $q$  represents the charge on the electrode. The electric field is masked by the layer of ions close to the electrode surface.

on the sample size, ionic strength, and the applied electric field strength. This state of equilibrium is avoided when the ions undergo electrochemical processes at the electrode in a process similar to that seen in an electrochemical cell [94]. In this scenario, the migrating ions undergo a redox reaction at the electrode, charge accumulation is avoided, and the electrophoretic migration continues.

A constant current regulator was used to ensure that the speed of the ions remains constant for the duration of the experiment. This regulator will make adjustments to the voltage if the resistance of the sample changes, resulting in a constant current flowing through the sample. This both helped to make sure no minor fluctuations of the ion flow occurred during the experiment and helped us to confirm no equilibrium was reached. An external voltage measurement showed that after a rise time of  $\sim 100$  ms, the voltage remained constant, indicating no state of equilibrium was reached.

In order to avoid the effects that charge accumulation might have on the experiments presented in Section 3.6 and Chapter 5, two precautions were taken. One was to switch the direction of the applied voltage in between acquisitions [85, 79, 95]. The other was to wait a significant amount of time (at least 10 s) in between scans to allow for diffusion driven

by chemical gradient enough time to restore equilibrium [58, 68, 57]. This long delay also helps to reduce resistive heating (as discussed in Section 2.2.2). The pulse sequences can be seen in Fig. 3.5.

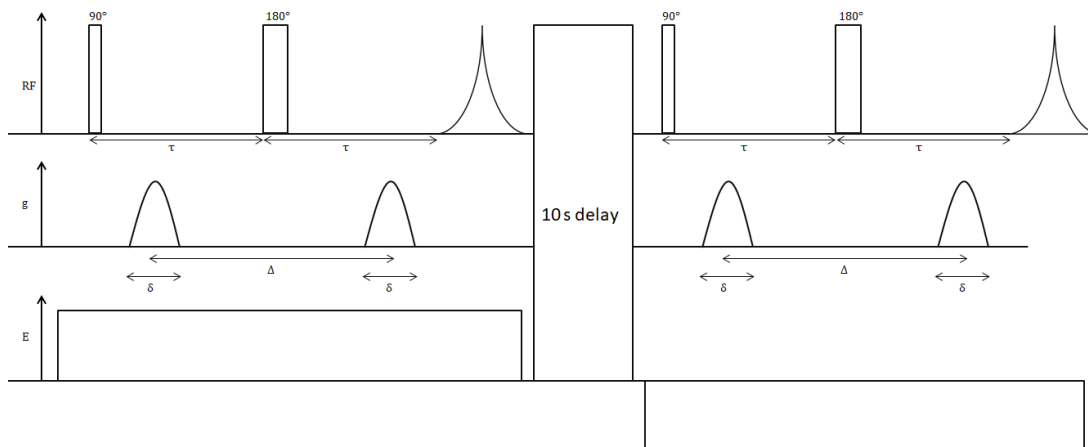


Figure 3.5: eNMR pulse sequence diagram. The polarity of the applied voltage is reversed between scans and the delay between scans was on the order of 10 s to allow the ions to return to equilibrium.

### 3.6 Data Interpretation

The zeroth order phase was extracted from the data by plotting the phase of the free induction decay (FID) as a function of time and fitting to a line. The zeroth order phase was taken as the intercept of the line at time zero. The uncertainty in the measured phase was less than one degree. Together with the uncertainty in the voltage measurements, the average mobility error was  $\approx 5\%$ .

### Results and Discussion

This experimental setup and pulse sequence allowed us to measure the phase shift of the NMR signal in response to an externally applied voltage. The measured phase is dependent

on the ions' displacement  $\phi \propto \nu t$  and therefore on the magnitude and direction of the applied current. An example of the resulting phase shift can be seen in Fig. 3.6. Fig. 3.6a shows the positive zeroth-order phase shift caused by the application of the required voltage to allow for a positive current of 1.06 mA. Fig. 3.6b shows the response of the NMR signal to the same magnitude of V but in the opposite direction. It is easy to see the inversion of direction in the zeroth-order phase shift, caused by the inversion in migration direction for the NMR visible ion.

The extent of the measured phase can be seen in Fig. 3.7 as the phase difference vs. the applied current. The measured phase showed an excellent linear correlation to the applied current. The magnitude of the measured phase increases with an increase in current magnitude. When no current was applied, the measured phase remained unchanged. From the measured phase we can extract the distance the ions passed during the experiment. In combination with measured electric field, this distance allows us to extract the electrophoretic mobility coefficient,  $\mu$ , using Eq. 2.7. Using this set-up we measured ionic movement in the range of  $\sim 10\text{-}80\ \mu\text{m}$  and measured mobility constants in the range of  $\sim 8.5 \cdot 10^{-12}$  to  $1.5 \cdot 10^{-8}\ \frac{\text{m}}{\text{V}\cdot\text{s}}$ . This large range of mobility is necessary in order to investigate conduction mechanisms of ion dense materials.

#### 3.6.1 Conclusions

These measurements show that electrophoretic driven transport can be measured in ion dense solutions with relatively high conductivity. The validation of this probe has shown that by using a simple eNMR probe in combination with a horizontal magnetic field gradient set, it is possible to minimize the effects gravitational artifact flows on the measured signal. Using this eNMR set-up, we are able to separate flow that is driven by the external electric field.

### 3.6. Data Interpretation

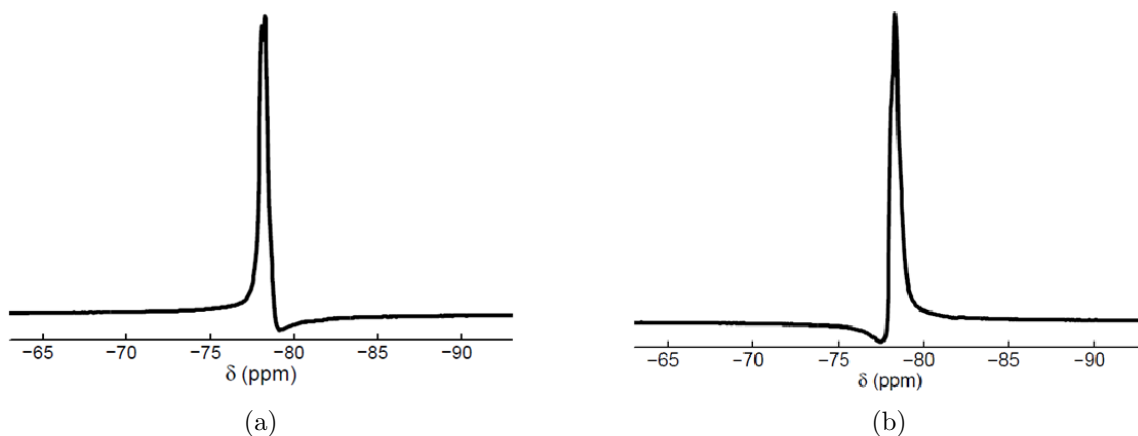


Figure 3.6:  $^{19}\text{F}$ -NMR spectra of 2.0 M LiTFSI in PC under applied voltage, performed at  $22^\circ\text{C}$ . The constant current was kept at (a)  $+1.06\text{ mA}$  or (b)  $-1.06\text{ mA}$ . Notice the inversion in zeroth-order phase in response to the reverse direction of ionic electrophoretic flow.  $\Delta\phi = 17.25^\circ$  and the calculated distance the ions have passed during the experiment was  $\sim 39.8\ \mu\text{m}$ .

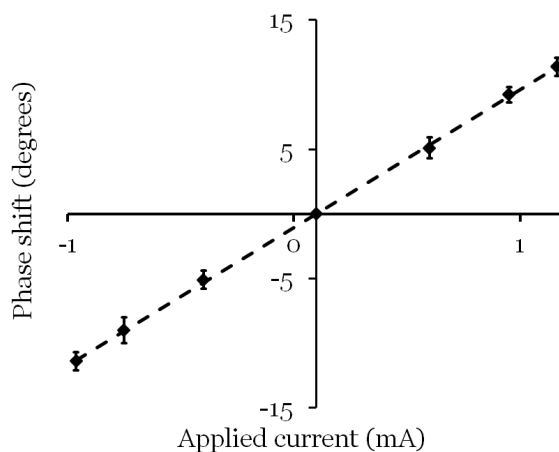


Figure 3.7: Acquired zero<sup>th</sup> order phase vs. constant current shows an expected linear relation between flow and phase according to  $\phi = \gamma g \Delta\delta \mu E$ . The direction of the phase changed as the direction of the applied current was changed. When no current was applied, the phase shift remained zero. Mobility was extracted from the linear fit and calculated to be  $2.49 \cdot 10^{-8} \frac{\text{m}}{\text{V}\cdot\text{s}}$ .

## Chapter 4

# Diffusion of EMI-TFSI Dilutions in Propylene Carbonate

### 4.1 Introduction

Iontronics are devices based on the conductivity of ions, in contrast to electron conductivity which is used in electronics. Driven by energy storage needs, flammability concerns, and the potential for novel new devices, interest in ion dense ionic conductors continues to increase [96, 97]. Ionic electroactive polymers (IEAPs) are a class of ionic-mechanical transducers composed of an ionic conducting membrane swollen with electrolyte. These are used to create actuators that can convert applied voltage to mechanical work and can also work in reverse by behaving as sensors that can convert mechanical deformation to measurable voltage. This ability to act as an actuator and a sensor, together with their general softness, soundless operation, light weight, and low operating voltage are all properties that have made IEAPs promising candidates for artificial muscles and as mechanical stress sensors [98].

The sensing and actuation behaviours are attributed to the newly termed “piezoionic effect” which has been previously observed, but its mechanism is still under investigation [99, 100, 101, 102]. A suggested mechanism attributes the produced voltage to the differences in diffusive properties of oppositely charged ions. Upon pressure application,

the movement of the ions is not necessarily equal. If one ion moves faster than the counterion, temporary charge separation is created and this potential difference can be measured. In Fig. 4.1 a diagram of an IEAP based sensor device is shown. The mechanical motion of a lever arm can be measured using IEAP that is in direct contact with two conducting electrodes. When the level arm moves and bends the IEAP, voltage is generated across the IEAP. The electrodes, which are connected to a potentiostat, can measure the generated voltage and quantify the extent of the arm motion. Research by Woehling *et al.* using RTILs as potential electrolytes for actuators revealed an interesting phenomenon.

As previously measured by Tokuda *et al.* [59], self-diffusion measurements of neat 1-ethyl-3-methylimidazolium-bis(trifluoromethylsulfonyl)imide (EMI-TFSI) displayed faster diffusion for the cation ( $\frac{D_+}{D_+ + D_-} > 0.6$ ) which is significantly smaller than the TFSI<sup>-</sup> anion. And indeed, film actuators built from an interpenetrating polymer network (IPN) of poly(ethylene oxide) (PEO) and nitrile butadiene rubber (NBR), swollen with neat EMI-TFSI have shown cationic behaviour. However, when actuators with different dilutions of EMI-TFSI with propylene carbonate (PC) as a co-solvent were fabricated, the displacement direction of the actuator changed and began showing signs of anionic behaviour as the direction of displacement reversed (see Fig. 4.2a). To confirm this inversion, open circuit voltage measurements in response to applied strain were performed on the samples, and indeed an inversion in the voltage direction was observed (see Fig. 4.2b).

It is believed that at the inversion point, the migration of the ions is equal, the sum of physical displacement in both directions is null. Interestingly, the maximum ionic conductivity was also observed at the inversion point (Fig. 4.3), suggesting that the maximum ionic conductivity occurs when transport numbers of the two ions are equal. The migration of the ions is expected to depend on the interactions between the ions. According to Dupont *et al.*, neat imidazolium-based RTILs form a supramolecular crystal-like structure that is

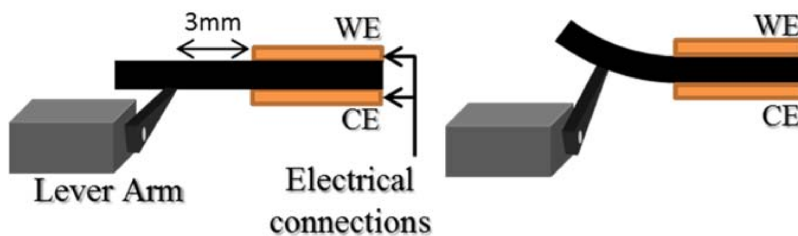


Figure 4.1: Experimental setup for sensor characterization. Figures show the sensor with applied stimulation (right) and without (left). The mechanical stimulation was applied at 3mm from the electrical contacts on the lower side using the Muscle Lever Arm 300 C, which means that during bending movement (right), the sensor side connected to the working electrode (WE) is contracted and the side connected to the counter electrode (CE) expanded. The copper electrodes are in direct contact with the IEAP and are connected to a potentiostat in such a way that the WE is always the upper one. Diagram is adapted from Woehling *et al.* [3].

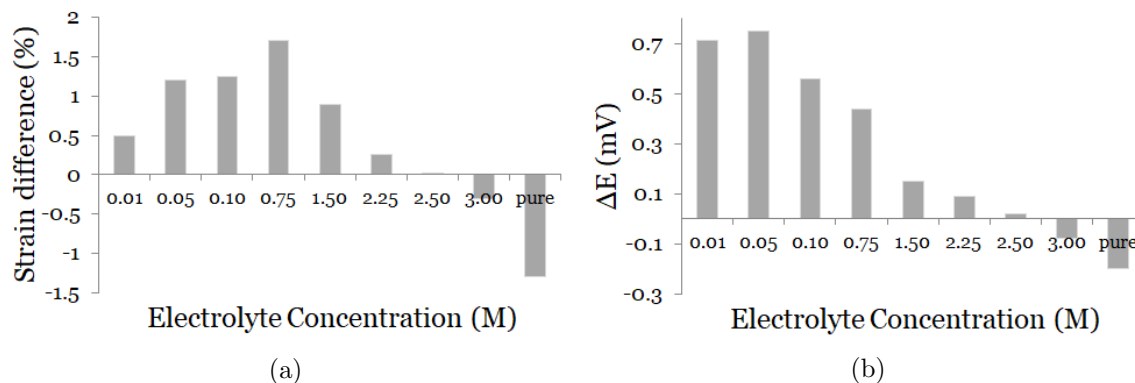


Figure 4.2: (a) Actuator mode strain response to applied potential of 2V. Notice the inversion in strain direction around 2.5M. (b) Open circuit voltage for different [EMI-TFSI] in PC in response to 4% strain. Notice the inversion in voltage direction around 2.5M [3]

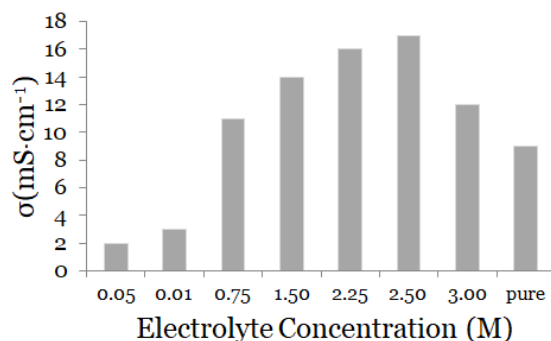


Figure 4.3: Ionic conductivity obtained by electrochemical impedance spectroscopy. Maximum is measured at the same concentration as the actuation inversion point.

based on hydrogen bonds (through the imidazolium hydrogens and anion's halide) [22, 103]. With the addition of a co-solvent, the correlation length of the supramolecular structure is reduced; the structure breaks down into smaller fractions of associated ion species such as triple-ions, contact ion-pairs, solvent separated ion-pairs, and, eventually, free ions. The level of separation is dependent on the polarity of the co-solvent as it masks the attraction between the ions [104, 105]. This suggested mechanism seems very intuitive and is known from the similar behaviour of electrolyte solutions [28] but due to the relatively short list of techniques that are able to investigate individual ions in RTILs, most RTIL/solvent mixtures behaviour remains speculative.

This chapter describes the self-diffusion measurements for the two ions of RTIL EMI-TFSI in varying concentration in PC solvent, both in IPN and in solution. The concentrations investigated were chosen according to the inversion point seen in the preliminary sensor measurements, to assure measurements of samples which are dilute, concentrated, and close to the inversion point. These measurements help us better explain the effect dilution has on EMI-TFSI association in PC.

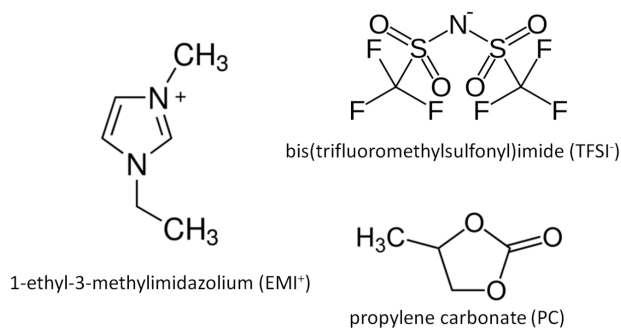


Figure 4.4: Structural formula of RTIL EMI-TFSI and co-solvent PC

## 4.2 Methods

High resolution  $^1\text{H}$  spectra of EMI-TFSI were collected using a high-resolution solution probe in a 400 MHz Varian Unity Inova spectrometer. For IPN samples NBR/PEO (40/60) rubber sheets were cut to  $4 \times 20 \times 0.25 \text{ mm}^3$  and soaked in the diluted solutions for a minimum of 48 hours before measurements. Two sheets were placed between glass slides and inserted into an NMR tube with the sheets positioned either parallel or perpendicular to the magnetic field gradient. PFG-STE experiments were performed at  $22^\circ\text{C}$  using a home-built PFG probe [2] in a home-built NMR spectrometer [89] operating at 8.4 T, which are both described in Chapter 3.

To track the individual ions,  $^{19}\text{F}$ -NMR was used for  $\text{TFSI}^-$  and  $^1\text{H}$ -NMR for  $\text{EMI}^+$ . The home-built horizontal diffusion probe has limited  $B_0$  homogeneity but excels in high gradient strengths that can measure slow diffusion of samples with short relaxation times. In combination with the high resolution solution spectra of the RTIL, it was possible to use the relatively well separated cation peaks around 7-10 ppm to track the motion of the ion, as well as the overlaying solvent peaks around 3 ppm to track the diffusion of PC. Diffusion measurements were made using the PFG-STE NMR pulse sequence (see Section 3.2 and Fig. 2.2 for the complete pulse sequence). A gradient pulse of  $\delta=318 \mu\text{s}$  was applied in

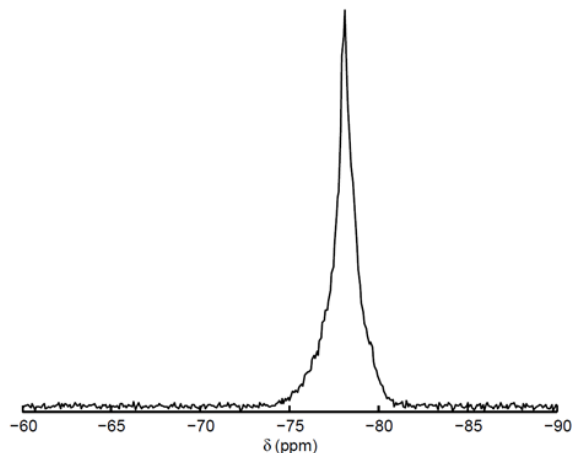


Figure 4.5: Example  $^{19}\text{F}$  spectra of 3M EMI-TFSI/PC in PEO-NBR IPN. The single TFSI $^{-}$  fluorine peak is shown at -79 ppm. Spectrum collected on the 360 MHz spectrometer using a home-built horizontal diffusion PFG-NMR probe.

varying strength from about  $g = 50 \frac{\text{G}}{\text{cm}}$  to  $1000 \frac{\text{G}}{\text{cm}}$ . For the samples soaked in NBR/PEO sheets, the diffusion is attenuated by the medium and required higher gradient strength. Gradients between  $g = 100 \frac{\text{G}}{\text{cm}}$  to  $2000 \frac{\text{G}}{\text{cm}}$  were used. The diffusion time  $\Delta$  was varied between 500 – 700 ms. An acquisition delay of  $T=20$  ms was used in order to allow eddy currents to decay before acquisition.

### 4.3 Results and Discussion

To track the individual ions,  $^{19}\text{F}$ -NMR was used for TFSI $^{-}$  and  $^1\text{H}$ -NMR for EMI $^{+}$ . The resulting spectra can be seen in Figs. 4.5 and 4.6, respectively. The lines in both spectra are generally broad due to the shorter relaxation times which are a result of the PEO-NBR polymer network [60]. In addition, the sample could not be well shimmed due to its geometry as it is made of individual films mounted inside a short horizontal section of a 5 mm NMR tube. Having a single peak spectrum with no background, the TFSI $^{-}$  ion was easily tracked by simply integrating the single peak. The same cannot be said for the

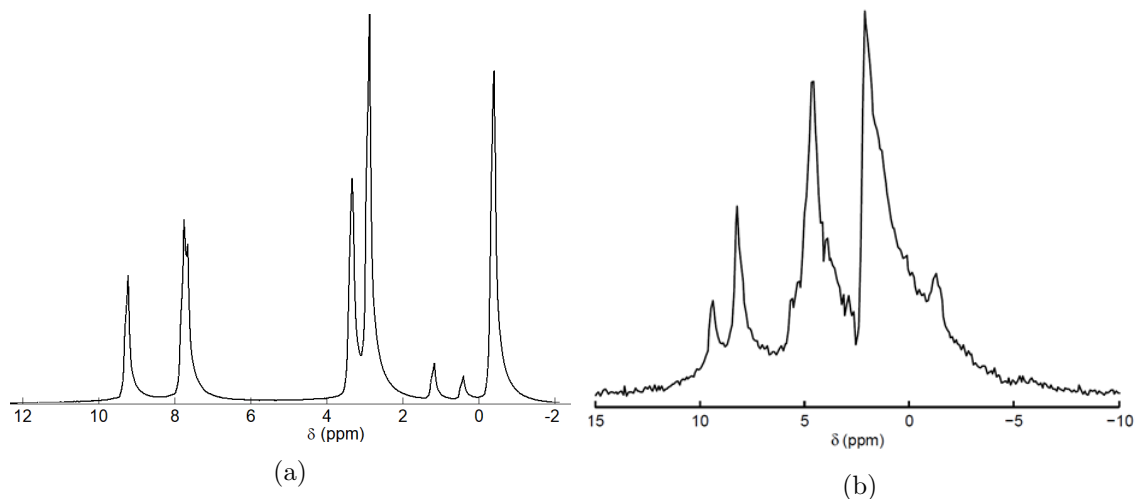


Figure 4.6: Example  $^1\text{H}$  spectra of 3M EMI-TFSI in PC (a) shows a solution sample and (b) shows the same sample, embedded in PEO-NBR IPN. (a) was acquired using a high resolution solution probe in a Varian Unity Inova 400 MHz spectrometer. The  $\text{EMI}^+$  protons are seen around 8 ppm and the PC protons around 3 and 0 ppm. (b) Spectrum collected on 360 MHz spectrometer using a home-built horizontal diffusion PFG-NMR probe and shows the  $\text{EMI}^+$  protons around 7 ppm and the PC protons around 3 and 0 ppm. The background signal from the PEO-NBR IPN is present in the spectrum and makes peak separation challenging.

proton spectrum. The  $^1\text{H}$  NMR spectrum contains more peaks, which overlap with the proton background from the solvent and the polymer network. To help separate the peaks of the cation from the solvent and polymer background, a solution spectrum of 3M EMI-TFSI in PC was collected. This spectrum can be seen in Fig. 4.6a. From this spectrum, which has an improved resolution, we can easily separate the  $\text{EMI}^+$  cation peaks from the solvent. By choosing to track the diffusion of the peak which is most separated from the background, around 8 ppm, we can separate the ion diffusion from the solvent and the polymer.

Self-diffusion coefficients ( $D$ ) were measured at room temperature for a set of different concentrations of EMI-TFSI/PC embedded in PEO-NBR IPN. The self-diffusion coeffi-

### 4.3. Results and Discussion

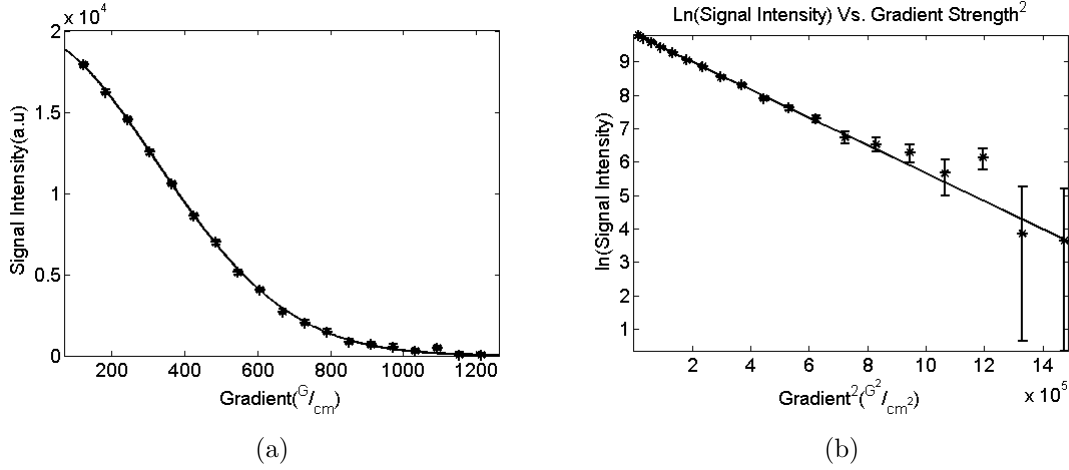


Figure 4.7: Example of a diffusion experiment for the anion, (TFSI<sup>-</sup>) of 2.50 M EMI-TFSI/PC in PEO-NBR IPN with a diffusion time  $\Delta = 375$  ms, performed at 22 °C. (a) shows the single TFSI<sup>-</sup> fluorine peak vs. gradient strength. The data is fitted to show a Gaussian decay of the signal with an increase in gradient strength. (b) shows the same data, plotted as the natural logarithm of the signal intensity vs the gradient strength squared to linearize the Gaussian behaviour of the Stejskal-Tanner diffusion equation. Both figures show excellent fits to a single diffusion coefficient of  $D = (4.71 \pm 0.05) \times 10^{-7} [\frac{cm^2}{s}]$ .

coefficients were extracted by fitting the signal intensity vs. magnetic field gradient strength to a Gaussian curve as described in Eq. 2.4. To further validate the fit, the natural logarithm of the intensity was plotted against the magnetic field gradient strength squared and modelled with a straight line. A typical data set can be seen in Fig. 4.7 where the data was well fitted to a single component Gaussian decay, indicating a single diffusion coefficient for each ion. The measured values for the two ions were of the same order of magnitude as typical self-diffusion coefficients for EMI-TFSI solutions observed previously [21]. For IPNs swollen with solutions, the values were again on the same order of magnitude as similar experiments done on EMI<sup>+</sup> embedded in ionic polymer conductor network composites [106] and for TFSI<sup>-</sup> in LiTFSI-PEO complexes [107].

Measurements were performed at two orientations and no notable differences in diffusion coefficients were detected between samples that were measured parallel to the magnetic

### 4.3. Results and Discussion

field gradient vs. perpendicular, indicating no structural anisotropy of the films. The experiment was repeated at different diffusion times for each concentration and the self-diffusion coefficients were averaged. Fig. 4.8 summarizes the self-diffusion coefficients of EMI-TFSI/PC with varying concentrations, both for solution samples and for IPNs swollen with solution. Table 4.1 shows the ratio of measured  $D$  for the two ions ( $D_+/D_-$ ). The self-diffusion of the co-solvent PC is presented in Fig. 4.11 and will be discussed below.

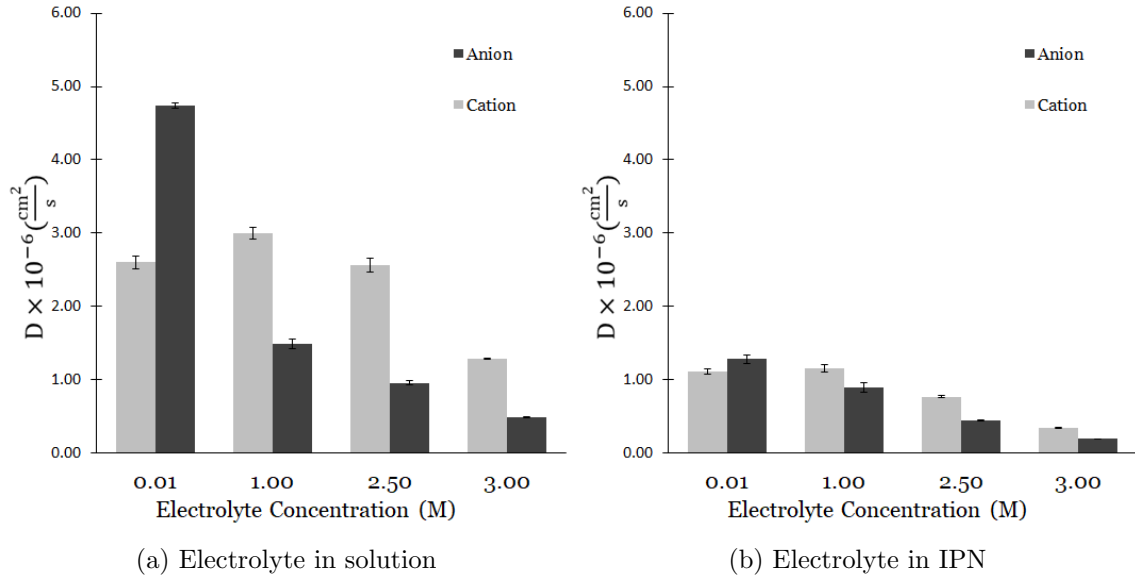


Figure 4.8: Self-diffusion measurements for EMI-TFSI dilutions in PC in solution (a) or embedded in IPN (b).

To discuss the effect dilution has on EMI-TFSI diffusion in PC, we should first return to the Sutherland equation (Eq. 1.4) and the Stokes-Einstein equation (Eq. 1.5) in order to see what the theory predicts. In addition, the solution permittivity and Debye length will, in theory, affect self-diffusion. In general, the theory predicts two opposing effects; one of them suggests an increase and the other a decrease in  $D$  with increased concentration. As mentioned before, these equations are mostly applicable in the low concentration limit, but have shown to be relevant to higher concentrations as well [10].

Both the Sutherland and the Stokes-Einstein equations predict an inverse relation between self-diffusion and electrolyte concentration. The factor most affected by ion concentration is the friction drag factor,  $f$ . Many factors contribute to the change in  $f$ , with the major effect coming from changes in the viscosity of the solution. In a polar solvent, such as PC, an order of magnitude increase in concentration typically increases the viscosity by a factor of approximately 30 [108]. The increased amount of solute ions leads to a more crowded environment which results in more interactions between all types of ions. Molecular crowding is a term mostly used for biological macromolecules, but it has been shown to apply to electrolytes in high concentration solutions, causing decreased solvent activity, resulting in higher molecular interactions [109]. These interactions cause a dramatic increase in viscosity. In addition to the increase in viscosity, higher electrolyte concentration and ion interactions are expected to increase the ionic pairing and other longer lasting ion-ion associations, causing a larger effective size for each moving species, again causing a decrease in self-diffusion with an increase in concentration. The data in Fig. 4.8 clearly shows a decrease in self-diffusion with an increase in concentration, but this decrease is only about a fifth of what the theory predicts.

The effect that might be causing the opposite trend comes from the fact that the solution's permittivity is inversely proportional to its ionic strength. An increase in concentration corresponds to an increase in ionic strength and an increase in screening which decreases the Debye length (Eq. 1.1). This decrease in the Debye length in turn decreases the ion-solvent interactions and the size of the solvation layer around each ion. This can cause the effective ion size to decrease, increasing the self-diffusion with an increase in concentration. Yet, this effect remains small as it is countered by the increase in Bjerrum length (Eq. 1.2), caused by the same increase in ionic strength which increases ion-ion interactions. In general, it is safe to say that as ionic strength increases, the solvation layer

is replaced with ion-ion long range interactions.

This combination of opposing effects leads to the general prediction that self-diffusion is expected to decrease as ion concentration increases. This prediction has been verified, as can be seen for example in the work of Anderson *et al.*, where self-diffusion of neutral large molecules was measured with respect to solutions' ionic strength [12] and in the work of Coglitore *et al.* [110] where self-diffusion of gold nanoparticles and polystyrene was measured with respect to the diffusing particle size. Fig. 4.8 shows that the anion's behaviour generally follows this expectation. The self-diffusion coefficient increases with a decrease in concentration, especially as it reaches 0.01 M, closer to the low concentration limit. The same cannot be said for the cation's self-diffusion as its concentration dependence displays several characteristics which are initially surprising.

An increased radius of a moving species is expected to hinder the self-diffusion coefficient. From the ions' structure (see Fig. 4.4) we can see the anion is larger in size than the cation. According to this, one would expect the self-diffusion of the anion to be consistently smaller than that of the cation. Indeed we see that for high concentrations of RTIL, the cation diffuses faster than the anion. Yet, for low concentrations, it appears that the opposite is observed. Looking at Table 4.1 which shows  $D_+/D_-$ , we can see that for very dilute solutions, the cation diffuses slower than the anion.

Electrolyte concentration (M)	Solution	IPN
0.01	0.56	0.91
1.00	2.01	1.50
2.50	2.67	1.69
3.00	2.64	1.98

Table 4.1: Ratio of self-diffusion coefficients  $\frac{D_+}{D_-}$  for EMI-TFSI in solution and IPN

This surprising behaviour can be explained by the charge distribution of the cation. At

low concentrations, the  $\text{EMI}^+$  cation is heavily solvated due to its substantial electric dipole moment [111] in addition to the dipole moment of the co-solvent. Because PC is an aprotic polar solvent with a relatively high dipole moment of 4.9 D [112], we expect a high affiliation between the solvent and the cation (see structures in Fig. 4.4) [113]. This relatively large solvation layer causes the effective radius and mass of the solvated ion to hinder its self-diffusion. The effect of high solvation results in the unexpected diffusion ratio between the ions. At low concentrations, the diffusion of the smaller cation is slower than that of the larger anion. This is again a result of the solvation layer around the  $\text{EMI}^+$  causing a significantly higher effective size and mass and consequently lower diffusion coefficient than  $\text{TFSI}^-$ , as the anion is relatively free of solvent because the symmetrical charge distribution in its dominant conformation results in a very small dipole moment [114].

With an increase in concentration, we can see another atypical behaviour. The maximal self-diffusion of the cation is not at the lowest concentration. This is again a result of the large solvation layer around it, resulting in a large effective radius. With an increase in concentration, the  $\text{EMI}^+$  sheds much of this solvation as the ionic strength of the solution increases, causing the maximal self-diffusion to be at a relative high concentration of 1 M. This effect can be seen in the IPN as well, but to a much smaller extent as the interaction of the ions with the polymer network reduces the solvation layer around the ions as  $\text{EMI-TFSI}$  is known to have high affinity to polymer networks with polar groups, specifically to PEO where the PEO ethers coordinate both the  $\text{EMI}^+$  and  $\text{TFSI}^-$  ions [115]. These high affinity interactions replace the ions' solvation layer with fixed groups on the polymer, resulting in an absorption of the RTIL in the PEO polymer network and a reduction in the solvation layer size.

At still higher concentration, both diffusion coefficients decrease as the solution viscosity increases and ion interactions slow ion motion. The  $\text{TFSI}^-$  diffusion coefficient decreases

slightly faster than that of the  $\text{EMI}^+$  as the RTIL concentration increases, as has been observed in some other RTILs [57].

Another point of comparison between the self-diffusion data and the device behaviour is the concentration at which an inversion between anionic and cationic behaviour is observed. Table 4.1, which shows the ratio of self-diffusion coefficients for the ions, shows this inversion between 0.01 M and 1 M. This inversion in  $D$  is expected to be seen in the device behaviour—both in actuation behaviour and in open circuit voltage measurements, as they both rely on differences in diffusion rates of the different ions. Yet, the concentration at which we see the actuation inversion does not match that seen in self-diffusion measurements. The inversion in device behaviour occurs at a higher concentration as can be seen in Fig. 4.2, around 2.5 M. This disagreement is an indication that there is a difference between the charge carrying abilities of the ions to their general self-diffusion, i.e., it suggests that there are some species that diffuse, but do not carry charge. A direct comparison between device behaviour and self-diffusion is not possible and direct measurements of mobility are necessary. From this difference in inversions, we expect that correlated ion motion exists in the system and affects its conductivity. To further investigate this assumption, conductivities were estimated from our self-diffusion measurements.

Using Eq. 1.16 the estimated ionic conductivity can be derived from self-diffusion measurements. These results are presented in Fig. 4.9. As has been discussed in Section 1.1.4, the derived conductivities from PFG-NMR measurements do not include the important factor of  $z_{\text{eff}}$  and are therefore used in a qualitative manner, in comparison to directly measured conductivities.

The estimated conductivity trend in Fig. 4.9 seems to agree with the directly measured ionic conductivity (Fig. 4.3). A maximum of both measured and estimated conductivities is observed around 2.5 M. The fact that the maximal conductivity is not at maximal or

### 4.3. Results and Discussion

minimal dilutions is common for RTIL dilutions in solvent. This is a result of the balance between two opposing factors; as the charge carrier concentration increases the conductivity increases, however the increased concentration reduces their diffusivity.

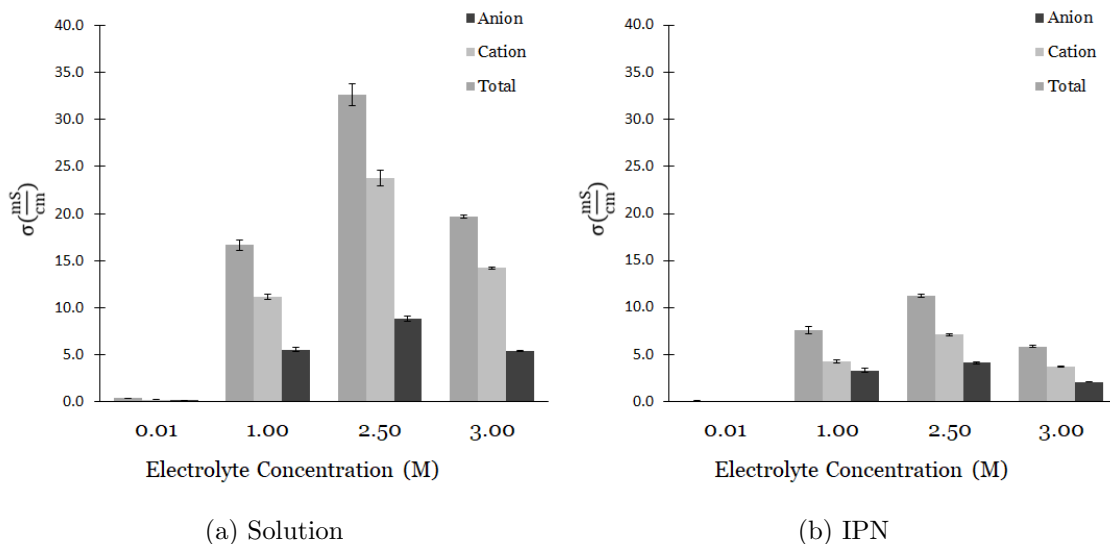


Figure 4.9: Estimated conductivity derived from self-diffusion measurements. Notice the conductivity for 0.01 M is lower by two orders of magnitude from the highest ionic conductivity measured at 2.50 M

As suggested by Tokuda *et al.*, the ionicity (or level of ionic association) can be calculated for a total electrolyte by using the directly measured total ionic conductivity and the estimated total conductivity derived using PFG-NMR, self-diffusion measurements, and the Nernst-Einstein relation (Eq. 1.15). This ratio of  $\frac{\sigma_{\text{NMR}}}{\sigma_{\text{direct}}}$  is presented in Fig. 4.10 and shows an interesting trend.

For solution samples at low concentrations, this ratio starts from a number slightly higher than one, indicating that the estimated conductivity is slightly higher than the measured conductivity. This observation indicates very few to no neutral aggregates and might even indicate an additional conduction mechanism that does not rely solely on charge

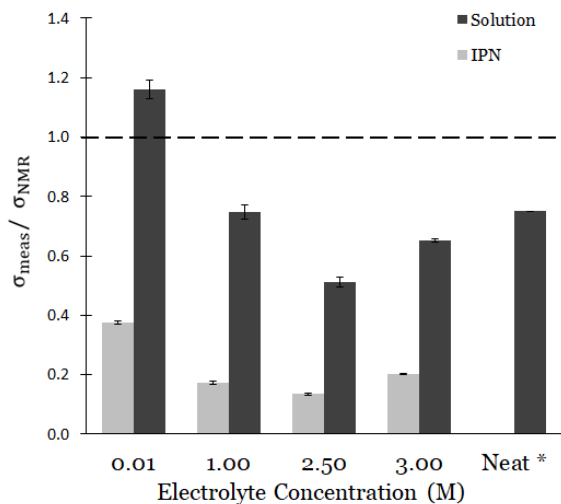


Figure 4.10: Ratio of directly measured conductivity  $\sigma_{\text{mes}}$  to the estimated  $\sigma_{\text{NMR}}$ .  $\sigma_{\text{NMR}}$  is estimated from NMR diffusion measurements using the Nernst-Einstein relation. This ratio is an estimation of the “ionicity” of an ionic liquid, and shows a minimum at 2.50 M, the point of maximal total conductivity. Values are shown for both solution and IPN embedded electrolyte. Value of neat RTIL (self concentration of 3.90 M) is added for comparison.

transport via the motion of the ions. This observation does not exist for IPN embedded samples, as even at low concentration, the local concentration in the IPNs is high enough to not allow for the ions to be distant enough to avoid the formation of neutral ion aggregates.

For both solution and IPN embedded samples, a trend as the concentration of RTIL increases can be identified. The ionicity of the solution decreases, indicating the formation of neutral associations. This is expected from an increase in the molecular crowding found in the solution and an increasing number of collisions between counterions. This phenomenon is common for many electrolyte solutions and has been observed before for both RTILs and simpler electrolyte solutions [28, 116, 117]. Interestingly, an inversion in the trend can be seen for high concentrations of RTIL. The ionicity increases as the concentration reaches  $\sim 75\%$  of the neat ionic liquid, at 2.5 M. A similar behaviour was seen by Hou *et al.* for the same cation but different anion at lower concentrations using water as a solvent [57].

### 4.3. Results and Discussion

---

This inversion indicates that in high enough concentration, the ions tend to decrease in ion-ion associations or shift to odd-numbered aggregates, either of which would result in increased conductivity. This means that the addition of a solvent to RTIL initially first promotes ionic association and after further dilution, promotes dissociation. The crossover between these two behaviours is seen at the same concentration as the maximum of ionic conductivity, again confirming the effect of ion-ion associations.

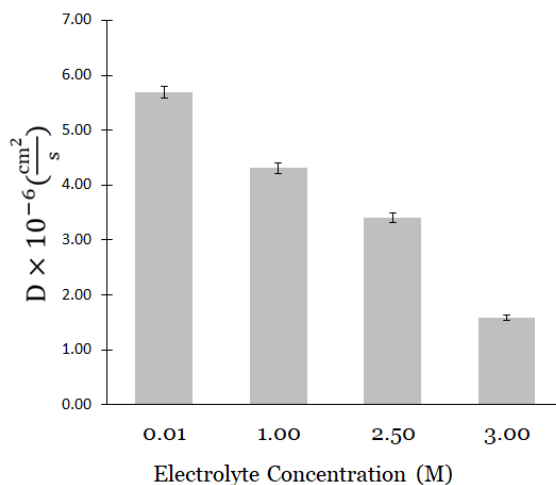


Figure 4.11: Co-solvent PC diffusion measurements in a solution sample vs. RTIL concentration.

The measured diffusion of the co-solvent is presented in Fig. 4.11. In agreement with predictions for solvent self-diffusion [118],  $D$  decreases with increased ionic strength. Because there is no inversion in the diffusion trend for the solvent, we can conclude that the inversions we see in the diffusion of the ion is a result of ion-ion associations and not general effects which arise due to the viscosity.

Because the solvation of the anion and the cation in PC is not the same, the effect it has on each of the ions might not be identical. Both PC and  $\text{TFSI}^-$  are electron donor molecules in comparison to  $\text{EMI}^+$  which is an electron acceptor. Also, if we look at the

shape of PC (Fig. 4.4) we notice its negative charge distribution is concentrated on the oxygen on its less bulky side. This might indicate an easier association to its negative side and therefore a heavier solvation layer on the cation. The charge and its location indicate that the cation is more easily solvated with PC than the anion. This could explain why TFSI<sup>-</sup> tends to aggregate more causing a reduced anion diffusion at higher concentration.

Another possible interaction that affects the diffusion arises from the interactions of the ions with the polymer network which were mentioned before. The high affinity between PEO and the RTIL indeed decreases the solvation layer around the ions, but might also decrease the ionic mobility of the solution by hindering the motion of the ions. To distinguish these interactions from one another, further research is needed using different co-solvents and different polymer compositions.

## 4.4 Conclusions

Self-diffusion measurements of EMI-TFSI dilutions in PC have been measured for both RTIL ions in solutions and IPNs. These measurements help to shed some light on the mechanisms behind the behaviour of actuators and sensors made of these materials.

In both solution and swollen IPNs, the change from cationic to anionic behaviour that was seen previously in actuator devices can also be seen in the self-diffusion data. An inversion in diffusion ratios between the ions depends on the RTIL concentration. From this inversion, we confirm that the observed change in the devices' actuation behaviour is a result of changes in their transport properties. This change in transport properties with respect to dilution shows that the extent and amount of ion-ion and ion-solvent associations depend on the sample concentration and helps confirm the suggested piezoionic mechanism. In addition, self-diffusion measurements show an expected disagreement between directly measured conductivity and self-diffusion estimated conductivity. This disagree-

ment again suggests the existence of ion-ion and ion-solvent interactions and enables us to assess the “ionicity” of each sample. The level of ionicity is an important factor in the understanding of the conduction mechanism of these ion dense solutions and ion dense IPNs. The ionicity level measured is minimal at the concentration of maximal conductivity measured in devices. This agreement helps to confirm the proposed Dupont mechanism, which suggests an increased fraction of ion associated species compared to neat RTIL.

From the measurements of self-diffusion and conductivity, we conclude that ion-ion associations exist in both solution and IPN devices, and they affect the conductivity of ionic conductors greatly. The dilution of RTIL can change the abundance and composition of these associated species and thus affect both the sign and magnitude of device conductivity and actuation response.

## Chapter 5

# Ion Transport in Touch Sensor Electrolytes

### 5.1 Introduction

As has been discussed in the previous chapter's introduction (Section 4.1), iontronics is a growing field of interest, in part because of the potential for iontronic devices to operate both as actuators and as sensors. In comparison to conventional electronics, iontronics have the ability to interface with biological tissues as they do not provoke an immune response from the body [119]. These properties make iontronics ideal candidates for artificial muscles and nerves.

Potential devices rely on the mechano-electrical transduction properties of ion dense conductors that have been shown in a number of ion-polymer systems such as hydrogels, polyelectrolytes, and ionic polymer materials [120, 121]. This ability to act as sensors and actuators comes from the 'piezoionic effect' [100, 101, 99, 102] which was introduced in Chapter 4. The piezoionic effect is defined in a similar way to the piezo-electric effect. When undergoing physical deformation, a measurable voltage is produced in the device. The suggested mechanism to this phenomenon involves pressure induced ionic redistribution of the electrolyte and depends on diffusion and conduction mechanisms of the ions in the system.

While it has been widely observed that diffusion and conduction mechanisms in ion-dense electrolytes differ from those of ideal solutions [58], detailed understanding of the phenomenon suffers from the small number of experimental techniques that allow accurate characterization. In solutions with concentrations higher than approximately half a molar, a shift from typical ionic conduction mechanisms occurs. Due to crowding effects, oppositely charged ions tend to stick to each other, forming ion clusters which have both higher mass and volume than a free ion and as a result decrease their self-diffusion coefficients. In addition, these clusters have a different total charge termed “effective charge” ( $z_{\text{eff}}$ ). All of these affect the response of the ion cluster to an applied electric field. The clustering might result in charge neutral clusters of ions which do not respond to an external applied electric field and cause the ions to lose their charge carrying abilities. Due to these differences in solvation and the formation of ion-associated structures, the electrophoretic mobility ( $\mu$ ) and self-diffusion depart from the linear ratio predicted by the Nernst-Einstein relation (see Eq. 1.15 and Section 1.1.3 for further information).

Although the mechanism behind the piezoionic phenomenon is not yet clear, both the magnitude and direction of this effect can be tuned using variations of ions, solvents, and concentration. In this chapter we discuss the use of NMR as a method to investigate the mechanism behind the piezoionic effect. Transport properties have been measured using both PFG-NMR and eNMR in a range of materials. We have measured both self-diffusion ( $D$ ) and electrophoretic mobility ( $\mu$ ) of ions in salt solutions of varying concentration in an attempt to investigate the difference between self and driven diffusion and to learn about the interesting conduction mechanism of  $\text{Li}^+$  in these fascinating new materials.

## 5.2 Methods

### 5.2.1 Sample Preparation

Electrolyte solutions of varying concentration between 0.01 M to 3.00 M were made by dissolving bis(trifluoromethane)-sulfonimide lithium (LiTFSI) salt with PC as solvent. The molecular structure of the ions is shown in Figs. 5.1 and 5.2, respectively. The mixtures were then sonicated for approximately 10 minutes until completely dissolved.

Polymer gels based on Poly(vinylidene fluoride-co-hexafluoropropylene) (PVDF-HFP) co-polymer (Fig. 5.3) were synthesized with LiTFSI salt using a solution casting technique. A polymer stock solution was made by dissolving PVDF-HFP pellets in acetone at 7.5 % wt. Electrolyte solutions of varying concentration were then mixed with the host polymer solution at a ratio of 5 mL/33.3 g (electrolyte/polymer stock). To ensure complete mixing, the mixture was sealed and sonicated for 2 hours with occasional stirring. The mixture was poured into a mould and covered with a perforated lid to allow gradual evaporation of the acetone at room temperature. The final polymer content was 30 wt% and the thickness of the films was approximately 200  $\mu\text{m}$ .

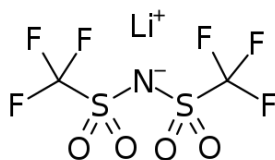


Figure 5.1: Structures of  $\text{Li}^+$  and bis(trifluoromethane)-sulfonimide ( $\text{TFSI}^-$ ) ions

### 5.2.2 Viscosity Measurements

Viscosity measurements were done at room temperature (22  $^{\circ}\text{C}$ ) using an Anton Paar MCR 301 rheometer applied with a rotational probe head.

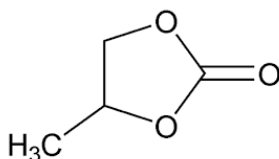


Figure 5.2: Structure of Propylene Carbonate (PC)

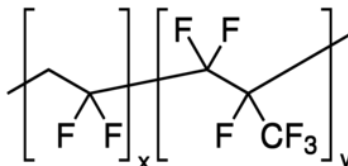


Figure 5.3: Poly(vinylidene fluoride-co-hexafluoropropylene) (PVDF-HFP) co-polymer

### 5.2.3 Self-Diffusion Measurements

Self-diffusion measurements were performed at 22 °C using a home-built PFG probe [2] in a home-built NMR spectrometer [89] operating at 8.4 T (both are described in Chapter 3). To track the individual ions,  $^{19}\text{F}$ -NMR was used for TFSI $^-$  and  $^7\text{Li}$ -NMR for Li $^+$ . PFG-STE NMR pulse sequence was used (described in Section 3.2 and Fig. 2.2) with diffusion echo time,  $\tau$ , of 0.5 ms to minimize the loss of signal due to spin-spin relaxation. A gradient pulse of  $\delta=318\ \mu\text{s}$  was applied in varying strength from about  $g = 50\ \frac{\text{G}}{\text{cm}}$  to  $1000\ \frac{\text{G}}{\text{cm}}$  for solution samples, and about  $g = 100\ \frac{\text{G}}{\text{cm}}$  to  $2000\ \frac{\text{G}}{\text{cm}}$  for samples embedded in polymer films. The diffusion time  $\Delta$  was varied between 350 – 900 ms, depending on the sample's diffusion rate. An acquisition delay of  $T=10\ \text{ms}$  was used in order to allow eddy currents to decay before acquisition.

### 5.2.4 eNMR Measurements

eNMR mobility measurements of electrolyte samples were done at 22 °C using the home-built eNMR probe (described in detail in Section 3.5). A spin-echo eNMR pulse sequence

(Fig. 2.3) was used with varying echo times of between 25-300 ms. The diffusion time,  $\Delta$ , was set between 50 to 600 ms and the pulse gradient duration  $\delta$  was varied between 1-10 ms. In order to ensure measurement of flow in the steady state, the electric field was initiated 200 ms before the pulse sequence started and was cut off after the signal acquisition was done. The voltage was applied to the sample through a constant current regulator to achieve a current of 1.5 mA. Tracking the voltage applied to the sample using an oscilloscope ensured that the current did not reach saturation and remained consistent throughout the eNMR experiment time. The gradient strength,  $g$ , was kept relatively low at a maximum of  $34 \frac{\text{G}}{\text{cm}}$  in order to balance the loss of signal due to self-diffusion, and maximize the phase shift due to the electrophoretic mobility of the ions. The time between the scans was set to 10 s in order to allow the sample to return fully to equilibrium and in order to avoid heat accumulation due to current flow in the sample.

To measure the electric field applied during the eNMR experiment, four point voltage measurements were done outside the magnet. The measurements were done by applying the same current as was used in the eNMR experiments, using the pulse programmer to maintain accurate duration as well. The AgCl electrodes used to measure the voltage were placed at known distances from each other via two holes drilled through the sample holder sides. This combination of known distance and measured voltage allowed us to calculate the electric field with an uncertainty of less than 5%.

In addition, attempts to measure the electrophoretic mobility in polymer electrolytes were done using the same set-up. Some of the electrolyte solution was removed from the polymer samples by wiping gently with a Kimwipe, to encourage slight shrinkage. The samples were then cut and placed in the 5 mm NMR tube and re-soaked with the electrolyte solution while in the tube. As the samples swelled again, contact of the polymer with the glass was maximized. The electrodes were kept in contact with the electrolyte solution to

conduct the current through the gel sample. The gel sample itself was longer than twice the NMR coil length to ensure any motion detected was a result of ionic motion inside the gel sample and not the electrolyte solution.

### 5.2.5 Conductivity and Piezoionic Measurements

Ionic conductivities of the polymer gels were determined by electrochemical impedance spectroscopy. Each sample was cut to a 2.5 cm by 1 cm rectangle and clamped between two stainless steel plates. Measurements were performed by sweeping a sinusoidal excitation voltage from 1 MHz to 0.1 Hz. The resistance of each sample was recorded at high frequency where the metal/polymer interface capacitance effectively shorted the interface impedance.

For electrolyte solution samples, the bulk ionic conductivity was measured using a computer-controlled Hewlett Packard 4192A LF impedance analyzer by applying 10 mV AC at 10 kHz. The measurements of the samples were carried out in a commercially available conductivity cell with platinized platinum (black) electrode cells (TOA Electronics, CG-511B).

Measurements of the piezoionic response were performed by subjecting the polymers to a mechanical deformation and recording both open circuit voltage and current response as a function of amplitude and frequency of the mechanical perturbation. The deformation was applied using a Bose ElectroForce<sup>®</sup> 3000 series dynamic mechanical analyzer and the voltage response was measured using a Metrohm Autotlab<sup>®</sup> PGSTAT101 potentiostat/galvanostat. The perturbation was load controlled with a maximum displacement of 2 mm. As pure PVDF-HFP can also show a piezoelectric response, similar tests were performed on PVDF-HFP films with no electrolyte concentration to confirm that the piezoelectric response was not a result of the polymer itself. The overall setup is presented in detail in Dobashi's MASc thesis [122].

### 5.3 Results and Discussion

To initially characterize their piezoelectric behaviour, the voltage response of PVDF-HFP co-polymer samples with varying concentrations of LiTFSI were measured in sensor mode. The general set-up and the results are presented in Figure 5.4. A general decrease of produced voltage can be seen with respect to increased concentration of salt. An inversion point can be seen around 2M. This change of both magnitude and direction of voltage indicates a significant change in conduction and diffusion properties. This motivates further investigation with direct measurements of both self and driven diffusion for each individual ion in these systems. Measurements were made for both electrolyte swollen polymer films and for the electrolytes alone.

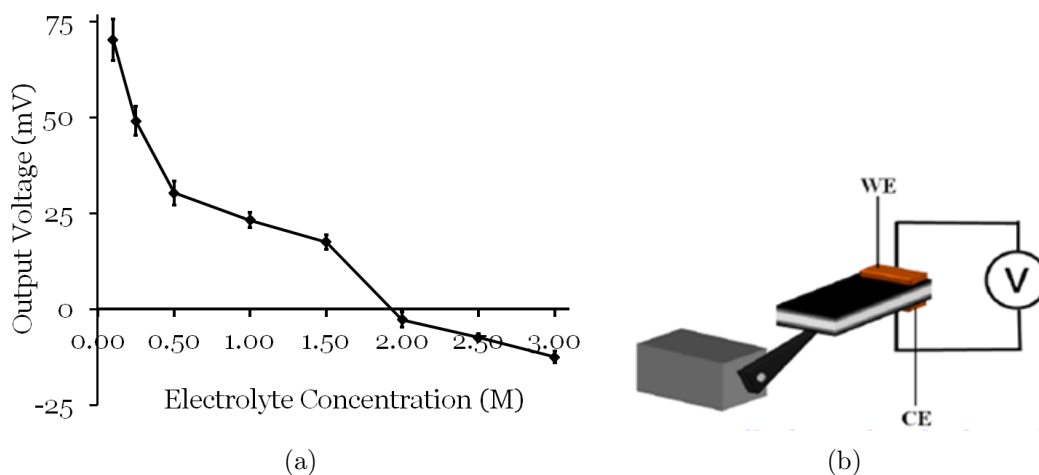


Figure 5.4: Electromechanical voltage response to controlled deformation of PVDF-HFP co-polymer prepared with varying LiTFSI salt concentration solutions. An inversion of output voltage is seen between 1.50 and 2.00 M which implies an inversion in the dominant charge carrier species. (b) a general diagram of the measurement set-up.

### 5.3.1 Self-Diffusion in Electrolyte Samples

Examples of self-diffusion measurements for both TFSI<sup>-</sup> and Li<sup>+</sup> ions dissolved in PC are presented in Figs. 5.5 and 5.6, respectively. The Gaussian decay of the signal intensity vs. gradient strength, as well as the linearized version of the same data, show excellent fits to single Gaussians, indicating the presence of a single diffusion coefficient.

A summary of self-diffusion measurements for both ions in electrolyte solutions is presented in Fig. 5.7. The results show an expected decreasing trend of self-diffusion as the salt concentration increases. Viscosity measurements for the same set of samples can be seen in Fig. 5.8a and show a dramatic increase in viscosity with increasing salt concentration which is consistent with calculations [123] and measurements seen in similar RTILs in water [108]. The expected increase in both crowding effects and viscosity causes a decrease of more than an order of magnitude in self-diffusion from highly diluted to concentrated solutions. When the concentration of ions in solution is high, the distance between the ions is reduced. When the distance between them is lower than the Debye length ( $\kappa^{-1}$ ), electrostatic interactions take place. Depending on the sign of the species' charge, electrostatic forces either repel or attract the neighbouring ions. The ions that are attracted result in clustered species of two or more ions. These clusters have a larger radius than individual ions and diffuse slower, as expected from the Stokes-Einstein equation (Eq. 1.5).

Unlike previous observations of concentrated LiBF<sub>4</sub> in sulfolane which showed increased self-diffusion of Li<sup>+</sup> in comparison to BF<sub>4</sub><sup>-</sup> [124], the cation's self-diffusion remains consistently lower than that of the anion for all concentrations. This initially might seem surprising due to the fact that the cation itself is significantly smaller than the anion (see Fig. 5.1). Yet, this can be explained by the larger and bulkier solvation layer surrounding the cation, resulting in a large effective total radius of the moving species. Previous calculations by Shi *et al.* [125] have shown that for concentrations lower than 2 M, the solvation layer formed

by PC solvent molecules around a  $\text{Li}^+$  ion consists of 4 solvent molecules, resulting in a tetrahedral solvation structure and effective size of more than  $10 \text{ \AA} \times 10 \text{ \AA} \times 10 \text{ \AA}$ . In comparison, due to its symmetrical shape, single hydrogen bonding site (the nitrogen [126]), and well distributed negative charge the  $\text{TFSI}^-$  anion has lower interactions with the solvent molecules [114, 127]. As shown by density functional theory (DFT) calculations and Raman spectroscopy measurements, two conformers are common for the  $\text{TFSI}^-$  anion. The staggered conformer is slightly more stable than the eclipsed, and rotation between the two is expected at room temperature ( $\Delta E = 2.3 - 2.9 \frac{\text{kJ}}{\text{mol}}$ ) [114]. This rotational motion, along with the fact that both conformers have a relatively delocalized charge, are the reason the anion struggles to make long-lasting interactions with solvent molecules, resulting in an anion that is almost bare of solvent. This leaves the anion with an estimated effective size of approximately  $8 \text{ \AA} \times 4 \text{ \AA} \times 2 \text{ \AA}$  [128, 129, 130] which is smaller than the effective size of  $\text{Li}^+(\text{PC})_4$  [125, 131]. This difference in solvent-ion interactions between the two ions helps explain the difference in self-diffusion for the ions and rationalize the fact that the cation self-diffusion is consistently smaller than that of the anion.

Another observation from the self-diffusion data in Fig. 5.7 is the general decreasing trend in self-diffusion as the salt concentration increases. The self-diffusion coefficients for both ions decrease and become similar. At 2.00 M, self-diffusion coefficients for both ions are nearly identical and at 2.50 and 3.00 M the difference is eliminated. As the salt concentration increases, the ratio of solute to solvent molecules decreases, making it impossible for the cation to be solvated by 4 solvent molecules. As the concentration reaches 2.1 M the molar ratio of  $\text{LiTFSI}:\text{PC}$  is 1:4 and decreases further as the concentration increases. Shi *et al.* shows that for higher than 2 M, the dominant species is a planar  $\text{Li}^+(\text{PC})_3$  and the effective radius of such species is at least 3 times smaller than the tetrahedral  $\text{Li}^+(\text{PC})_4$  ( $3 \text{ \AA} \times 10 \text{ \AA} \times 10 \text{ \AA}$  [125]). In addition, this decrease in solvation layer makes ion-ion

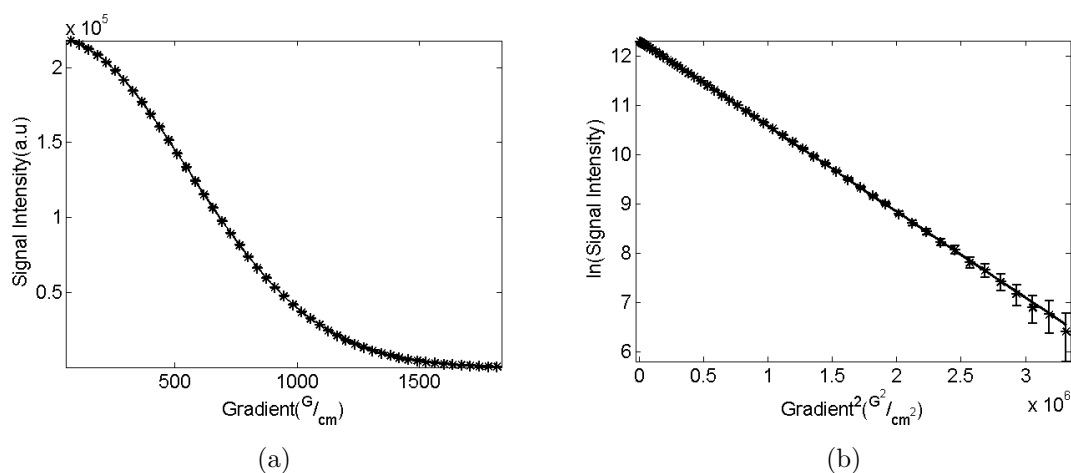


Figure 5.5: Example of a diffusion experiment of  $\text{TFSI}^-$  in 2 M LiTFSI/PC with a diffusion time  $\Delta = 350$  ms, performed at  $22^\circ\text{C}$ . (a) shows  $\text{TFSI}^-$  fluorine peak integral vs. magnetic field gradient strength. The data is fitted to a Gaussian decay function. (b) shows the same data, plotted as the natural logarithm of the signal intensity vs. gradient strength squared to linearize the Gaussian. Both figures show excellent fits to a single diffusion coefficient of  $D = (1.91 \pm 0.07) \times 10^{-11} [\frac{\text{m}^2}{\text{s}}]$

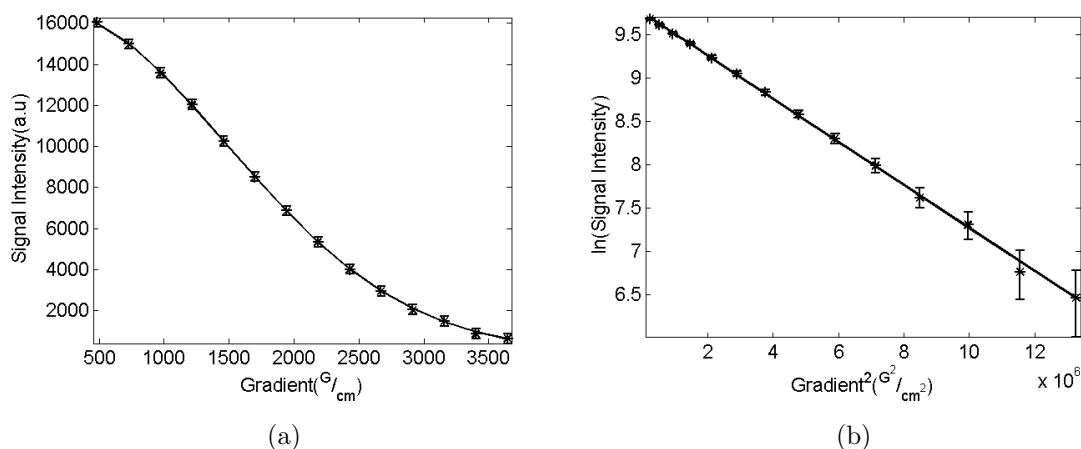


Figure 5.6: Example of a diffusion experiment for  $\text{Li}^+$  in 2 M LiTFSI/PC with a diffusion time  $\Delta = 350$  ms, performed at  $22^\circ\text{C}$ . (a) shows the  $\text{Li}^+$  peak integral vs. gradient strength. The data is fitted to a Gaussian decay function. (b) shows the same data, plotted as the natural logarithm of the signal intensity vs. gradient strength squared to linearize the Gaussian. Both figures show excellent fits to a single diffusion coefficient of  $D = (1.59 \pm 0.09) \times 10^{-11} [\frac{\text{m}^2}{\text{s}}]$

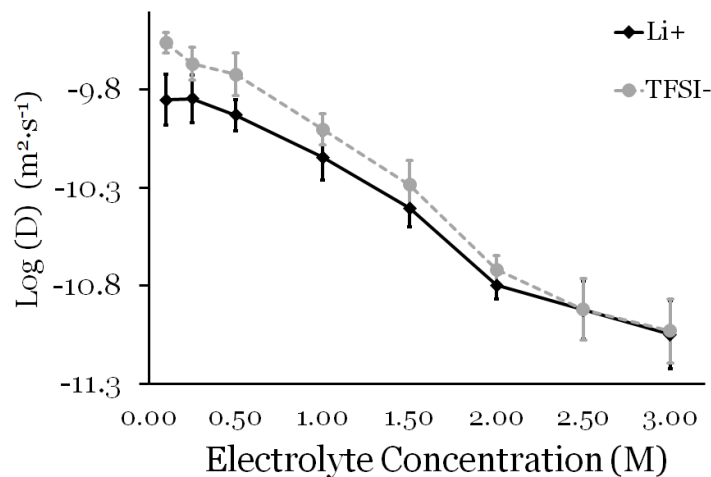


Figure 5.7: Self-diffusion measurements of LiTFSI vs. electrolyte concentration as measured by PFG-NMR. Solid line shows  $D$  for the cation and dashed line for anion. The lines are meant only to guide the eye.

interactions more probable and the ions spend more time as contact ion pairs and solvent separated ion pairs. This ion pair formation has been suggested by Wang *et al.* [126] who have done Raman spectroscopy experiments on the same system in varying concentrations. They interpreted their measurements as a potential formation of ion pairs in concentrations higher than 2.5 M which can be validated by the data presented here.

In order to separate the effects of ion-ion and ion-solvent interactions from the general viscosity of the solution, the total dynamic viscosity of the solution,  $\eta$ , was measured. Results are presented, on a logarithmic scale, in Fig. 5.8a. As previously mentioned, the viscosity increases as the salt concentration of the solution increases, indicating again the increased crowding effects and more ion-ion interactions. By combining self-diffusion with viscosity measurements, we can use the Stokes-Einstein equation (Eq. 1.5) to extract an approximate effective radius ( $r$ ) for each of the ions. The values for  $r$  are presented in Fig. 5.8b. These calculations should be considered an approximation due to the underlying assumptions involved in the Stokes-Einstein equation. The equation accounts for drag force

### 5.3. Results and Discussion

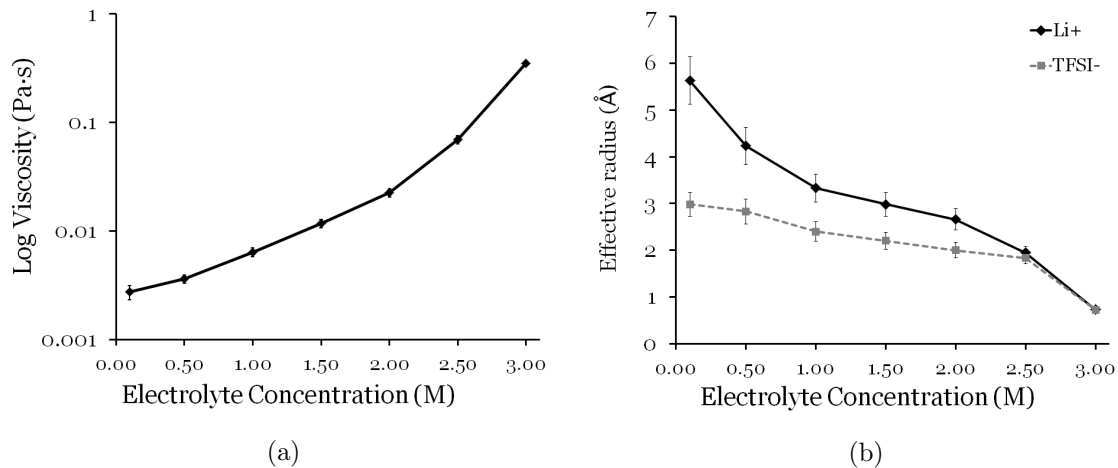


Figure 5.8: (a) Dynamic viscosity of the solution vs. salt concentration in PC measured using a rotational rheometer (MCR 301) (b) Estimated effective radius ( $r$ ). The lines are meant only to guide the eye.

applied on rigid, spherical molecules with small Reynolds numbers. These assumptions do not apply accurately to this specific set of salt and solvent conditions and therefore the numerical values should be considered an estimation. Furthermore, the factor  $b$  in this equation, which accounts for the level of interactions between the moving species and their environment, potentially changes with changes in concentration. Therefore, it is again important to interpret these numerical values with caution.

Observing the graph in Fig. 5.8b, we can see that the effective radius ( $r$ ) of the cation has a strong initial decrease as concentration increases. This dramatic decrease in  $r$  is a result of the increase in  $\eta$  as well as changes to the  $b$  factor due to initial changes from tetrahedrally solvated ions to trigonal. This decrease is followed by a more gradual decrease which becomes significant again around 2.00 M, by which point we expect the majority of the cations have had their solvation layer change from tetrahedral to planar. Looking at the change in the anion's effective radius we see a slow, gradual decrease in  $r$  from a dilute solution to about 2.50 M where there is a more drastic decrease in  $r$  and the effective radius

becomes identical to that of the cation. Around this concentration, we expect to have a more significant amount of ion-ion associations. From our measurements, we see that these associated species decrease the measured diffusion coefficient significantly ( $\sim$ order of magnitude), but do not increase the effective size to the same extent. This comes as a surprise because we can see the effect of ion-ion species in  $D$ , but not as much in  $r$ . Because of the method used to calculate  $r$  using  $\eta$ , we do not account for the gradual change in the  $b$  factor due to the ion clustering.

To compare the self-diffusion data to the experimental sensor data, we needed a comparable quantity. Conductivity was chosen as the most direct solution yet, to be able to calculate conductivity from  $D$ , the traditional (and most likely wrong) assumption that the effective charge,  $z_{\text{eff}}$ , is equal to the ions' valence had to be used (Eq. 1.16). Both derived and directly measured conductivities are summarized in Fig. 5.9 to allow for an easy comparison.

For low concentrations, the derived conductivity from self-diffusion shows an excellent match to the directly measured conductivity. This means the assumption of  $z_{\text{eff}}$  equal to valence charge is valid and the existence of ion-ion associated structures is minimal and insignificant. In highly diluted solutions, the distance between the ions is large enough (larger than the Bjerrum length) therefore the interactions between oppositely charged ions are minimal and conductivity can be safely derived from self-diffusion measurements. Once the salt concentration exceeds 0.25 M, derived conductivities from self-diffusion consistently over estimate the ions' ability to carry charge. Because self-diffusion measurement is not able to distinguish between neutral and charged species, it falsely assumes that neutral species conduct charge. It is therefore expected that self-diffusion measurements will fail to account for the effect ion pairs, and other charge altering associations, have on conductivity.

In an alternative approach, ion transport numbers were used to observe the charge

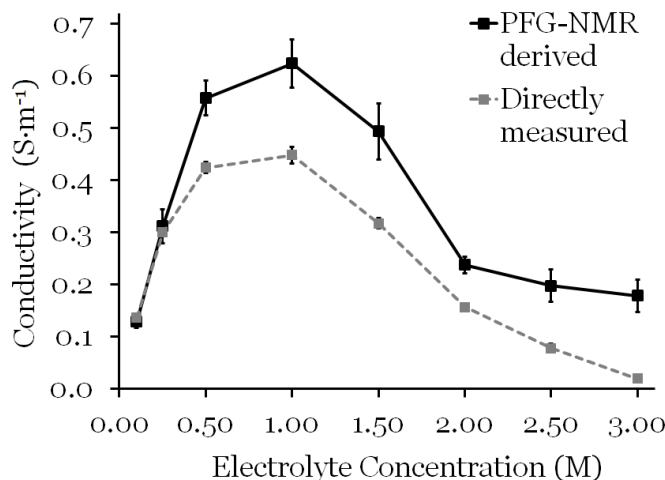


Figure 5.9: Total conductivity derived from PFG-NMR self-diffusion measurements vs. directly measured conductivity for LiTFSI vs. salt concentration in PC. The lines are meant only to guide the eye.

carrying ratio between the ions. Derived from the ratio of ion conductivity to the total conductivity, both derived from self-diffusion measurements, the transport numbers are presented in Fig. 5.10. Unlike the inversion seen between 1.5 and 2 M in sensor mode measurements (Fig. 5.4), we see no inversion of transport numbers from self-diffusion measurements in solution. This means that, according to the self-diffusion data, the anion remains the main charge carrier for all concentrations, contradicting the data shown by deformation measurements. In addition to the known issue of  $z_{\text{eff}}$ , this disagreement potentially arises because we compare the self-diffusion of electrolyte solutions to deformation measurements done on IEAP devices. To improve our comparison and look further into this inconsistency, we have measured the self-diffusion of samples identical to the IEAP devices and those are discussed in the next section.

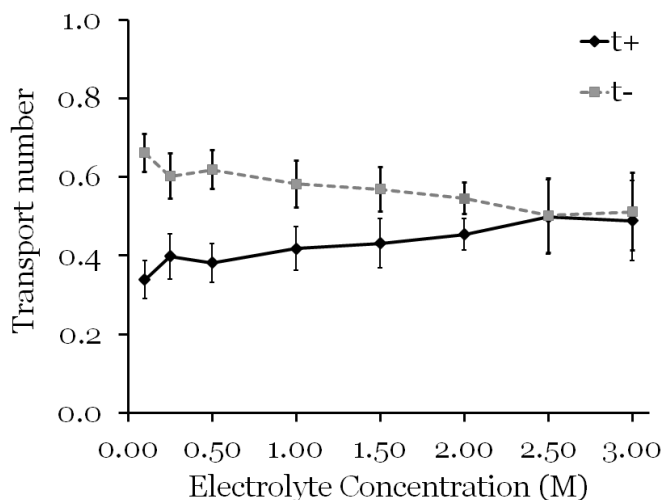


Figure 5.10: Transport number derived from self-diffusion measurements of LiTFSI vs. salt concentration in PC. Solid line for the cation and dashed line for anion. The lines are meant only to guide the eye.

### 5.3.2 Self-Diffusion in Polymer Electrolyte Samples

Examples of self-diffusion measurements for the PVDF-HFP co-polymer samples are presented in Figs. 5.11 and 5.12 for TFSI<sup>-</sup> and Li<sup>+</sup>, respectively. The Gaussian decay of the signal intensity vs. gradient strength and the linearized version of the same data show an excellent fit to single Gaussians, indicating the presence of single diffusion coefficients. A summary of the self-diffusion measurements for the IEAP samples is presented in Fig. 5.13a. These measurements are in better agreement with the deformation data as they show a similar pattern of inversion as was seen for the sensor deformation experiment in Fig. 5.4. The sensor showed an inversion of output voltage in concentrations between 1.5 and 2.0 M, and self-diffusion measurements of the IEAP samples show an inversion at  $\sim 1$  M. This might indicate that ion-polymer interactions indeed have a role in changing the charge carrying abilities of the ions, but they are not identical since we are still only looking at

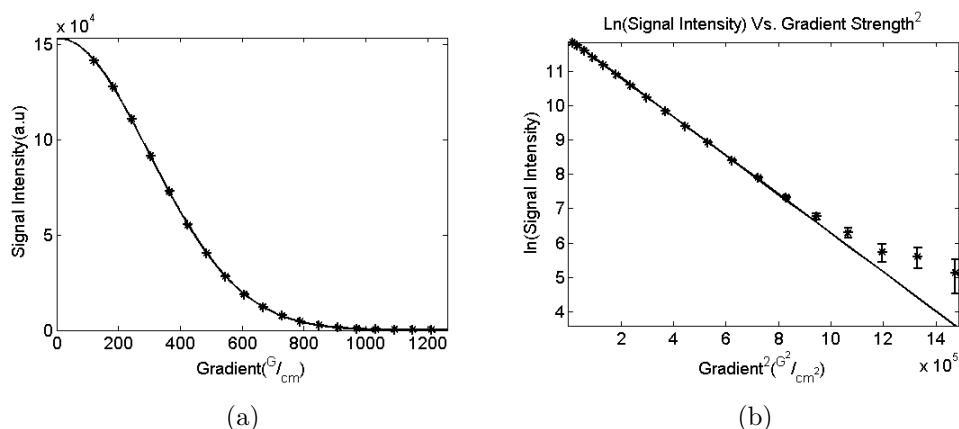


Figure 5.11: Example of a diffusion experiment for the anion, ( $\text{TFSI}^-$ ) of 2M LiTFSI/PC in PVDF-HFP co-polymer with a diffusion time  $\Delta = 350$  ms, performed at  $22^\circ\text{C}$ . (a) shows the single  $\text{TFSI}^-$  fluorine peak vs. gradient strength. The data is fitted to show a Gaussian decay of the signal with an increase in gradient strength. (b) shows the same data, plotted as the natural logarithm of the signal intensity vs the gradient strength squared to linearize the Gaussian behaviour of the Stejskal-Tanner diffusion equation. Both figures show excellent fits to a single diffusion coefficient of  $D = (6.35 \pm 0.09) \times 10^{-11} [\frac{\text{m}^2}{\text{s}}]$

self-diffusion, a property that does not take into account  $z_{\text{eff}}$  of the ions.

The self-diffusion of the anion in IEAPs shows a similar trend to that observed in the electrolyte solutions (repeated as Fig. 5.13b).  $\text{TFSI}^-$ 's self-diffusion coefficient consistently decreases with an increase in concentration. Unlike the anion,  $\text{Li}^+$  shows a different trend. The self-diffusion coefficient of the cation stays relatively constant with an increase in concentration. This is potentially the result of a similar solvation effect to that which is seen in the electrolyte. However, when embedded in a polymer, solvation and effective radius of the cation have a more significant effect over the diffusion as the ion tries to move through the polymer network. As the concentration increases, the cation's solvation and effective radius are reduced, making it easier for  $\text{Li}^+$  to move through the polymer. Due to the small effect solvation has on the anion, it is not as heavily affected by interactions with the polymer and the general trend of decreasing self-diffusion with increased salt

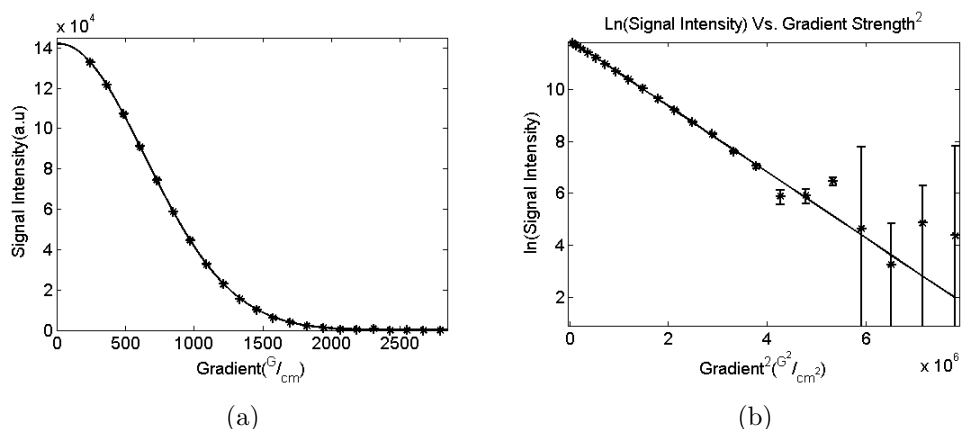


Figure 5.12: Example of a diffusion experiment for the anion, ( $\text{Li}^+$ ) of 2M LiTFSI/PC in PVDF-HFP co-polymer with a diffusion time  $\Delta = 350$  ms, performed at  $22^\circ\text{C}$ . (a) shows the single  $\text{Li}^+$  fluorine peak vs. gradient strength. The data is fitted to show a Gaussian decay of the signal with an increase in gradient strength. (b) shows the same data, plotted as the natural logarithm of the signal intensity vs the gradient strength squared to linearize the Gaussian behaviour of the Stejskal-Tanner diffusion equation. Both figures show excellent fits to a single diffusion coefficient of  $D = (8.2 \pm 0.1) \times 10^{-11} [\frac{\text{m}^2}{\text{s}}]$ .

concentration remains.

The change in environment between IEAPs and solution results in the following surprising observation: For high concentrations (above 1.5 M), the self-diffusion of both ions is higher than in solution. This is counterintuitive as we expect a viscous, harder to pass through medium to hinder the diffusion coefficient of the ion, yet it appears that the intramolecular interactions in solution are causing a stronger decrease in self-diffusion than the introduction of a polymer mesh. This is potentially a result of supra-molecular aggregates formed by the ions and the solvent as was seen by Dupont *et al.* and others [22, 103] in different RTILs and solvents. In these aggregates, the ions are arranged in a non-rigid structure in which the ions' motion is correlated. A visual representation can be seen in Fig. 1.3. We believe that in the case for LiTFSI salt, self-diffusion measurements support similar supra-molecular structures. The salt forms large electrostatic aggregated ionic

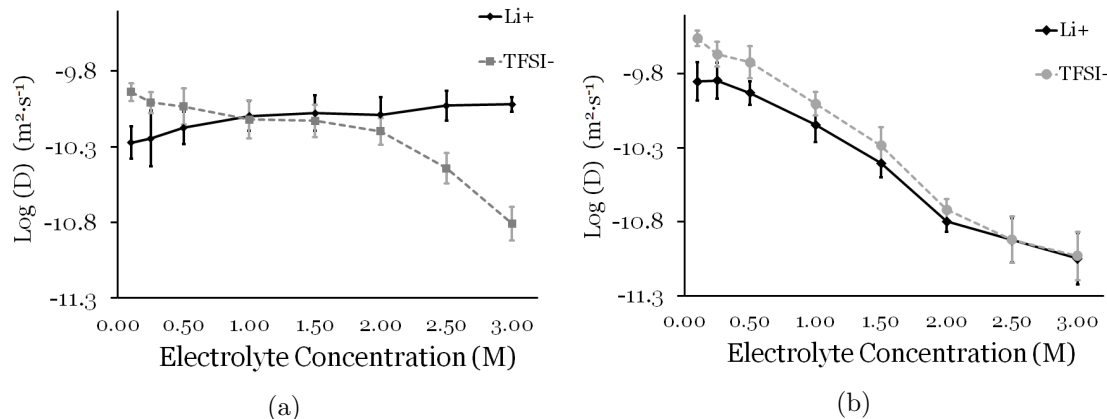


Figure 5.13: (a) Self-diffusion measurements of LiTFSI vs. electrolyte concentration embedded in PVDF-HFP co-polymer as measured by PFG-NMR. Solid line shows  $D$  for the cation and dashed line for anion. (b) is a repeat of Fig. 5.7 to allow for an easy comparison. The lines are meant only to guide the eye.

species in solution, but less so when embedded in a polymer network that interrupts the development of these large structures. These aggregates cause the general diffusion of both ions to be higher in a polymer network than in high concentration solutions.

To again compare results of self-diffusion to conductivities, the estimated conductivity was derived from self-diffusion and compared to directly measured ionic conductivity. This comparison is presented in Fig. 5.14a. Again, we see an excellent match between conductivities at low concentrations and as the concentration of ions increases the results diverge. This is again a result of the increased fraction of ion pairs that affect  $z_{\text{eff}}$ , a quantity that is not accounted for in our estimated conductivities. The divergence of the estimated conductivity from the directly measured ionic conductivity is greater than that seen for the electrolyte. This is a result of the self-diffusion coefficients in high concentrations being an order of magnitude higher than those of the equivalent concentrations samples without polymer. This is an indication that the polymer might be acting as an obstacle, inhibiting the formation of especially large ion-ion associated structures, resulting in an average

smaller species size that can diffuse faster.

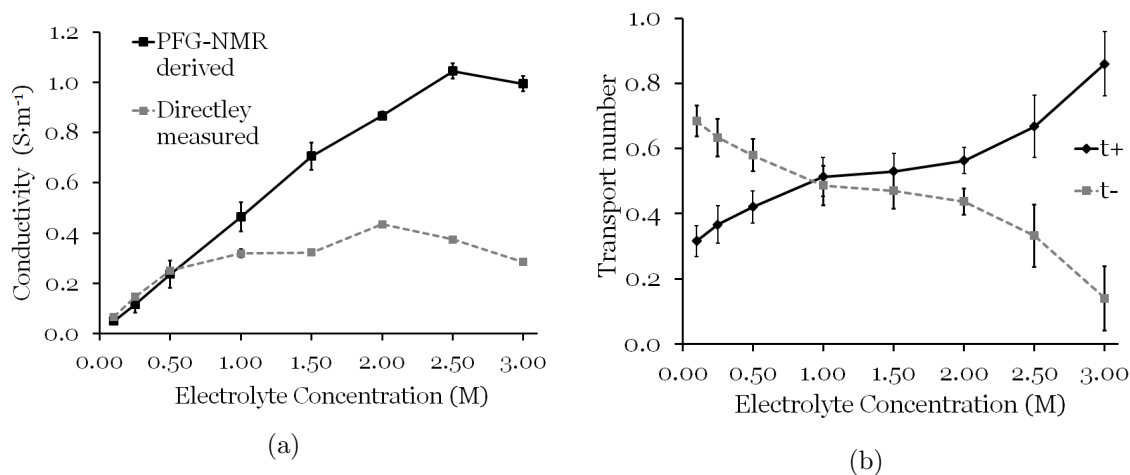


Figure 5.14: (a) Total conductivity of Gel samples derived from PFG-NMR self-diffusion measurements vs. directly measure conductivity for LiTFSI vs. salt concentration in PC. (b) Transport number derived from self-diffusion measurements. Solid line for the cation and dashed line for anion.

It is clear to see that for both solution and IEAP, self-diffusion does not predict conductivity parameters well for concentrations higher than  $\sim 0.5$  M. A more direct approach of mobility measurements is needed in order to make predictions or reach any conclusions regarding conduction mechanisms in either electrolyte solutions or co-polymer electrolyte systems. These direct approach measurements are discussed below.

### 5.3.3 Driven Diffusion in Solution Electrolyte Samples

eNMR is a more direct approach to assess conductivity as it directly measures the electrophoretic mobility of an ion in solution in response to an applied electric field. The NMR signal phase modulations are presented in Fig. 5.15a for the TFSI<sup>-</sup> anion and Fig. 5.15b for the Li<sup>+</sup> cation. In both Figs. the zeroth-order phase changes in response to the magnitude and direction of the applied, constant current through the samples. The direction

of the phase shift for the counterions is reverse in direction, indicating that the ions move in opposite directions in response to voltage. Mobility coefficients for the individual ions in solution samples were extracted from the measured zeroth-order phase shift vs. current flow through the sample.

A summary of the mobility coefficients for varying concentrations of LiTFSI in PC is presented in Fig. 5.16. It is clear to see that the more affected ion by the increase in concentration is the larger of the two: TFSI<sup>-</sup>. The mobility of the anion plummets by almost 3 orders of magnitude between 0.10 and 3.00 M, similar to what was seen in self-diffusion. This similarity is an indication that for the anion, the conductivity mechanism is based on the diffusivity of the ion. As discussed, in the Stokes-Einstein equation (Eq. 1.5), diffusion is inversely proportional to viscosity. With the increase in salt concentration, the total viscosity increases by a factor of 10 for each increase of 1.00 M. This effect explains the large decrease in mobility for the TFSI<sup>-</sup> anion. Considering this increase in viscosity should also affect the Li<sup>+</sup> cation, it is surprising to see that its mobility is hardly affected by the concentration increase.

With the initial increase in concentration from 0.10 to 0.50 M, the effects of solvation changes on the cation can be seen in  $\mu$  as we leave the infinitely diluted regime. As previously observed and discussed, the number of solvating molecules decreases with an increase in the solution's ionic strength [125, 126]. This decrease in  $r$  can explain the small increase in mobility observed between 0.25 and 1.00 M. Yet, with further increase in concentration, the mobility remains more or less constant for Li<sup>+</sup>. This contradicts two of our previous observations. We know the viscosity of solution increases by approximately a factor of 10 with the concentration increase from 2 M to 3 M. This has been both measured (Fig. 5.8a) and confirmed in the literature [123, 108]. Second, we measured a decrease in  $D_s$  for the same solution samples. The drop in measured self-diffusion for both ions

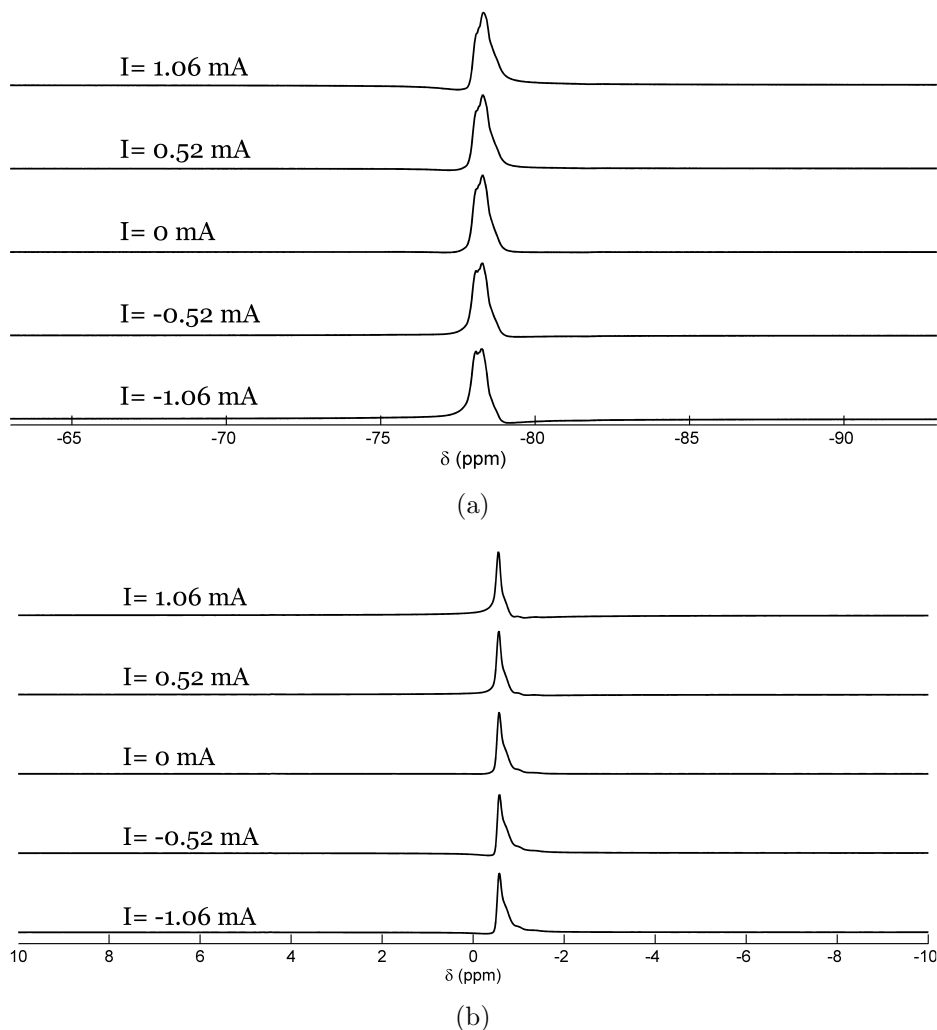


Figure 5.15: NMR spectra of 2.0 M LiTFSI in PC as a function of applied electric field. The zeroth-order phase of the peaks changes in response to the magnitude and direction of the applied electric field. (a) shows  $^{19}\text{F}$ -NMR of the TFSI $^-$  anion (b) shows  $^7\text{Li}$ -NMR spectra of the Li $^+$  cation. All experiments were performed at 22  $^\circ\text{C}$  using our home-built eNMR probe and eNMR pulse sequence (described in detail in Section 3.5)

means the diffusivity of both ions is affected in a similar manner, yet their mobility is not. From this contradictory information, we must conclude there is a different conduction mechanism for Li $^+$ , one that relies on factors other than the ion's diffusivity and causes a

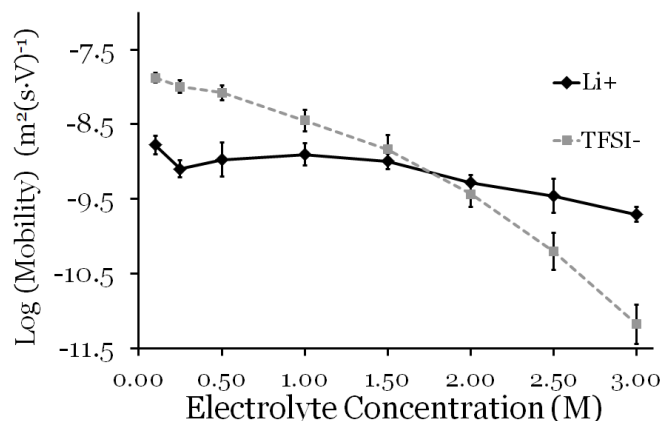


Figure 5.16: Electrophoretic mobility measurements for LiTFSI vs. salt concentration in PC as measured by eNMR. Solid line shows  $D$  for the cation and dashed line for anion.

divergence from the Nernst-Einstein relation (Eq. 1.15). We suggest that  $\text{Li}^+$ 's conduction mechanism follows a non-Stokesian charge transport that resembles the Grotthuss proton hopping mechanism in water [132, 133] and vacancy  $\text{Li}^+$  conduction that is seen in solid materials [134, 135].

In acidic or basic conditions at high enough concentration, water molecules form a hydrogen bond network that can conduct the charge carried by a proton by what is termed a structural diffusion mechanism or Grotthuss proton hopping [136]. By forming a bond with a proton in a neighbouring ion and breaking an existing bond in the hydronium ion, a proton can “move” through the length a solution without any single ion required to move the entire distance. Since the same bond that breaks also forms immediately, there is no total energy difference and since the distances are small and the hydrogen bonding network already exists, the energy barrier is small [132]. It is important to note, because this mechanism does not involve any movement of a nucleus, it can not be observed using NMR methods. This mechanism, where a structural feature moves through the material, results in much higher conductance than predicted by the diffusivity of water.

For the solid case, it has been established that  $\text{Li}^+$  conduction becomes depletion based in solids such as inorganic solid electrolytes [137, 138]. In such materials, the relatively mobile ion can hop from one site to another in the crystal structure. This mechanism requires the existence of a hole; a vacancy of an energetically equivalent site to hop into. In solid vacancy conduction, the energy barrier to create a hole may be large as it involves breaking bonds that link an atom in the crystal structure to its neighbours [139].

In our case, it is possible that  $\text{Li}^+$  conduction occurs by a mechanism having elements similar to both of these. The conduction itself which is similar to the vacancy based conduction seen in the solid case, is made possible by aggregates that are formed in solution, similar to the Grotthuss case. In LiTFSI electrolyte solution, there is no solid crystal but the proximity of the ions to each other in this concentrated solution creates large supra-molecular structure that resembles the hydrogen bonded network formed by water. With an increased concentration of ions in solution, large ionic aggregates are formed due to the electrostatic forces between the ions (Fig.1.3, [22]). When the distances between the ions are small enough, the Debye length of one ion overlaps, or nearly so, with a neighbouring ion. In this very viscous crowded case, the diffusion coefficients of the ions are small, as they are bound together in an ordered structure so diffusion requires overcoming the electrostatic forces between the ions. The measured self-diffusion in electrolyte solution agrees with this assumption as was seen in Fig. 5.7 where the ions' self-diffusion is very small at high concentrations. This arrangement, however, could allow fast vacancy migration similar to that in the solid state.

Previous observations [124, 140] in other solvents (*e.g.* sulfolane, succinonitrile) and with other anions (*e.g.*  $\text{BF}_4^-$ , bis(fluorosulfonyl)amide) have shown that the self-diffusion coefficient of  $\text{Li}^+$  becomes larger than that of the anion in concentrated solutions. In this suggested mechanism, the solvent and anion create aggregates which are involved in bridg-

ing coordination of  $\text{Li}^+$  that can be observed in increased self-diffusion coefficients. These aggregates are non-rigid associated species in which the motion of the ions is correlated, and they provide a scaffold for increased  $\text{Li}^+$  hopping [124]. This mechanism does not require external potential and is random in its direction. However, this increase in  $\text{Li}^+$  self-diffusion is not observed in our case of LiTFSI dissolved in PC. Based on our observations of increased  $\text{Li}^+$  mobility, we believe certain boundary conditions are necessary for  $\text{Li}^+$  hopping to occur and those are satisfied by applying an electric field.

As an electric field is applied, the  $\text{Li}^+$  ion closest to the cathode moves toward it, in response to the potential difference, leaving a vacant space, or a hole, in the supra-molecular structure, similar to the hole seen in solid Li ion conductivity. This newly formed vacancy allows for another  $\text{Li}^+$  ion to travel a small distance, perhaps even inside the same Debye sphere, to occupy it. This continues through the length of the solution, to the anode. The combination of transient movements of the  $\text{Li}^+$  leads to an effective conduction of the charge over the long distance between the electrodes. Due to the high concentration of solution,  $\text{Li}^+$  can travel from one anion to the other, without ever leaving the electrostatic sphere and never having to overcome electrostatic forces. In the absence of the driving potential, no holes are injected and the transport remain Stokes-Einstein based. In this mechanism the effects of higher viscosity, increased drag, and crowding are minimized as the ion does not need to diffuse large distances. This allows for faster current conduction that does not solely rely on diffusivity. As this mechanism relies on the existence of supramolecular ionic aggregates, in future research, it should be possible to test it by studying the effects of elevated temperatures, which would decrease the correlation length of the supramolecular structure, breaking the structures down and inhibiting  $\text{Li}^+$  conduction.

This divergence from diffusivity is emphasized when comparing the measured mobility to measured self-diffusion. Although self-diffusion of the anion is higher than that of the

cation for all concentrations, the mobility data shows a crossover between 1.50 and 2.00 M. At low concentrations, the mobility of TFSI<sup>-</sup> is higher by an order of magnitude than the Li<sup>+</sup> and at higher concentrations, the mobility of Li<sup>+</sup> becomes higher than TFSI<sup>-</sup>. The same effect can be seen in the transport numbers which are presented in Fig. 5.17. This shows that at low ionic concentrations, 90% of the current is carried by the TFSI<sup>-</sup> anion while at higher concentrations, the majority of the current (89%) is carried by the Li<sup>+</sup> making it practically a single ion conductor. This transport number shift from a current which is TFSI<sup>-</sup> dominant to Li<sup>+</sup> dominant is seen at around 2.00 M which explains the switch in behaviour of the IEAP device at similar concentrations as well as the maximum in conductivity. Since this crossover is not seen in self-diffusion in the electrolyte, we can conclude that Li<sup>+</sup>'s conduction does not follow the Nernst-Einstein relation and is not based on self-diffusion.

A very similar mechanism has been described independently by a research group in Wuhan, China[4]. Using a computational approach, Gao *et al.* have developed a model describing ion transport as an ion-vacancy coupled charge transfer reaction and can reasonably predict conductivities in lithium based electrolytes. This computational work and independently developed model strongly support the lithium hopping mechanism that was described here based on our eNMR measurements.

The effective charge,  $z_{\text{eff}}$ , can be derived using the ratio of measured mobility and self-diffusion (Eq. 1.17) and is plotted in Fig. 5.18 for both ions. The effective charge of Li<sup>+</sup> rises significantly at concentrations higher than 1.00 M, up to the point of being close to 1. This is initially surprising, as we have come to expect a decrease in effective charge with higher concentration of solute. Although this increase has been observed before with charge-delocalized ions like imidazolium-based cations [58], it is unexpected for small, spherical cations such as Li<sup>+</sup>. The suggested depletion based conduction mechanism can explain

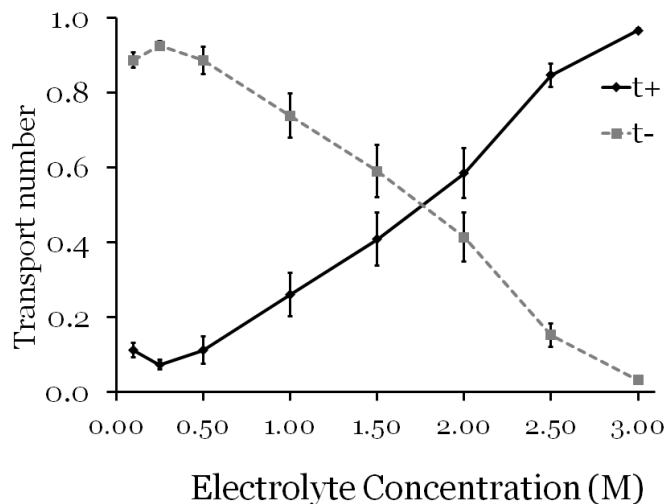


Figure 5.17: Transport number derived from driven diffusion measurements (eNMR) vs. salt concentration in PC. solid line for the cation and dashed line for anion.

this increase in  $z_{\text{eff}}$  as it requires a crowded mesh of ions to occur. This mechanism is only possible if the TFSI<sup>-</sup> ions create a close enough cluster that allows for quick movement between one overlapping Debye length to the next and therefore it is expected to occur exclusively in high concentrations.

To confirm the validity of our measurements, we compare eNMR derived conductivity to directly measured conductivity. eNMR derived conductivity can be calculated by plugging mobilities into Eq. 1.10. Using directly measured mobilities we arrive at the total ionic conductivity which includes the effects of  $z_{\text{eff}}$ . Results are shown in Fig. 5.19. We can see a consistently excellent match for all concentrations between directly measured conductivity to eNMR derived conductivity. This match proves that eNMR can successfully predict the conductivity of a sample to high accuracy, even for concentrated solutions. This means that eNMR indeed directly measures the motion of ionic species in response to an electric field. The improved match of eNMR measurements in comparison to self-diffusion indicates that there are clustering species that affect the conduction, especially for higher concentrations.

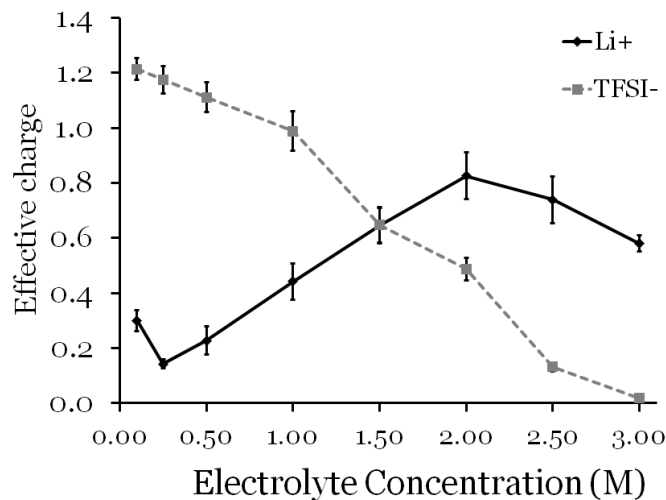


Figure 5.18: Effective charge ( $z_{\text{eff}}$ ) derived from driven diffusion measurements (eNMR) vs. salt concentration in PC. Solid line for the cation and dashed line for anion.

Because eNMR measures the displacement of ions under applied electric field, the measured motion goes through the same mechanism as in a typical conductivity measurement. By performing the eNMR experiment under the same chemical and physical conditions as the desired device, one can resolve the individual ionic conductivities and transport numbers of any magnetically visible ion.

### 5.3.4 Driven Diffusion in Polymer Electrolyte Samples

Attempts were made to measure mobility in IEAP samples. Successful mobility measurements in IEAPs would increase the range of possible devices to explore and allow us to investigate conduction mechanisms further, in different media. Sadly, measurements of eNMR in LiTFSI swollen PVDF-HFP were not successful. Attempts done on gelled samples left us with no measurable signal at the end of the pulse sequence due to the combination of short relaxation and signal decay due to self-diffusion.

As mentioned in Section 3.5.2, the eNMR pulse sequence does not use the stimulated

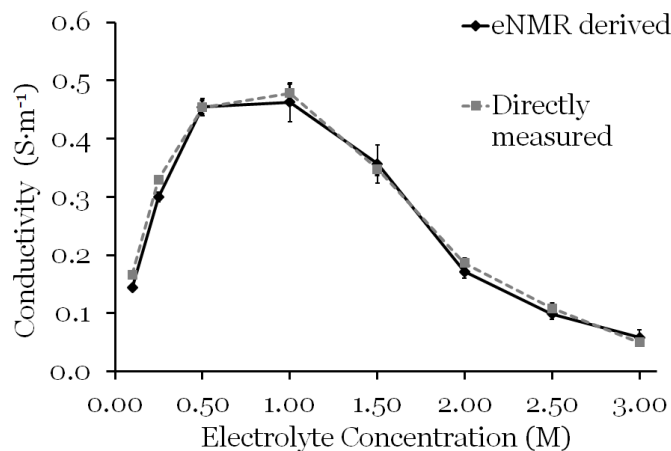


Figure 5.19: Total conductivity of electrolyte samples derived from eNMR driven diffusion measurements vs. directly measured conductivity for LiTFSI vs. salt concentration in PC. Graph shows excellent match between directly measured conductivity (dashed) to conductivity derived from eNMR measurements (solid).

echo method, and therefore  $T_2$  relaxation occurs for the entire duration of the pulse sequence. In addition, Brownian motion, which naturally occurs in the samples, further decays the signal in accordance to the Stejskal-Tanner equation (Eq. 2.3). Self-diffusion was in some cases faster than that seen in solution electrolyte samples, which in combination with the shorter relaxation times seen in polymers, reduced the measurable signal greatly. Attempts to minimize the effect of self-diffusion on the signal by shortening the diffusion time (max of  $\Delta = 60$  ms) and the magnetic field gradient strength (max of  $3.4 \frac{\text{G}}{\text{cm}}$ ) also reduces the measurable phase shift due to driven diffusion. In these attempts, some signal was left at the end of the measurement, but no phase shift was detected, eliminating our ability to calculate mobility coefficients.

One more added difficulty was observed after the eNMR attempts were done. The sample changed colour in addition to the formation of fine black particles near the electrode. These might be an indication of an electrochemical reaction. In our set-up, an

interface between the liquid electrolyte and the IEAPs exist and cannot be eliminated. This interface increases the total sample resistance and forces our constant current set-up to a higher voltage, well above the electrochemical window for all the components in the system (LiTFSI 4.4V [141] and PC -2 to +6V [142]). As the voltage exceeded the electrochemical window,  $\text{Li}^+$  may have been reduced to Li metal, which appeared as black grains near the electrode, and PC was oxidized, changing the colour of the solvent to brown. We believe that the changes to the sample would reduce the quality of the collected data and adjustments are required in order to reduce the total electrical resistance of the sample.

## 5.4 Conclusions

In order to learn about the mechanism behind innovative piezoionic materials, self-diffusion measurements were collected for both ions in LiTFSI salts dissolved in PC, both in solution and embedded in polymer. Comparing these results to directly measured conductivities results in poor prediction of conductive properties from self-diffusion, especially at high concentrations. The total conductivity estimated from self-diffusion has predicted consistently higher ionic conductivities, especially in high concentrations. This was expected as we know that self-diffusion does not account for the reduced ability of correlated ions to conduct charge.

In addition, measurements of the output voltage from the piezoionic material in sensor mode were in direct contradiction to transport numbers derived from self-diffusion measurements of solution samples. In IEAP samples on the other hand, an inversion of transport numbers was measured, but at a lower concentration. We conclude from these results that self-diffusion is a poor predictor of conductivity properties and has a tendency to overestimate the conduction ability of ions.

Our simple, horizontal eNMR probe has successfully measured the ionic mobility for

both ions in some samples. Comparing conductivity estimated from *in-situ* eNMR mobility measurements to directly measured conductivities has shown an excellent match. In addition, an inversion in transport numbers was measured at the same concentration as was seen in the output voltage measurements of devices in sensor mode. This demonstrates that eNMR can accurately predict conductive properties for NMR visible ions.

This inversion in transport numbers is explained by combining self-diffusion with mobility measurements to extract  $z_{\text{eff}}$  for each ion. This enabled us to see that lithium's effective charge increases with an increase in concentration, resulting in the  $\text{Li}^+$  carrying nearly 90% of the total current making it practically a single ion conductor. This result contradicts most diffusion based conductivity theory as  $\text{Li}^+$ 's conductivity is higher than its diffusivity suggests. This increase implies that a different conduction mechanism takes place.

We suggest from this data that at high concentrations  $\text{Li}^+$  conduction is by a mechanism similar to vacancy based diffusion which is possible due to supramolecular structures formed by the anion and the solvent. In this suggested mechanism the lithium ions can hop from occupied to vacant sites in the supramolecular ionic structures, without the need to overcome electrostatic interactions and solution viscosity. This hopping mechanism allows the system to perform better as a charge carrier than predictions based on the Nernst-Einstein relation.

## Chapter 6

# Chromophore Diffusion in Optical Filter Devices

### 6.1 Introduction

In addition to applications as touch sensors, artificial muscles, and iontronics, ion dense gels are the basis for some optical device applications. SWITCH Materials Inc. has developed a commercial optical filter for the automotive glazing industry utilizing electro-photochromic molecules. These chromophore molecules are integrated into an optical film, which is subsequently encapsulated into car sunroofs. The optical film can modulate the light transmission of a car sunroof in response to both light and electric potential [143]. By modulating the solar gain through the sunroof, climate control within the vehicle is possible without the need for active cooling or heating. This reduced load on the vehicle AC system can improve the vehicle's fuel economy. Unlike many other photochromic materials, these films do not show thermochromic behaviour - expanding their applications to a large range of temperatures.

The optical films are made by embedding chromophore molecules into a polymer gel electrolyte, which is coated between two sheets of transparent conducting electrodes. The polymer gel electrolyte acts as a conductive scaffold allowing current to propagate to the entire film with little resistance, minimizing voltage drop across the film. The chromophore

molecules selected for different applications are determined by the structure of the substituents, represented as R in Scheme 6.1. The chromophore molecules inter-convert between two isomers that have either high or low absorbance of visible light. Transition between those states happens in response to either specific wavelengths of light or to applied voltage [144]. The rate of conversion between these two states depends, in addition to other factors, on the diffusion rate of the chromophore molecules in the polymer gel electrolytes. In particular, diffusion of the chromophore to the transparent conducting electrode is a necessary step for the electrochromic dark-to-light state transition.

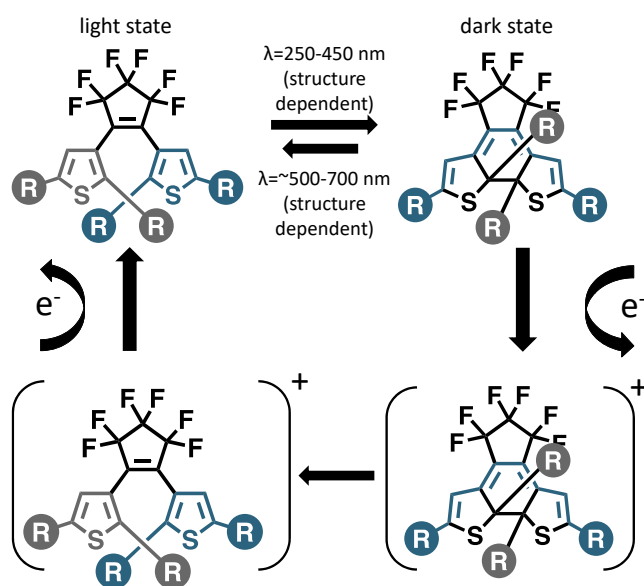


Figure 6.1: Chromophore inter-conversion as a response to voltage or a photon of wavelength  $\lambda$  for a common molecular structure [144]. The state on the right represents the closed-ring isomer which acts as an optical filter. Figure adapted from SWITCH Materials Inc. with permission.

To understand the performance limitations of devices based on these chromophores

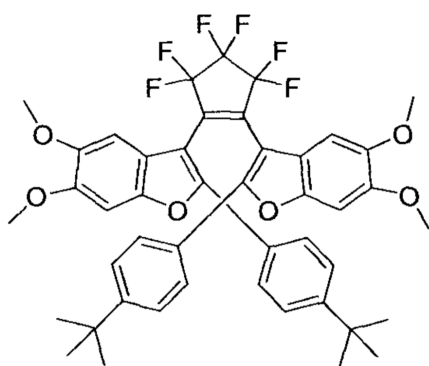
we collaborated with SWITCH Materials Inc. to measure the self-diffusion of a variety of chromophores in different solvent compositions as a function of temperature. These measurements will guide the development of devices with increased usability in more extreme climates.

In order to measure self-diffusion in conditions as similar as possible to operating conditions, our PFG-STE measuring setup was upgraded. A cooling attachment was added to allow for a larger range of temperatures and an external electric field was added to the probe. This allowed us to observe the effect an electric field has on the diffusion of these uncharged molecules, in an environment as similar as possible to that of a fully operational device.

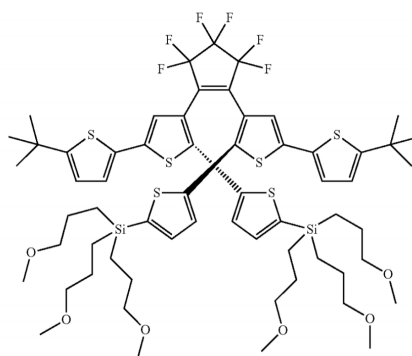
## 6.2 Methods

The system is composed of 10 wt% of chromophore molecules dissolved in a solution containing a combination of ester based solvents, a paramagnetic charge compensator, catalyst, and RTIL all embedded in a polymer network that was either crosslinked or left uncrosslinked. Fig. 6.1 shows the interconversion processes undergone by the chromophores, which differ in the structure of substituent R. Those discussed in this chapter are shown in Fig. 6.2. Sample preparation was done by the Research and Development team at SWITCH Materials Inc. by creating solutions, full formulation samples, or polymer films that could be illuminated to either the closed or open isomer of the chromophore. The detailed composition of the chromophore samples cannot be divulged as this information is protected under a non-disclosure agreement with SWITCH Materials Inc.

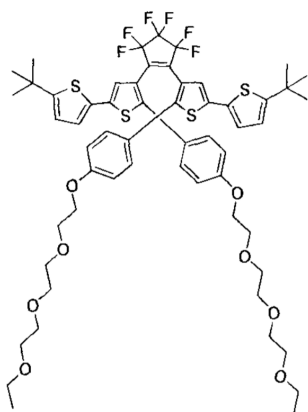
High resolution solution sample NMR spectra for each chromophore dissolved in Rhodisol<sup>®</sup>IRIS/butylene carbonate (BC) mixture were collected using <sup>19</sup>F-NMR on 8.4 T and 4.7 T home-built NMR spectrometers as well as a 9.4 T (400 MHz) Varian Unity Inova



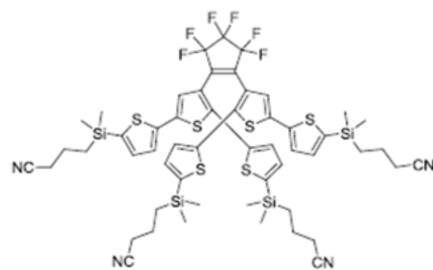
(a) Red chromophore S164



(b) Blue chromophore S158



(c) Blue chromophore S109



(d) Blue chromophore S304

Figure 6.2: Structure of chromophore molecules investigated in this chapter [144]

spectrometer. Spectrometers are described in detail in Chapter 3. Experimental parameters, such as pulse widths and frequencies, were set in accordance with the nuclei being investigated.

In order to push the photochromic reaction to either open or closed states, samples were illuminated with the appropriate wavelength of light. In order to activate the reaction to the open, clear state the samples were illuminated for a minimum of 4 hours by a low-pressure sodium lamp (Philips 179753 SOX 55 W) emitting at wavelength  $\nu=589$  nm. To push the reaction to the closed, opaque state, a homemade UV LED light box containing three 5 mm LEDs emitting UV light of  $\nu=380$  nm was used for a minimum of 10 hours.

Self-diffusion coefficients of the chromophores and solution components were measured using  $^{19}\text{F}$  PFG-STE NMR (full pulse sequence is presented in Fig. 2.2). Experiments used a home-built PFG probe [2] in a home-built NMR spectrometer [89] operating at 8.4 T. Temperature control was achieved using a Bruker B-VT-1000 temperature control unit. More information regarding the spectrometer and the setup can be found in Chapter 3.

Diffusion time,  $\Delta$ , was varied between 350 and 700 ms, depending on the diffusion rate of the sample. A short gradient pulse of  $\delta=318$   $\mu\text{s}$  was applied in varying strength from approximately  $g = 200 \frac{\text{G}}{\text{cm}}$  to  $3000 \frac{\text{G}}{\text{cm}}$ . This short pulse was necessary due to the short  $T_2$  times typical for polymer gels [63]. A longitudinal acquisition delay of  $T=10$  ms was used in order to allow eddy currents from the magnetic field gradient pulses to decay before acquisition.

Measurements to explore the effects electric field has on self-diffusion coefficients were made using an apparatus shown in Fig. 6.3. The voltage applicator and the sample holder can be seen in Fig. 6.3a. The gelled sample was pressed between two sheets of conductive Indium Tin Oxide (ITO) covered with polyethylene terephthalate (PET) that both held the sample in place and were used to apply an electric potential across the film. This sample

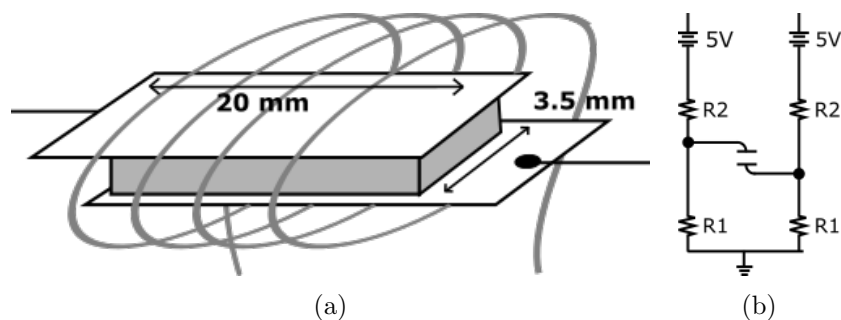


Figure 6.3: (a) Sample holder, showing electrodes and film, and (b) wiring diagram of gelled sample between ITO electrodes. Electrodes are shown in white, whilst the electromagnetic coil is in grey. Notice the electrode contacts are outside the RF coils.

holder was inserted into the RF coil of the PFG-NMR probe and the same experimental parameters were used as in the previous PFG-NMR experiments, other than the delay time which was extended to 10 s to minimize any accumulative resistive heating and avoid a state of equilibrium from charge accumulation near the electrodes (as described in Section 3.5 and Fig. 3.4). These conductive plates were connected to a 5 V source through a voltage divider that can be seen in Fig. 6.3b. While one source was open, the other was closed allowing a directional switch of the applied voltage. To further minimize the probable effect of resistive heating, an approach of using an alternating pattern between applied voltage and non-applied voltage scans was employed. The resistor ratio determines the voltage on one plate while the other was connected to ground, and thus the voltage across the sample was equal to  $V_{\text{out}}$  of the voltage divider according to  $V_{\text{plate}} = V_{\text{out}} \cdot \frac{R_1}{R_2 + R_1}$ . This voltage assumes the resistance of the device is significantly higher than that of the resistors. This assumption was confirmed by measuring the voltage across the sample. For a sample of thickness of  $200 \mu\text{m}$ , the maximum electric field is  $250 \left[ \frac{\text{V}}{\text{cm}} \right]$ . The 5 V source was driven by the NMR pulse programmer and therefore timed with sub-microsecond accuracy with respect to the total pulse sequence.

## 6.3 Results and Discussion

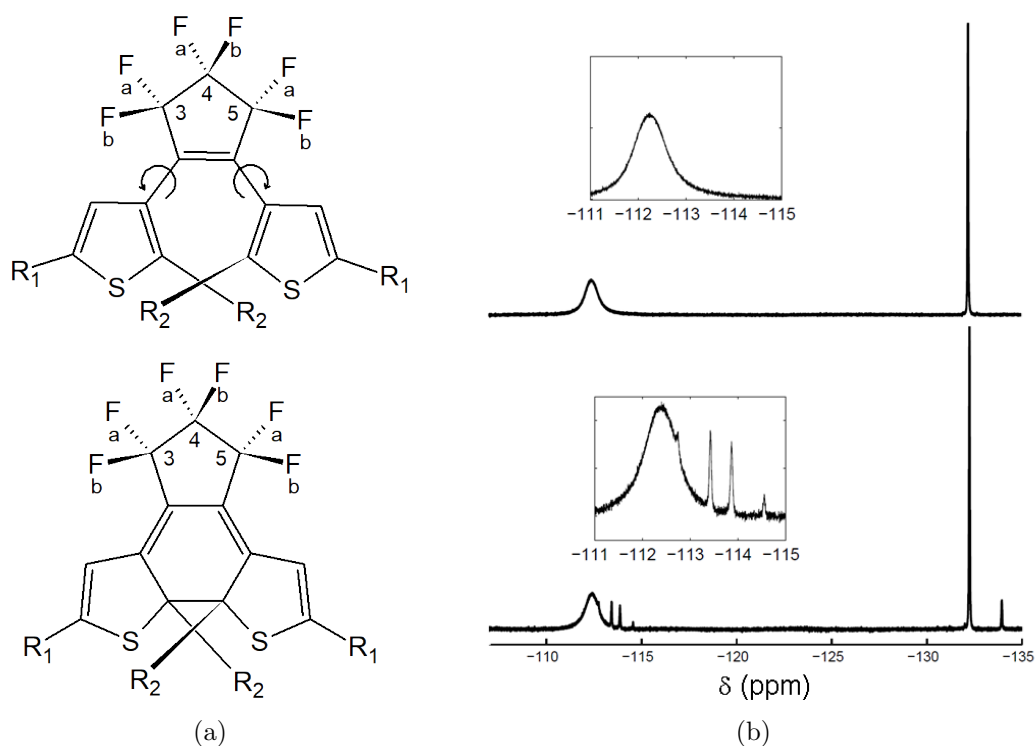


Figure 6.4: (a) The general molecular structure of a blue chromophore in its open form (upper) and closed (lower). Carbons 3, 4, and 5 of the cyclopentene ring are labelled. Out of plane Fs are labelled with b and in plane Fs are labelled with a [144]. The rotation around the single bond between the cyclopentene and the thiophene ring is marked with an arrow. (b) 1D <sup>19</sup>F NMR spectra, N= 256 scans, of S158 for both open (light) state (upper) and partially closed (dark) state (bottom). Spectrum collected on 400 MHz spectrometer using high resolution solution probe.

High resolution 1D <sup>19</sup>F solution spectra of chromophore S158 dissolved in Rhodiasolv<sup>®</sup> IRIS/BC mixture can be seen in Fig. 6.4 alongside the general molecular structure of the chromophore molecule. The spectra show the chromophore in two states: 1) completely open when the bis(terthiophene)ring is in its open form and 2) partially closed where both the open and closed states of the bis(terthiophene) ring are present. In the open state

spectrum (upper) two peaks are recognized. The upfield peak around -132 ppm is generally sharper and represents the two magnetically equivalent Fs on carbon 4 of the cyclopentene ring, 4Fa and 4Fb. The downfield peak, around -112 ppm, represents the four magnetically equivalent Fs on positions 3 and 5 of the cyclopentene ring. This line appears broad as a result of the hindered rotation of the bond between the cyclopentene ring and the thiophene ring (labelled with a rotation arrow on Fig. 6.4a). In the open state, this single C-C bond allows for rotation, but the geometry of the R arms hinders this rotation resulting in a broad line. This broadening is a result of the molecular motion being in the intermediate time scale relative to the frequency difference between the chemical shifts in the various conformations. For a detailed explanation regarding this broadening mechanism, see Part 7 of Spin Dynamics by Malcolm H. Levitt [60].

In the lower spectrum where the closed and open forms coexist, smaller sharp peaks can be seen near the open state peaks. These peaks indicate the structural difference between the closed and open forms. As the structure changes to form a closed bis(terthiophene) ring, the conjugated  $\pi$  system becomes longer and all the peaks shift upfield [145]. In addition, the geminal fluorines on carbon 3 are no longer equivalent ( $3\text{Fa} \neq 3\text{Fb}$ ) and are therefore coupled to each other. The same happens to fluorines 5Fa and 5Fb as they are as well not equivalent in the closed state. This creates an AB pattern quartet of  $J_{\text{AB}} = 280 \text{ Hz}$  and  $\Delta\nu_{\text{AB}} = 390 \text{ Hz}$  that are seen as 4 sharp peaks that appear, in addition to the open state broad peak, around -113.6 ppm. The rotation of the bond between the cyclopentene and the thiophene ring is eliminated when the ring is closed and the lack of free rotation in this bond forces the molecular symmetry to a  $C_2$  rotation about C4 of the cyclopentene ring. This means that in the closed state, the R arms are confined in an anti-parallel position where  $R_1$ s are facing above and below the plane of the cyclopentene ring. This symmetry makes the opposing Fs on carbons 3 and 5 equivalent ( $3\text{Fa} = 5\text{Fb}$  and  $5\text{Fa} = 3\text{Fb}$ ).

The small sharp peak that appears close to the open state peak, near -132 ppm is a result of the closed-state geminal fluorines in position 4 which remain equivalent. The peak is shifted upfield, again, due to the change in the conjugated  $\pi$  system. These fluorines are coupled to the fluorines in the vicinal positions, but the F-C-C-F coupling is too small ( $\sim 2$  Hz) to be resolved [146].

This solution spectrum allows us to resolve the closed state peaks from the open state. Yet, a much lower resolution was achieved for the viscous uncrosslinked full formulation samples and even more so for the crosslinked samples (linewidths in the order of  $\sim 500$ - $1000$  Hz or larger). From this, it was determined impossible to distinguish the dark and light state in a crosslinked sample. The linewidths were especially large for the red chromophore, S164, raising a question regarding the structure and dynamics of the molecules and led to further investigation described below.

In the measurements of the red chromophore, S164, generally broader lines were observed with interesting shoulders around both of the major peaks (see Fig. 6.5). It was initially suspected that these shoulders might be a sign of molecular degradation due to oxygen exposure or cycling fatigue between the open and closed states. In order to examine these shoulder peaks, samples with different amounts of air exposure and different number of open/closed cycles were examined. All samples showed the same spectral features. In an attempt to see whether solvent interactions were causing the shoulders, the chromophore was tested in a variety of solvents: butylene carbonate (BC), acetone, deuterated chloroform and methanol. The shoulders appeared in all solvents except acetone.

Higher resolution, variable temperature measurements of the liquid samples were taken using the 400 MHz Varian Unity Inova spectrometer and can be seen in Fig. 6.7. These spectra are of the fully open state and surprisingly show an AB pattern similar to that identified in the closed state spectrum in previous measurements. This time, the sharp

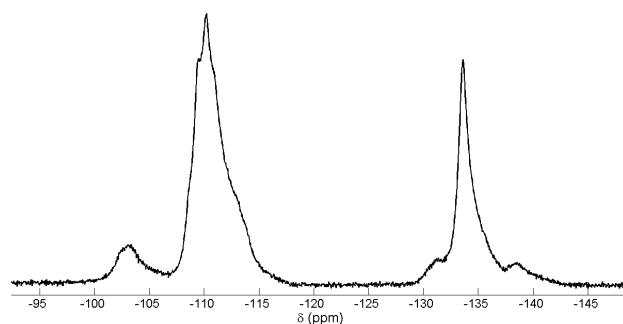


Figure 6.5:  $^{19}\text{F}$  NMR measurements of S164 chromophore in the open state dissolved in Rhodiasolv<sup>®</sup> IRIS/BC. The shoulders are visible around -102, -131, and -137 ppm. Spectrum collected on 360 MHz spectrometer using horizontal diffusion PFG-NMR probe.

peaks appear around the central broad peak and are not shifted upfield. Recall that the upfield shift was a result of the change in length of the conjugated system in the closed ring. In this case, there is no change in the conjugated system as the molecule is still in its open state and the length of the conjugated system did not change.

As was mentioned before, the AB pattern in the closed state is a result of the inequivalence of fluorines 5Fa and 5Fb, as well as 3Fa and 3Fb, due to the rigid bond between the cyclopentene and the thiophene ring. When the arms are free to move, they can spend time in either of the two arm positions: parallel or anti-parallel (see Fig. 6.6). When the transition between these arm positions occurs on an intermediate time scale, the broad lines that are a characteristic of the open state spectrum, appear as well (see Fig. 6.4). However, the spectra in Fig. 6.5 and 6.7 suggest that transitions between the parallel and anti-parallel states are hindered. When the arms face opposite directions (anti-parallel) they mimic the structure of a closed state molecule, resulting in the AB pattern split seen in the closed spectra. When facing the same direction (are parallel) the molecule has a  $C_s$  mirror symmetry about carbon 4, where 4Fa and 4Fb are inequivalent and split by each other. This symmetry makes fluorines 3Fa and 5Fb equivalent as well as 3Fb and 5Fa.

Both are split by geminal J couplings as couplings from vicinal fluorines are too small to resolve.

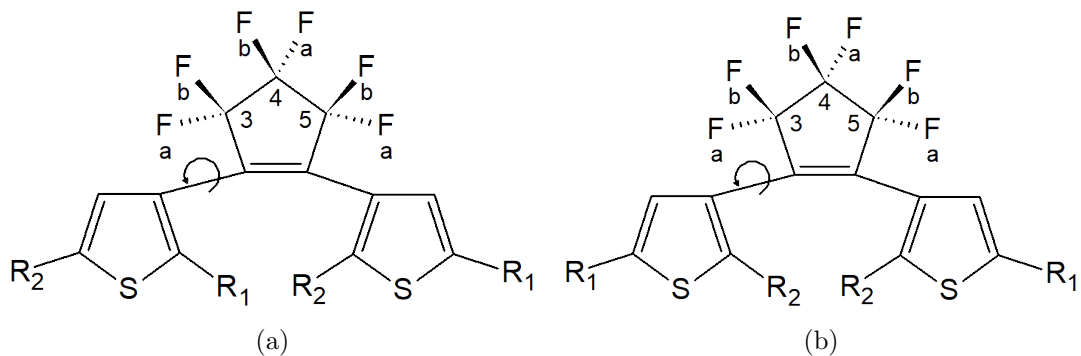


Figure 6.6: General structure of the open state chromophore in (a) parallel and (b) anti-parallel arm positions. The rotating bond is labelled with an arrow. The different arm positions change the symmetry of the molecule. The experiments suggest that a steric barrier impedes transitions between these parallel and anti-parallel conformations, but presumably significant rotational freedom within each conformation state exists.

As the molecule rotates between the two arm positions, the broad shoulders of couplings are formed and are clearly seen in Fig. 6.5. In the same spectrum, hints of the AB pattern are seen on top of the downfield peak. When looking at the higher resolution spectrum at room temperature shown in Fig. 6.7, we can easily recognize the AB pattern peaks at -110 ppm. Due to the slow motion of the arms in a viscous solution, the two arm positions are separated and are visible in the spectrum. As the solution is heated, transitions between the parallel and anti-parallel states become more rapid, and the spectra coalesce into a single time-averaged spectrum. Further heating sharpens the peaks even more. The fact that the shoulders are a result of limited molecular dynamics agrees with the fact that these shoulders are not present in samples dissolved in acetone, a low viscosity solvent (a factor of 10 lower than BC ( $0.3034 \frac{\text{mP}}{\text{s}}$  vs.  $2.98 \frac{\text{mP}}{\text{s}}$  [147, 148]), that allows rapid arm motion, similar to the high temperature spectra for more viscous solvents. These shoulders were only observed for S164 and are assumed to be a result of the large steric hindrance to

### 6.3. Results and Discussion

the rotation the R arms cause. Further investigation of the matter was not deemed crucial for a successful investigation of diffusion properties.

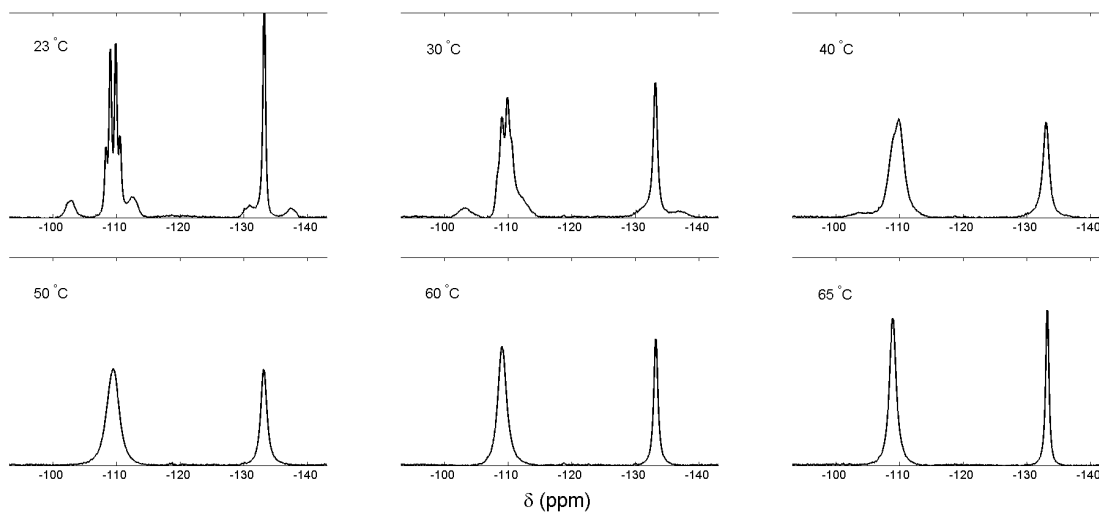


Figure 6.7: S164 dissolved in Rhodiasolv<sup>®</sup> IRIS/BC mixture  $^{19}\text{F}$  NMR measurements vs. temperature. At room temperature an AB pattern can be seen around -110 ppm which coalesce to the main peak above 30 °C. The shoulder peaks disappear above 40 °C and the peaks sharpen as temperature is increased further. Spectra collected on 400 MHz spectrometer using high resolution solution probe.

One of the important first steps in our diffusion investigation was to assess the diffusion of both dark and light optical states. The generally poor resolution of samples in the gelled state made it impossible to separate the two isomers in crosslinked samples for all chromophores. In order to overcome this, the films of crosslinked samples were illuminated in the glove box of SWITCH Materials Inc. with the appropriate light wavelength for an extended time (minimum of 24 hours) in order to ensure a maximal conversion of the chromophores to the desired state before the PFG-NMR measurements. A summary of both isomer diffusivities, for several chromophores, is presented in Table 6.1. The self-diffusion measurements show that self-diffusion of the two isomers are not dramatically different, but on closer inspection, the diffusion of the light state is generally faster than

for the dark state. As discussed, the steric packing of the molecule changes between the two states, and their effective radii are expected to be somewhat different and affect their self-diffusions.

Chromophore	D-Open $\times 10^{-7}$ [ $\frac{\text{cm}^2}{\text{s}}$ ]	D-Closed $\times 10^{-7}$ [ $\frac{\text{cm}^2}{\text{s}}$ ]
S109	$1.9 \pm 0.3$	$3.0 \pm 0.3$
S158	$2.1 \pm 0.2$	$2.6 \pm 0.3$
S304	$2.0 \pm 0.3$	$1.8 \pm 0.4$
S164	$2.2 \pm 0.8$	$2.6 \pm 0.3$

Table 6.1: Self-diffusion coefficients at room temperature of blue chromophores S109, S158, and S304 and red chromophore S164 in full formulation crosslinked samples.

When comparing the relative self-diffusion coefficients of blue chromophores, S109, S158, and S304 in the closed state to each other, we can see that S109, although it appears to be larger, has the fastest diffusion coefficient, followed by S158 and S304. The effect of the diffusion coefficient of the blue chromophore on the transition time for optical filters was analyzed and summarized in Table 6.2. The transition times, from dark to light state, of optical filters made with the different blue chromophore were measured at SWITCH Materials Inc. The comparison between S158 and S304 was done in highly-crosslinked polymer gel formulations. The comparison between S158 and S109 was done in uncrosslinked polymer gel formulations. In the uncrosslinked case, the optical filter made with S109 has a much faster transition time than S158, consistent with the relative diffusion coefficients measured by NMR. In the crosslinked formulation however, the optical filters with S158 and S304 have almost identical transition times. This suggests that while diffusion of the chromophore may play a role in the transition speed, there are other factors involved.

In order to measure diffusion coefficients under similar conditions to the expected operating conditions of devices, diffusion coefficients were measured at varying temperatures between 235 K and 300 K. Results can be seen in Fig. 6.8. The general trend shows an

### 6.3. Results and Discussion

Chromophore	Formulation	Transition time (s)
S158	Crosslinked	$69 \pm 7$
S304	Crosslinked	$65 \pm 6$
S158	Uncrosslinked	$32 \pm 6$
S109	Uncrosslinked	$21 \pm 2$

Table 6.2: Transition time comparison of blue chromophores in crosslinked and samples in full formulation that were left uncrosslinked. The transition time was between fully darkened state to 87.5% faded.

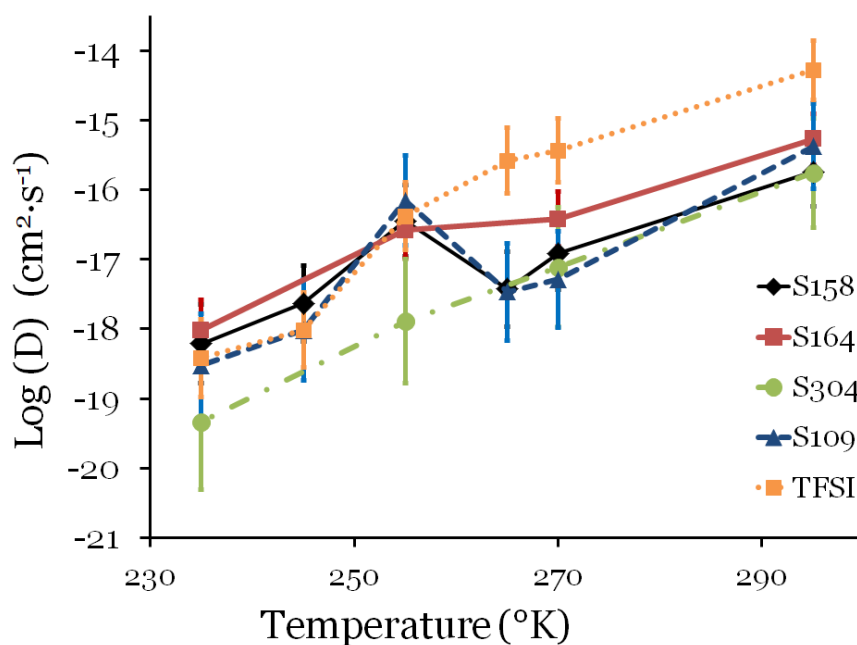


Figure 6.8: Self-diffusion measurements vs. temperature. Some of the chromophores have shown an expected decrease in  $D$  with a decrease in temperature, yet others have shown an unexpected increase in temperature around 250 K.

Arrhenius-like dependence on temperature, which indicates a Fickian diffusion behaviour, typical of polymers above their glass transition temperature ( $T_g$ ). Two of the chromophores (S109 and S158) show a local maximum in diffusion as a function of temperature. This is an unexpected behaviour according to the Einstein-Smoluchowski-Sutherland relation (Eq.

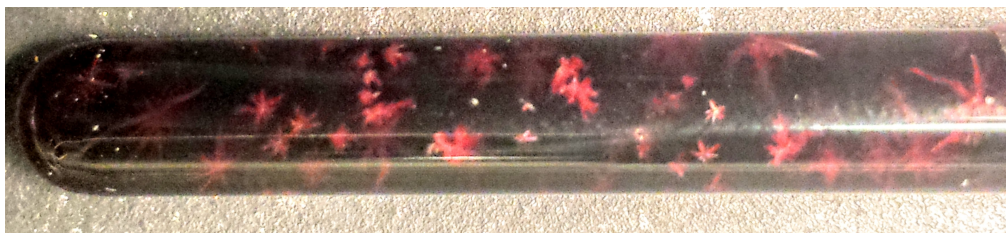


Figure 6.9: Uncrosslinked full formulation sample S164 after being left at 250 K overnight. Some crystals can be seen in the sample.

1.4). The increase in diffusion at 250 K might be explained by certain components of the solution reaching their freezing point and precipitating. The composition of the remaining solution is modified and has a lower viscosity allowing the chromophore to diffuse through a less viscous matrix. At the same temperature, a stronger decrease in the RTIL anion TFSI<sup>-</sup> self-diffusion is seen, perhaps an indication it is a component in the material precipitating out of solution. Visual inspection of a full formulation liquid sample left overnight at 250 K revealed crystallization in the samples, but their composition was not identified. Fig. 6.9 shows the S164 full formulation solution sample with the unidentified crystals. More research is required in order to answer these questions.

Another external condition required to fully mimic the operational conditions of the chromophore film is an applied electric field. The amount of the charged species in the sample does not exceed 1.5% w/w. The chromophore itself remains uncharged most of the time. It is charged briefly as it interconverts between the two isomers (see Scheme 6.1). Therefore, it was expected that the chromophore does not undergo electrophoretic diffusion and the motion should remain incoherent. It was predicted that applying an electric field to the electroactive gel would affect the charge distribution of the polymer gel itself. This will cause a change in the interactions between the ions in solution and the polymer network, resulting in changes to self-diffusion coefficients, but will not create electrophoretic motion for the chromophore molecules.

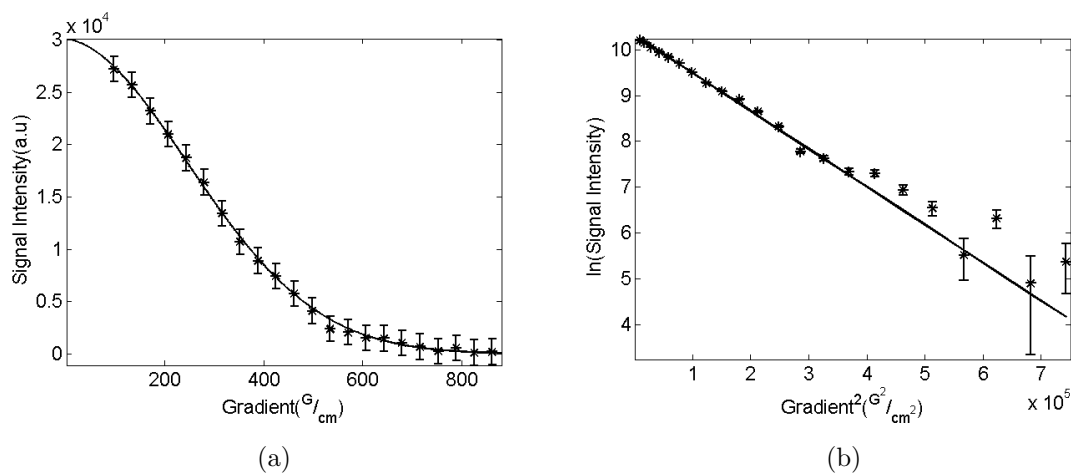


Figure 6.10: Example of a diffusion experiment for chromophore S109 in full crosslinked formulation with a diffusion time  $\Delta = 425$  ms, performed at  $22^\circ\text{C}$ . (a) shows the chromophore fluorine peak integration vs. gradient strength. The data is fitted to show a Gaussian decay of the signal with an increase in gradient strength. (b) shows the same data, plotted as the natural logarithm of the signal intensity vs the gradient strength squared to linearize the Gaussian behaviour of the Stejskal-Tanner diffusion equation. Both figures show excellent fits to a single diffusion coefficient of  $D = (1.9 \pm 0.3) \times 10^{-7} [\frac{\text{cm}^2}{\text{s}}]$ .

Because the electric field does not directly affect the diffusion of the chromophore, it is expected that self-diffusion would remain unaltered, i.e. mostly thermally dependent and random (Brownian motion). This incoherent motion will create a decay in the signal with a magnetic field gradient increase but not a phase modulation. More information regarding the difference between coherent and incoherent diffusion and their effects on the NMR experiment can be found in Chapter 2.

Figures 6.10 and 6.11 show an example of the diffusion measurement done on chromophore S109 in the open state with and without an external applied voltage. The voltage increased the noise by about 20% as the electrodes were placed directly inside the RF coil. The results are summarized in Table 6.3. Measurements of self-diffusion under an applied voltage show hints of faster diffusion. The increase observed is about 5%, and is not statistically significant. However, this small increase in self-diffusion is present in all

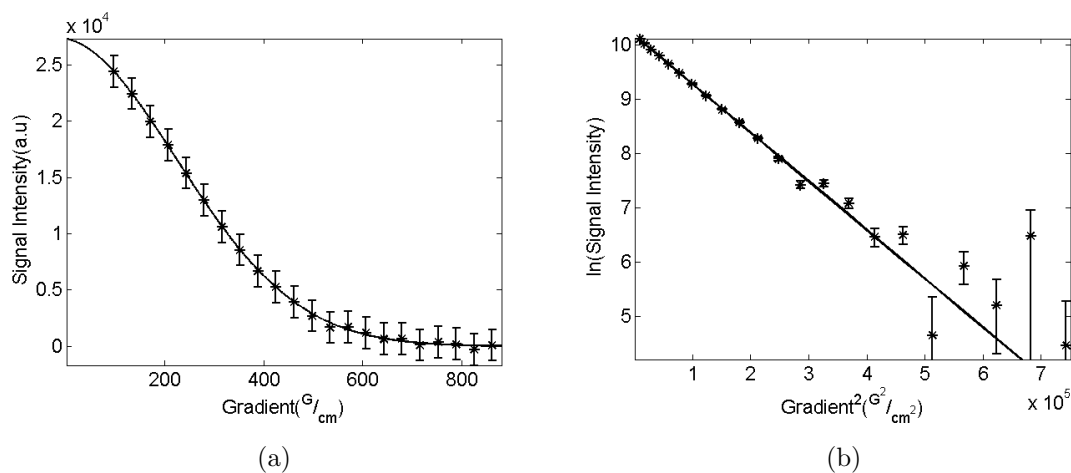


Figure 6.11: Example of a diffusion experiment under applied voltage for chromophore S109 in full crosslinked formulation with a diffusion time  $\Delta = 425$  ms, performed at  $22^\circ\text{C}$ . (a) shows the chromophore fluorine peak integration vs. gradient strength. The data is fitted to show a Gaussian decay of the signal with an increase in gradient strength. (b) shows the same data, plotted as the natural logarithm of the signal intensity vs the gradient strength squared to linearize the Gaussian behaviour of the Stejskal-Tanner diffusion equation. Both figures show excellent fits to a single diffusion coefficient of  $D = (2.0 \pm 0.5) \times 10^{-7} [\frac{\text{cm}^2}{\text{s}}]$ .

three chromophores tested. This suggests that the chromophore molecules indeed diffuse faster through the polymer when voltage is applied.

This increase in self-diffusion might be a result of small changes to the sample's temperature caused by resistive heating. The applied voltage to the sample produces heat according to Joule's heating process (see Section 2.2.2) which might increase self-diffusion. Although the sample is embedded in a polymer gel (which is expected to minimize any effects of convection) self-diffusion coefficients depend on temperature both directly, and indirectly through viscosity (see Eq. 1.5). From extrapolations of our temperature dependent measurements (shown in Fig. 6.8), it is possible that such a small change in self-diffusion is a result of a temperature increase in the order of half a degree. Since precautions to minimize resistive heating were taken (by using a 10 s delay between scans in addition to an alternating pattern between applied voltage and non-applied voltage scans) we believe

the increase observed is not a result of resistive heating.

Another possibility is that this observed increase in self-diffusion results from the redistribution of charge for both chromophore and solvent molecules. The delocalized charge of the  $\pi$  system is easily polarized by an external electric field, resulting in an enhancement of the dipole moment of the molecule [149, 150]. This effect is especially prominent on large molecules due to their higher polarizability and even more so on molecules that contain halogens due to their relatively high electronegativity [151].

The change to the molecular dipole moment affects both the interaction of the chromophore with the polar solvent molecules and with the polymer itself. These new interactions can either increase or hinder diffusion, depending on many factors [152, 153]. In this case, the slight increase can be explained by the relatively large size ratio of the chromophore to the solvent. As seen in previous calculations, large molecules surrounded by smaller solvents have a tendency to increase their self-diffusion with an increase in dipole moment. The increased dipole moment causes a stronger interaction between the solute and solvent, effectively increasing its solvation layer and creating a larger solute-solvent complex. In the case of large solute and small solvent, the shape of this complex is more spherical in comparison to a less solvated solute. This spherical complex, although larger, diffuses up to 24% faster in comparison to a complex of the same size with a planar shape [154]. This mechanism may explain the slight increase in self-diffusion seen for chromophore molecules under an applied electric field. As the dipole moment of the chromophore is enhanced, the polar butylene carbonate (BC) solvent molecules increase their solvation, creating a large, more spherical complex with an increased self-diffusion through the polymer medium.

## 6.4. Conclusions

---

---

Chromophore	D (Control) $\times 10^{-7}$ [ $\frac{\text{cm}^2}{\text{s}}$ ]	D (applied V) $\times 10^{-7}$ [ $\frac{\text{cm}^2}{\text{s}}$ ]
S109	$1.9 \pm 0.3$	$2.0 \pm 0.5$
S158	$2.1 \pm 0.2$	$2.3 \pm 0.3$
S304	$2.0 \pm 0.2$	$2.1 \pm 0.4$

---

---

Table 6.3: Self-diffusion coefficients at room temperature of blue chromophores S109, S158, and S304 with and without applied voltage. Samples were prepared in full formulation and crosslinked as for an operating device.

## 6.4 Conclusions

The self-diffusion coefficients of chromophores under operating conditions of devices were measured using PFG-NMR. A total of four chromophores were examined in a vast variation of formulations and physical states ( $\sim 30$  samples), in order to optimize both the feasibility of the measurements, and to provide experimental data to assist in formulation decisions of future devices.

The dynamics of the general chromophore were investigated as NMR spectra of some samples showed unexpected shoulders. The collection of spectra in different solvents as well as temperature dependent spectra leads us to attribute these features to hindered dynamics in the molecules that depend on the different substituent groups and the differing molecular symmetries arising from the different substituent configurations.

The relation between diffusion and temperature has been investigated and showed a general decrease in self-diffusion with temperature decrease. It was observed that at 250 K the diffusion of the chromophore shows a non-Fickian behaviour and increases as the temperature decreases. It is likely that this is a result of some components precipitating out of solution, reducing the viscosity of the solution, causing the observed increase in D.

Measurements of self-diffusion under applied voltage showed consistent hints of faster diffusion, though the change observed was not statistically significant. A large change is

not expected because the chromophore itself is neutral most of the time. The small change in diffusivity may be due to changes in the sample's temperature due to resistive heating or changes to the dipole moment of the chromophore itself in response to the electric field. The change in the molecular dipole moment could cause a change in the molecular shape of the chromophore-solvent complex, resulting in a more spherical shape. This complex shape change would translate to a slight increase in self-diffusion with the application of an electric field.

The information provided by these measurements will be used in the determination of formulations that can be used for a wide range of operating temperatures. This increased temperature range will help and enhance the performance and usability of films used for automotive glazing and help increase fuel economy by reducing the need for active cooling or heating in automobiles.

## Chapter 7

# Vitrimers - Transport of Thermally Exchangeable Molecules

Transport measurements are of interest in many other classes of materials in addition to ion dense materials. In this chapter we focus on a very different system, where similar techniques again help illuminate mechanisms that are the source of interesting material properties. We investigate the dynamics and transport of crosslinker molecules in large scale polymers, as they can be the key to more efficient polymer recycling.

### 7.1 Introduction

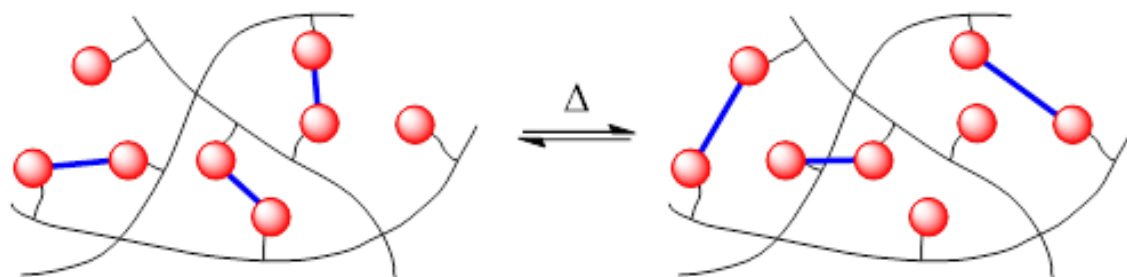
The introduction of plastics to the world enabled the development of an enormous array of products with positive effects on hygiene, health, and the economy. Yet, the widespread use of plastics causes an ongoing problem of excessive plastic waste. Due to their availability, relatively low price, and simple manufacturing, cross-linked polymers are being disposed of in massive quantities creating a plastic waste crisis. Both bulk and microplastic waste in the oceans have potential health and environmental impacts. These have been well researched in recent years, and they are of growing public concern (*e.g.* the ever growing Great Pacific Garbage Patch [155]). Better recycling of plastics to secondary materials is one possible solution to the plastic pollution problem as currently only  $\sim 10\%$  of plas-

tics manufactured between 1950 - 2015 have been recycled ( $\sim 600$  Mt) while approximately 4900 Mt were discarded to landfill [156].

Commercially manufactured plastics are generally divided into two broad categories: thermoset and thermoplastic. Thermoset plastics (such as polyurethane) are irreversibly crosslinked polymers and offer resilient, heat resistant end products that are non-remoldable or recyclable. Thermoplastics (such as nylon) are made of linear polymer chains and are less heat resistant and therefore can be more easily recycled as they can be melted down at high temperatures. Yet, they are less resistant to swelling or dissolution in chemical solvents and are not suitable for high temperature or high impact applications.

Vitrimers are a recently developed class of thermoset polymers [157, 158] in which molecular cross-links are thermally activated and are exchangeable. This means that these covalently bonded crosslinkers can shift from one bonding site to another upon heating, allowing for rearrangement of the whole network (see Scheme. 7.1). It is believed that as the system is heated above what is termed its topological freezing point temperature,  $T_v$ , the covalent bonds exchange at a significant rate, and the crosslinked system is moldable and therefore can be truly recycled to a new crosslinked polymer. Below  $T_v$ , the exchange reaction is slow and the vitrimer becomes rigid like a thermoset plastic [159]. The thermally labile nature of vitrimers allows them to be recast and recycled simply by heat and mechanical manipulation. These systems can have the strength and durability of crosslinked materials while still being recyclable over many cycles via cutting and compression molding above both  $T_v$  and the glass transition temperature,  $T_g$ . By changing the polymer backbone, additives or processing conditions, vitrimers can satisfy specific needs of mechanical properties and be made into a variety of applications [160].

These crosslinked polymers can flow like linear polymers when heated above their  $T_v$  and  $T_g$ . It has been suggested that when heated to this malleable state, the number of covalent



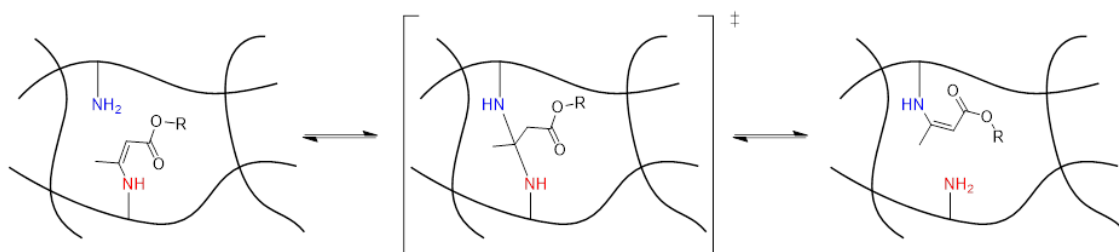
Scheme 7.1: General mechanism of thermally exchangeable covalent bonds in vitrimers. Red spheres represent moieties that can undergo reversible bond formation. The bond rearrangement leads to topological changes of the network itself.

lent bonds in vitrimers remains constant but the rate of bond exchange increases [160, 161]. This exchange can lead to a flow motion as the viscosity of the material decreases— similar to a viscous liquid that can flow with increased temperature. The rapid stress relaxation these materials exhibit, has also been attributed to this dynamic bonding property [157].

The Wolf group at UBC has suggested a new use for this rapid exchange reaction. By covalently attaching a tag molecule to vinylogous urethane linkages of a crosslinked polymer network (see Scheme 7.2), we can utilize the rapid bond exchange to allow the tag molecule to diffuse throughout the matrix. This new mechanism for molecular movement may provide greater control over the diffusion of additives through the polymer. In this chapter, the mechanism of this rapid bond exchange in polymers is investigated using diffusion NMR. By covalently attaching NMR visible molecules to the vinylogous urethane linkages, we are able to directly track their motion and learn about some of the contributing factors to this interesting molecular bond exchange.

## 7.2 Methods

In order to learn about the motion of the crosslinker, a set of vitrimer samples were made with different combinations of covalently bonded crosslinkers and tag molecules. Samples



Scheme 7.2: Vinylogous urethane exchange reaction of a pendant molecule covalently attached to a crosslinked polymer, resulting in a net movement of the polymer. Vinylogous urethane exchange is proposed to proceed through a tetrahedral intermediate which means the molecule is always attached to the polymer [160].

were prepared by Taylor D. Wright in Dr. Michael Wolf's lab at UBC and the sample preparation is described in detail in Appendix A. All polymers had the same backbone of polydimethylsiloxane (PDMS) random copolymer containing pendant propylamine groups to create PDMS-NH<sub>2</sub> which can be seen in Fig. 7.1. The backbone was crosslinked with either an exchangeable vinylogous urethane crosslinker (VitCL - Fig. 7.2) or a non-exchangeable crosslinker, triethylene glycol dimethacrylate (Fig. 7.3) which created a dynamic or static network [162]. To attach the tag in an exchangeable or a static way, the propylamine groups were reacted with either 2,2,2-trifluoroethylacetoacetate or 2,2,2-trifluoroethyl methacrylate, respectively. The exchange reaction is based on a Michael addition reaction [163], in which the formed C-N bond tautomerizes between a single to a double C-N bond. While in the double bond state, the reaction can undergo the exchange. The exchangeable tag is presented in Fig. 7.4. With the non-exchangeable tag, shown in Fig. 7.5, the Michael reaction forms a single C-N bond which is thermodynamically less reactive and does not allow exchange. Heating to approximately 60 °C was expected to bring the samples above T<sub>v</sub> and therefore allow for diffusion based on vinylogous urethane exchange, as can be seen in Scheme 7.2.

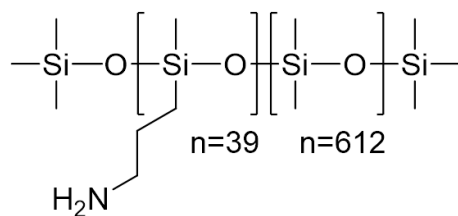
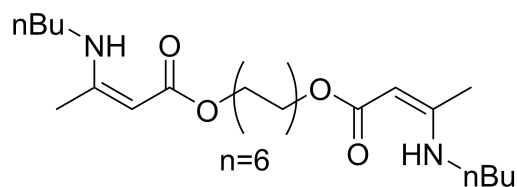
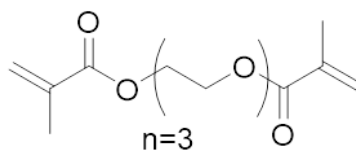
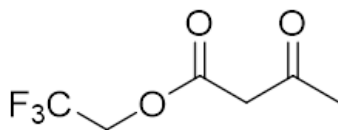
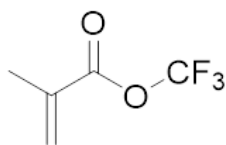
Figure 7.1: PDMS-NH<sub>2</sub> polymer structureFigure 7.2: Exchangeable crosslinker 1,12-dodecane-bis- $\beta$ -ketoenamine *n*-butyl

Figure 7.3: Non-exchangeable crosslinker triethylene glycol dimethacrylate.

Figure 7.4: Exchangeable tag 2,2,2-Trifluoroethylacetoacetate. The <sup>19</sup>F nuclei will be used as the NMR visible tag for this molecule.Figure 7.5: Nonexchangeable tag 2,2,2-trifluoroethyl methacrylate. The <sup>19</sup>F nuclei will be used as the NMR visible tag for this molecule.

In addition to the exchangeable tag mentioned, an exchangeable, F labelled, blue light-absorbing NMR visible tag was prepared in order to allow for visual tracking of the tag molecule as well as NMR. The synthetic steps are described in Appendix A and the resulting molecule can be seen in Fig. 7.6.

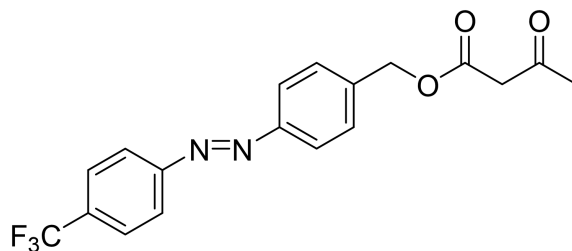


Figure 7.6: Orange coloured,  $^{19}\text{F}$  NMR visible exchangeable tag 4-trifluoromethyl-4'-methylacetoacetate azobenzene

To prepare the samples for the PFG-NMR experiment, PDMS-NH<sub>2</sub> (1 g, 0.02 mmol), 38 mg of exchangeable vinylogous urethane crosslinker or 23 mg of triethylene glycol dimethacrylate (0.08 mmol, 4 eq) or a non-exchange triethylene glycol dimethacrylate, *p*-toluenesulfonic acid (0.67 mg, 0.5 mol relative to moles of NH<sub>2</sub>, as a dilute solution in THF), 5 molar equivalents of an NMR visible tag, and 2.5 mL of THF were combined in a 20 mL vial and stirred using a magnetic stir bar for 5 minutes. The vial was degassed using a sonicator for 10 minutes. The solution was transferred to a silicone mold inside a glass desiccator, which was then evacuated. The system was placed under N<sub>2</sub>, covered in aluminum foil, and heated to 60 °C using an oil bath until the THF fully evaporated. The system was then heated to 100 °C and kept at that temperature for 18 hours under N<sub>2</sub>. Polymer samples were removed from the warm molds and stored in a refrigerator when not in use.

To prepare the samples to fit in the NMR tube, the polymer samples were cut into approximately 1.5 cm by 0.25 cm blocks using a razor blade and placed at the bottom of a glass NMR tube. The sample was then attached to a Schlenk-line and evacuated under

vacuum and then backfilled using dry  $N_2$ . This procedure was repeated twice. The tube was then sealed under either vacuum or dynamic  $N_2$  using a butane torch.

To create a heterogeneously loaded polymer sample, PDMS- $NH_2$  polymer was cut into  $3\text{ mm} \times 2\text{ cm}$  pieces. The lower 20% of the polymer was dipped in a solution of the orange coloured product (see Fig. 7.6), creating a heterogeneously colour loaded polymer. After being soaked overnight, the polymer was rinsed and dried before being sealed under  $N_2$  in an NMR tube. The process and resulting polymer sample can be seen in Fig. 7.7.

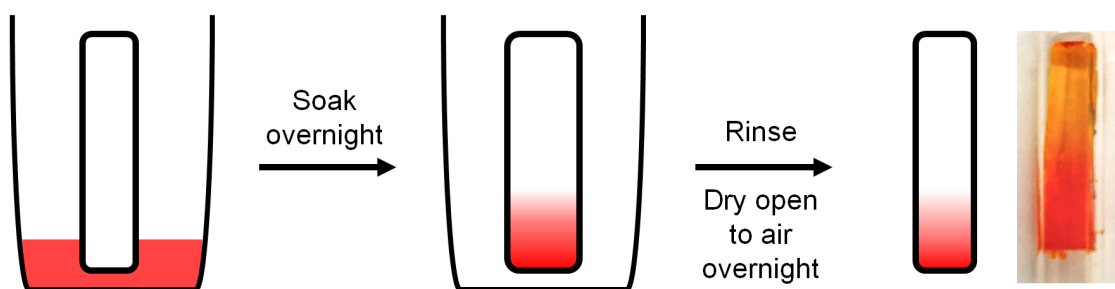


Figure 7.7: Sample heterogeneously loaded with 4-trifluoromethyl-4'-methylacetoacetate azobenzene. Notice, the concentration of the orange colour varies through the length of the sample.

In order to measure self-diffusion coefficients of the NMR visible tags,  $^{19}F$  or  $^1H$  PFG-STE NMR experiments were performed at varying temperatures using a home-built PFG probe [2] in a home-built NMR spectrometer [89] operating at 8.4 T, which are described in Chapter 3. Temperature control was achieved using a Bruker B-VT-1000 temperature control unit. A PFG-STE NMR pulse sequence was used, as described in Section 2.1 and presented in Fig. 2.2. A gradient pulse of  $\delta=318\ \mu\text{s}$  was applied in varying strength from about  $g = 500\ \frac{\text{G}}{\text{cm}}$  to  $3640\ \frac{\text{G}}{\text{cm}}$ . The diffusion time  $\Delta$  was varied between 700 and 2000 ms, according to the sample's diffusion rate and relaxation times. An acquisition delay of  $T=10\text{ ms}$  was used in order to allow eddy currents to decay before acquisition.

Self-diffusion measurements were fitted to a function similar to the Stejskal-Tanner

equation (see Eq. 2.4) with an added weighting factor:

$$\frac{S_{(g)}}{S_{(0)}} = (1-f) \exp\left(-\frac{4}{\pi^2} \gamma^2 g^2 \delta^2 \left(\Delta - \frac{\delta}{4}\right) D\right) + f, \quad (7.1)$$

where the weighting factor,  $(1-f)$ , accounts for some fraction,  $f$ , of the sample which does not participate in diffusion.

Relaxation measurements were carried out by either using an inversion recovery pulse sequence to measure spin-lattice relaxation ( $T_1$ ) or a spin echo in order to measure spin-spin relaxation ( $T_2$ ).

### 7.3 Results and Discussion

Temperature [ $^{\circ}\text{C}$ ]	time under heat [hours]	$D \times 10^{-12}$ [ $\frac{\text{m}^2}{\text{s}}$ ]	$f$	Figure
Room temperature	0	< 0.01	N/A	7.8a
40	4	3.1	0.03	7.8b
50	6	4.5	0.12	7.8c
60	8	6.5	0.50	7.8d
70	10	< 0.01	N/A	7.8e
80	12	< 0.01	N/A	
90	14	< 0.01	N/A	
100	16	< 0.01	N/A	
110	17	< 0.01	N/A	
120	18	< 0.01	N/A	7.8f

Table 7.1: Self-diffusion coefficients of vitrimer sample PD1a vs. temperature. The measurements were taken consecutively, the first measurement being the one at room temperature.

Initial PFG-NMR measurements of self-diffusion vs. temperature for a sample containing both an exchangeable crosslinker and an exchangeable tag, PD1a, can be seen in Fig. 7.8 and the numerical values extracted from this data are in Table 7.1, which sum-

### 7.3. Results and Discussion

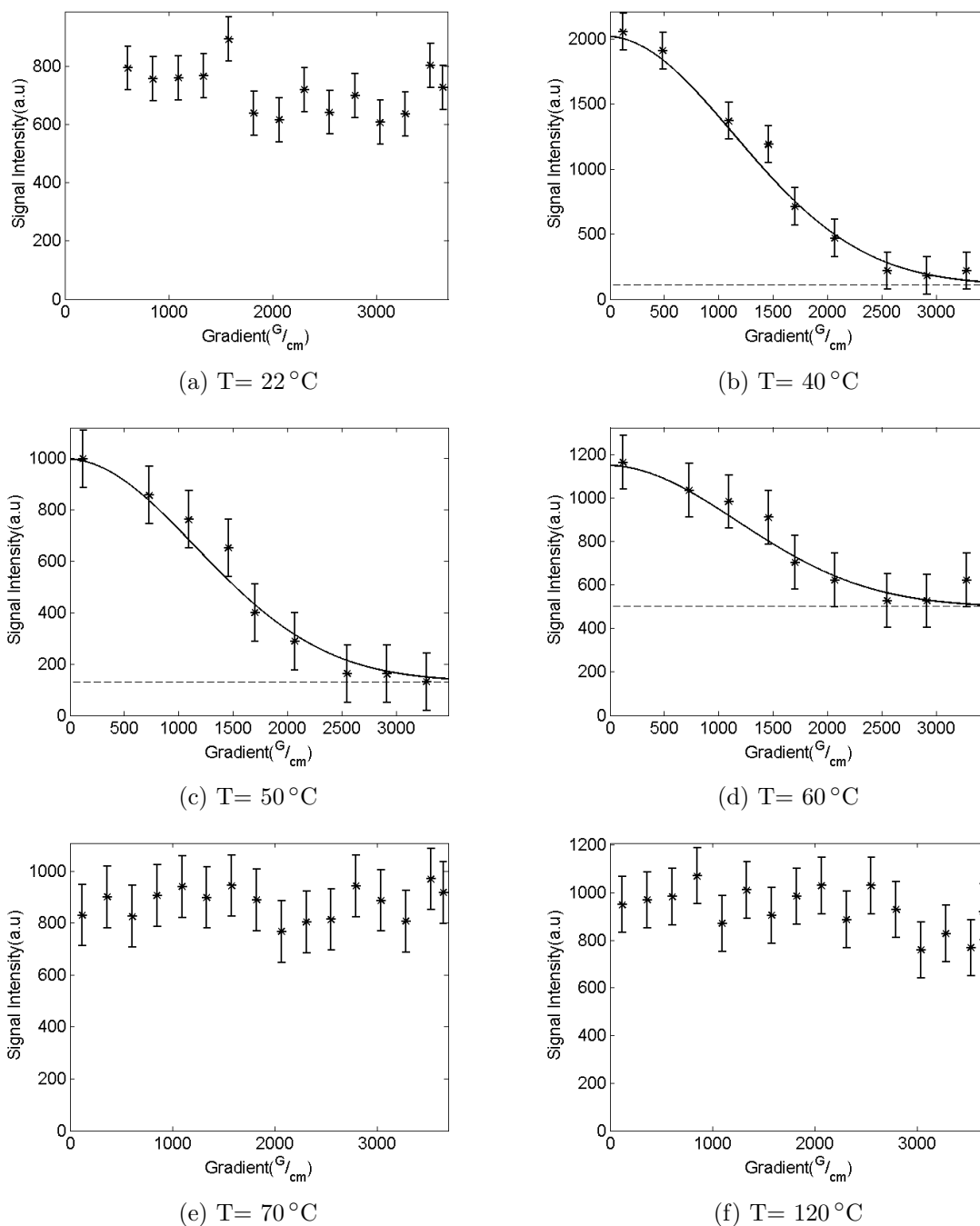


Figure 7.8: PFG-STE NMR signal intensity vs. magnetic field gradient strength of sample PD1a as it is heated from room temperature to 120 °C. Solid line shows the Gaussian fit and dashed line shows the weighting factor  $f$ . Numerical values are provided in Table 7.1.

marizes the results. Starting from room temperature in Fig. 7.8(a) we see no measurable diffusion. When the sample was heated at 40 °C for 3 hours the measurements show the typical Gaussian decay that can be seen in Fig. 7.8(b), which is fitted with a self-diffusion coefficient of  $3.1 \times 10^{-12} \frac{\text{m}^2}{\text{s}}$ . An added dashed line represents the weighting factor mentioned in Eq. 7.1. This factor,  $f$ , shows the fraction of the sample which did not participate in self-diffusion and can be seen in the figures as the amount of signal which does not present the Gaussian decay expected from a PFG-NMR experiment of a diffusing species. Fig. 7.8(c) shows the signal after two more hours of heating to 50 °C. Here the extent of the weighting factor increases, and a larger portion of the sample does not show diffusive behaviour. The portion that does diffuse, shows a 50% higher diffusion coefficient. Fig. 7.8(d) shows the signal decay vs. gradient strength for the sample after being heated for another two hours at 60 °C. The diffusion coefficient measured increases by another 45%, but the weighting factor nearly tripled to approximately 50% of the sample. As the sample was heated further to 70 °C, after spending 10 accumulative hours under heating, the self-diffusion coefficients measured for PD1a decayed until it was no longer possible to measure in the existing set-up. Further heating up to 120 °C did not regenerate the diffusion and it remained undetectable. These measurements raised two related questions: why does only a fraction of the sample contribute to the diffusion, and why does the fraction change with time? In order to answer these questions, further investigations were undertaken, discussed below.

In order to confirm that oxidation was not the cause of this loss of diffusivity, the experiments were repeated with samples open to air, sealed under vacuum, and sealed under inert N<sub>2</sub> gas. The same decrease in the diffusing fraction (increase in  $f$ ) and decrease in self-diffusion were observed under all conditions.

To assess whether the loss of diffusivity factor was a result of time spent at temper-

### 7.3. Results and Discussion

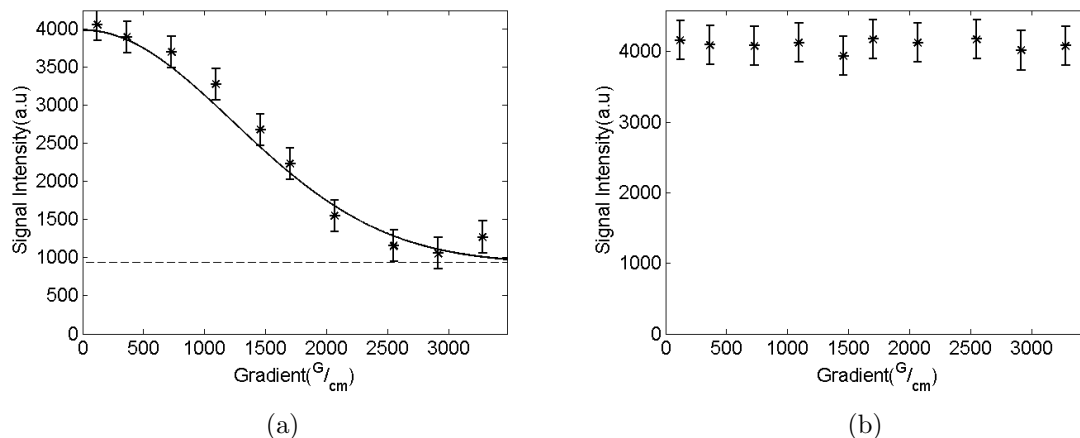


Figure 7.9: STEPFPG-NMR experimental results for D of Sample PD1b, performed at  $60^{\circ}\text{C}$ . (a) shows the diffusion measurements as the sample reached temperature. The solid line shows the Gaussian fit and the dashed line shows the weighting factor  $f$ . D was measured at  $3.2 \times 10^{-12} \frac{\text{m}^2}{\text{s}}$  with a weighting factor  $f = 0.23$ . (b) shows the same experiment and the same sample after being kept at the same temperature for 10 hours.

ature or a result of increased temperature, the experiment was repeated at the highest temperature diffusion was measured. A new piece of the same sample, PD1b, was heated to  $60^{\circ}\text{C}$ . The diffusion was measured a few minutes after reaching temperature and ten hours after being kept at the same temperature. The results can be seen in Fig. 7.9 where the typical decay of the NMR signal with increase in the magnetic field gradient can be seen, as expected of a diffusing sample. Data analysis showed an initial diffusion coefficient of  $3.2 \times 10^{-12} \frac{\text{m}^2}{\text{s}}$  with a weighting factor  $f = 0.23$ . Measurements taken after ten hours of heating do not show the Gaussian decay of the signal, indicating an unmeasurable diffusion rate ( $< 10^{-14} \frac{\text{m}^2}{\text{s}}$ ). Decay of diffusion due to time spent under heat was observed in many repeated experiments, following the same sample preparation procedures and it was concluded that self-diffusion coefficients decay with exposure to heat. It is therefore important to note that the self-diffusion coefficients were changing during the PFG-NMR experiments. Due to the time required for NMR signal averaging, the shortest experiment

possible was one hour. This signal averaging results in an averaged self-diffusion coefficient over the experiment, limiting the quantitative conclusions that can be drawn. By comparing the effect of different compositions, conditions, and stimuli on the presence or absence of diffusion we are able to learn about the conditions that lead to or eliminate diffusion.

In general, diffusion of the tag indicates either movement of the polymer network itself as a whole or exchange reactions transferring the tag between polymer chains. To ensure measurements do not simply represent the polymer backbone motion, the experiment was repeated with a non-exchangeable tag. The results are summarized in Table 7.2. Samples PD1 and PD2, which were made with an exchangeable tag (2,2,2- Trifluoroethylacetoacetate) were found to have initial self-diffusion coefficients on the order of  $10^{-12} \frac{\text{m}^2}{\text{s}}$  at  $60^\circ\text{C}$ , while sample PD3, which has no exchangeable tag, showed no measurable self-diffusion at any temperature. The measured self-diffusion coefficients of samples PD1 and PD2 are comparable to the diffusion rates of penetrant *n*-heptane through a crosslinked polyamide at similar temperatures [164]. This supports the conclusion that diffusion in these samples occurred as a result of the exchangeable tag and not of the bulk movement of the polymer chains, as the diffusion rate depends on the presence of the exchangeable tag.

Sample	Exchangeable CL	Exchangeable tag	$D \times 10^{-12} [\frac{\text{m}^2}{\text{s}}]$	$f$
PD1	✓	✓	2.5	0.02
PD2	✗	✓	3.1	0.01
PD3	✗	✗	< 0.01	N/A

Table 7.2: Initial self-diffusion coefficients at  $60^\circ\text{C}$  of NMR visible tags in PDMS backbone vitrimers.

$T_1$  and  $T_2$  measurements were taken at different temperatures to determine whether molecular dynamics can shed some light regarding the mechanism of action. They are presented in Fig. 7.10. The changes in relaxation time with temperature follow the expected

dynamics of a polymer chain above its  $T_g$ , as they show a linear relation between relaxation times and temperature. This indicates that there is no major change in the dynamics that occur in the polymer in this range of temperatures.

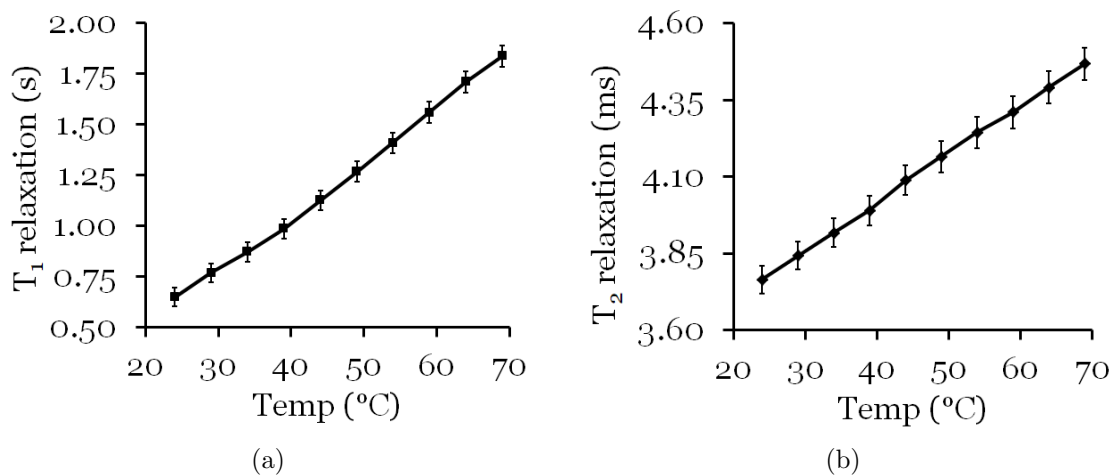


Figure 7.10: Relaxation times of sample PD1 vs temperature. (a) Spin-lattice relaxation times ( $T_1$ ) as measured using an inversion-recovery pulse sequence. (b) Spin-spin relaxation times ( $T_2$ ) as measured using a spin-echo pulse sequence. Both graphs show a quasi-linear relation between temperature and relaxation times, as expected from a polymer chain above  $T_g$ .

As the exchange reaction evidently decays as samples are annealed, more investigation was necessary to find its triggering mechanism. In a vinylogous urethane exchange reaction, the total number of bonds in the system does not change, therefore the system's potential energy remains the same. Unless an external potential drives it (compression or internal strain), the enthalpy,  $\Delta H$ , of this exchange reaction is expected to be zero and therefore cannot be the driving force. Rovigatti *et al.* compare this system's dynamics to "a stroll on the flat ground state potential energy surface" [165]. The only remaining driving force is entropy, as the system explores the enthalpy equivalent states, it will maximize its entropy by allowing each of the covalent bonds to be surrounded by as many possible sites for an exchange reaction. One of the early tests, done by the Wolf group, of these materials

### 7.3. Results and Discussion

found qualitatively that fluorescent dye soaked to one edge of the material seemed to migrate approximately one mm per 5 hours, indicating a diffusion coefficient in the order of  $10^{-10} \frac{\text{m}^2}{\text{s}}$ . This thought process and the qualitative data drove us to repeat the diffusion experiments using a sample with a driving force in the form of a chemical potential gradient. A heterogeneously loaded sample with tags being unevenly loaded in the polymer will have a gradient of concentration that may trigger the exchange reaction. This chemical potential gradient was expected to drive the system to a measurable self-diffusion of the tag in its attempt to increase entropy and reach a lower energy state. Results of this experiment can be seen in Table 7.3.

Time under heat [hours]	$D \times 10^{-12} [\frac{\text{m}^2}{\text{s}}]$	$f$
0	< 0.01	N/A
2	1.5	0.23
4	2.5	0.18
6	< 0.01	N/A
8	< 0.01	N/A
10	< 0.01	N/A
12	< 0.01	N/A

Table 7.3: Self-diffusion coefficients of heterogeneously loaded vitrimer sample at 60 °C vs. time. The first measurement (time 0) was measured before the heater was turned on as a control.

The results show again that diffusion decays over the course of several hours under isothermal annealing, to the point of no measurable diffusion. The induced diffusion was small, but still measurable, until it decayed entirely after six hours of exposure to heat. When the sample was removed from the NMR, it looked visibly very similar to the sample in its original state. No significantly visible diffusion of the coloured tag had occurred and the sample still had a very visible colour gradient and therefore still had a chemical potential gradient. It seems that chemical potential gradient is not enough to overcome

the energy barrier involved in creating the tetrahedral transition state that is required for the exchange process (see Scheme 7.2).

In an attempt to create other scenarios to produce the exchange process, a stress relaxation mechanism in polymers was considered. In general, amorphous polymers heated above their  $T_g$  can have individual chains diffuse and flow in a similar way to a viscous liquid [166]. This means that any deformation or stress from applied force is relaxed through the rearrangement of the polymer chains, similar to how a liquid responds to mechanical changes by breaking and creating intermolecular associations [167, 168]. Polymers containing small-molecule penetrants can exhibit self-diffusion of the penetrant on the same order of magnitude as was measured here. This diffusion behaves as a stress relieving mechanism by creating different local penetrant concentrations in different areas of the polymer, affecting the swelling and local mechanical properties of certain sections of the polymer [169, 164]. It is possible that the exchange mechanism is enabled by an effect called ‘stress dependant thermal activation’, which uses the exchange to reduce stress in the sample [170, 171]. This diffusion is dependant primarily on penetrant size, as the interactions between the polymer and the penetrants are weak. These interactions are similar to solute solvent interactions, and therefore present a size dependency for diffusion that resembles the Stokes-Einstein equation (Eq. 1.5).

We suggest that crosslinked vitrimers present covalent bond diffusion only when the sample is under mechanical stress. When the system is not in mechanical equilibrium, its initial state is higher in free energy and therefore the energy barrier for the exchange reaction is smaller and hence can be thermally overcome.

To test this hypothesis, three subsequent measurements of the same sample were carried out, in four different mechanical conditions. The steps are portrayed in Fig. 7.11 to simplify the explanation of the process, and the numerical results are summarized in Table 7.4.

Sample PD1c was made according to the exact same procedure as PD1a, cut to size, and packed in a sealed NMR tube. The sample in this state has residual mechanical stress as a result of post-polymerization cooling [172]. This stress is portrayed in Fig. 7.11b as bent lines which represent mechanical stress. The sample was then heated to 60 °C and resulted in a measurable self-diffusion coefficient of  $3.3 \cdot 10^{-12} \frac{\text{m}^2}{\text{s}}$  (see Table 7.4). The sample was held at 60 °C overnight, after which no self-diffusion was measured. We suggest that the time spent at 60 °C allowed the sample to go to a lower energy state via covalent bond diffusion we measured in the previous step. This mechanically relaxed state is represented in Fig. 7.11c as straight lines.

The sample was then removed from the NMR tube and mechanically cut and compressed to introduce mechanical stress to the sample. This step is portrayed in Fig. 7.5d and 7.5e as well as shown in a picture in Fig. 7.12. The temperature was once again increased to 60 °C and measurements of the compressed sample showed an initial diffusion coefficient of  $1.5 \cdot 10^{-12} \frac{\text{m}^2}{\text{s}}$ . This measured diffusion decayed after about six hours of exposure to 60 °C. This disappearance and reappearance of self-diffusion in response to physical manipulation of the sample demonstrated that the diffusion in the sample could be stimulated by the application of mechanical stress.

We propose that in both the original sample and the compressed sample, stress was present from either post-polymerization cooling of the sample or from the active compressing. The diffusing fraction of the sample is the fraction experiencing mechanical stress. Based on the regenerated diffusion after an external stress application and the lack of diffusion after the sample was allowed to return to equilibrium, it appears that the presence of mechanical stress in the sample is the key criterion needed for the exchange to occur spontaneously in the polymer.

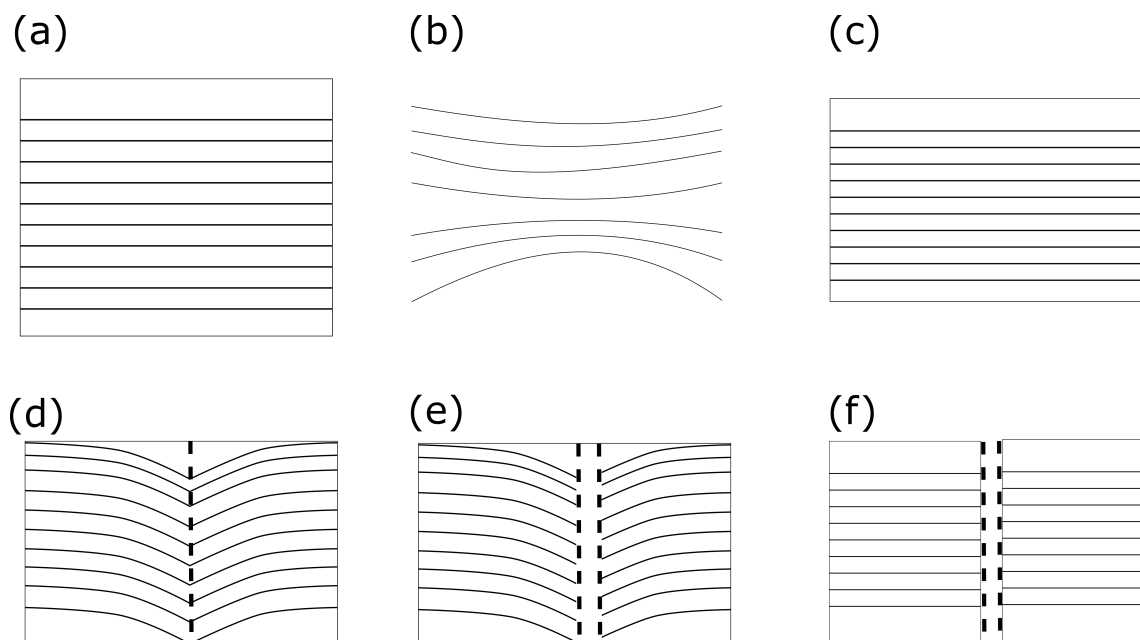


Figure 7.11: Explanation of the mechanical stress in the sample (a) when cast (b) post polymerization and cooling (c) after heating (d) when cut (e) cut and compressed (f) after heating. Bent lines represent the existence of mechanical stress and straight lines the lack of.

Sample's physical state	$D \times 10^{-12} [\frac{\text{m}^2}{\text{s}}]$	$f$	corresponds to Fig.:
Cut from original polymer cast	3.5	0.78	7.5b
Kept at temperature overnight	< 0.01	N/A	7.5c
Ground and compressed manually	1.5	0.88	7.5e
Kept at temperature for 6 hours	< 0.01	N/A	7.5f

Table 7.4: Self-diffusion coefficients at 60 °C of vitrimer sample PD1c with different states of mechanical stress. The measurements were taken in the order presented on the same sample.

Since the diffusion coefficients measured are similar to those of small molecules in dense polymers [173], another potential mechanism should be considered. It is possible that the



Figure 7.12: Sample PG1 (a) as originally packed in a sealed NMR tube and (b) after being opened and manually cut and compressed to introduce mechanical stress.

self-diffusion measured is that of tag molecules released in response to mechanical stress by a mechano-chemical process [174, 175]. These released molecules diffuse before attaching again to the polymer network, reforming the crosslinked polymer in its new configuration. The fact that no self-diffusion was observed when the polymer was crosslinked with a non-exchangeable crosslinker (see Table 7.2) does make this mechanism less likely. However, additional control experiments would be beneficial to our understanding of the mechanism behind this diffusion regeneration.

There is an interesting parallel with the piezoionic materials investigated in chapter 5. In both systems, mechanical stimulus leads to diffusion. There, a mechanical deformation creates a non-equilibrium ion distribution, giving rise to gradually diminishing ionic motion and an associated voltage. Here, built-in mechanical strain is gradually relieved by covalent rearrangement of crosslinkers. Similarly, equilibrium self-diffusion does not predict the stimulus response in either system.

## 7.4 Conclusions

The investigated vinylogous urethane exchange reaction in a crosslinked polymer network was observed using  $^{19}\text{F}$  PFG-NMR. These measurements have shown that these tags, which are stationary at room temperature, diffuse for a short period but abruptly stop after being exposed to heat for a few hours. Further heating and the creation of a chemical potential gradient do not appear to result in increased diffusion. Diffusion was only regenerated by application of mechanical stress. We therefore propose that the exchange reaction is a result of a thermally activated stress relaxation mechanism and is initiated by mechanical stress in addition to heat which is required to overcome the energy barrier. Further control experiments are necessary to eliminate other possible mechanisms that can potentially explain this observed behaviour. This suggested mechanism introduces opportunities for recycling materials made of vitrimers and also shows the physical limitations of using such materials under physical load in combination with heat.

## Chapter 8

# Conclusions and Future Work

### 8.1 Conclusions

In this dissertation, transport properties were investigated in a variety of systems in order to increase our understanding of the effects transport have on reaction rates, conductivities, and mechanical behaviour observed in innovative materials. We have used both existing and newly developed NMR methods to directly measure both driven and self-diffusion *in-situ* while investigating the effects concentration and environment have on them. By measuring both driven and self-diffusion in a variety of materials using nuclear magnetic resonance, we explain some of the transport mechanisms that are behind unique material behaviour.

To shed light on the piezoionic behaviour of devices made from EMI-TFSI dilution in PC, self-diffusion measurements were performed on RTIL ions in solutions and IPNs. The inversion observed in self-diffusion was similar to that seen in piezoionic behaviour providing experimental evidence for a previously suggested mechanism. This work helps clarify the ambiguities on the origin of the piezoionic effect and confirms that it is a result of differences in diffusivity of oppositely charged ions. The differences observed between directly measured conductivities and those derived by the Nernst-Einstein relation from self-diffusion suggest that the size and composition of ionic aggregates depend on RTIL concentration and that these aggregated species greatly affect the charge carrying abilities

of the ions.

A simple, low cost, eNMR probe was developed in order to directly measure the electrophoretic mobility of magnetically visible ions. Using this probe in conjunction with PFG-NMR measurements allowed us to investigate the unique behaviour of artificial muscle and nerve piezoionic materials. From these measurements, we conclude that in low concentrations the majority of the current is carried by the anion and in high concentrations,  $\text{Li}^+$  becomes the dominant carrier. This inversion contradicts the predictions of the Nernst-Einstein equation. We suggest a new conduction mechanism for  $\text{Li}^+$  that relies on supramolecular structures formed by the ions and the solvent. The relatively small  $\text{Li}^+$  ion can hop between vacant sites in these structures avoiding the hindering effects of a crowded, viscous solution. A similar conduction model has been computationally derived by Gao *et al.* [4], providing more support for the existence and importance of this conduction mechanism in concentrated solutions. By hopping between vacant sites in the concentrated solution,  $\text{Li}^+$  can conduct charge better than its diffusivity suggests, changing our understanding of the relation between diffusion and ionic conductivity.

The self-diffusion coefficients of four chromophores were measured in operating conditions of optical filters used in the automotive industry. The measurements were done in a vast variety of formulations and physical states in order to optimize both the feasibility of the measurements and provide experimental data to assist in formulation decisions of future devices. The dynamics of chromophore molecules were investigated as well as the relation between chromophore diffusion and temperature. A general decrease in self-diffusion with temperature decrease was observed. Yet, at 250 K the diffusion of the chromophore showed a non-Fickian behaviour and increases as the temperature decreases. This is likely a result of some components precipitating out of solution resulting in a reduction of the total viscosity of the solution. The information provided by these measurements has provided

experimental data that assists in the determination of device formulations. This research helps improve the usability of these optical filters and increase fuel economy by reducing the need for active cooling or heating in automobiles.

A vinylogous urethane exchange reaction in vitrimers was investigated using PFG-NMR. In these samples, no diffusion was observed after the initial heating of the samples. Only when physical stress was introduced, diffusion regenerated. From these measurements, we propose a thermally activated stress relaxation mechanism which is initiated by mechanical stress. This work changed what we know about vitrimers recycling by showing the necessary conditions to initiate the crosslinker exchange reaction. We learn the physical limitation for usage of these vitrimers as they cannot be used in temperatures higher than 60 °C while under physical load, as that will initiate the crosslinker exchange, forcing them to re-shape. In addition, this suggested mechanism introduces recycling opportunities for materials made of vitrimers under the same conditions. This research has shown both the limitations and the recycling opportunities for these materials.

The investigation of these systems has demonstrated that transport is a key component in their unique behaviours. This research changed what we know about these systems and proved, again, that classical description does not provide accurate predictions for transport in dense material. The new mechanisms suggested in this dissertation have shown that, in concentrated media, diffusivity does not follow the same mechanism as in diluted solutions. The suggested mechanisms provide a different mental images that explains the experimental evidence. From this work, it is clear to see that experimental data measured *in-situ* is necessary to guide the development of innovative materials. With our new, simple, low-cost eNMR probe future scientists can continue and explore the diffusivity and conduction of dense materials.

Although the research done in this dissertation has answered some questions, new

questions are also raised. Further research is still necessary for the complete investigation of transport properties in dense media. The methods used in this dissertation have been tested and refined so that future researchers can utilize them, and continue the work and expand it to further materials and types of media.

## **8.2 Recommended Future Work**

### **8.2.1 eNMR Probe Construction and Validation**

The newly constructed eNMR probe was proven successful in directly measuring electrophoretic mobility coefficients for solution samples of both low and high conductivities and concentrations. Further validation work should be done on a variety of salts, comparing the mobilities measured to known conductivities. In addition, more experiments should be done using the existing eNMR probe on samples based on polymers in order to investigate the conduction mechanisms in polymer based materials. Our attempts to make eNMR measurements in polymers were not successful; we believe this was due to high resistance of the solvent-polymer interface, which may be reduced by increasing the contact area between the electrode and the polymer. This can be done by either finning the polymer to increase the surface area of contact with the solution or by connecting the electrode directly to the polymer sample. If necessary,  $T_2$  times of the mobile species might be increased by employing a deuterated solvent which would reduce the intermolecular contribution of the probe nucleus' relaxation.

### **8.2.2 Diffusion of EMI-TFSI Dilutions in Propylene Carbonate**

The self-diffusion measurements of EMI-TFSI dilutions have been successfully measured and answered some of the question regarding the piezoionic effect seen in devices made

of these IEAPs. In order to fully investigate the transport mechanism and conductivity attenuating interactions, ionic mobility constants should be measured directly for the existing set of liquid samples, using the eNMR set-up that is described in Chapter 3. With further adjustment of the existing eNMR pulse sequences and sample holder, we believe it will be possible to measure mobility for the set of IPN embedded electrolytes as well.

By obtaining the effective charge ( $z_{\text{eff}}$ ) for the individual ions from the combination of eNMR and PFG-NMR insight on the aggregation of RTILs as a function of dilution would be gained. This will provide a more direct explanation of the observed phenomena in addition to providing us with a better understanding of conduction in ion dense solutions. By measuring the mobility for samples with different solvents and polymer compositions we will be able to achieve better understanding of ion-solvent and ion-polymer interactions, expanding our understanding of transport in ion dense media. This will make it possible to better design future electrochemical devices with specific transport properties.

### 8.2.3 Ion Transport in Touch Sensor Electrolytes

Both self-diffusion and electrophoretic mobility have been measured for a set of different concentration LiTFSI salt solutions in PC that exhibit the piezionic effect. The data showed that for lithium, the effective charge,  $z_{\text{eff}}$ , increases with an increase in concentration. Together with self-diffusion data, we suggest a potential  $\text{Li}^+$  conduction mechanism that explains the interesting behaviour of the ions in high concentrations. The mechanism is based on  $\text{Li}^+$  hopping between holes, created by an external application of voltage. In order to confirm the suggested  $\text{Li}^+$  conduction mechanism, more experiments should be done at elevated temperature. Increasing the sample's temperature should decrease the ion-ion aggregates necessary for conduction via this suggested mechanism. This mechanism can be further validated if indeed  $\text{Li}^+$ 's mobility matches that predicted by the

Nernst-Einstein relation at elevated temperature. Additionally, proximity measurements may help confirm the existence of ionic aggregates in solutions and learn of their structure. Using the nuclear Overhauser effect (NOE) may assist in learning the proximity between the anion and solvent and revealing the ratio between them to create the necessary supra-molecular structure. Raman spectroscopy might help provide experimental evidence of the supra-molecular structures and their composition in solution (as done for solvation layer measurements of  $\text{Li}^+$  by Shi *et al.* [125]). Molecular dynamics simulations can provide helpful insight (as shown by Gao *et al.* [4]) and assist in learning the minimal conditions necessary for the existence of this conduction mechanism.

These experiments should be expanded to more lithium salts, especially those containing a differently sized counterion. It would be interesting to see what is the minimal ion size difference ratio necessary for the depletion conduction mechanism to occur.

### 8.2.4 Chromophore Diffusion in Optical Filter Devices

In order to fully examine the effect of an electric field, more eNMR experiments are needed. To confirm that the transport of the chromophores occurs as we suspect, transport measurements of the only magnetically visible ion in the sample,  $\text{TFSI}^-$ , could be performed. By comparing the measured mobility to relative device fading time, the effect an applied electric field has on chromophore diffusion can be examined.

The time it takes for the charge to accumulate at the electrodes, shielding the electric field on the sample can be measured using a constant-time eNMR pulse sequence. In this pulse sequence, the total duration of the experiment is fixed, but the time during which the electric field is applied,  $\tau$ , can be modified to measure the time migration constant,  $\tau_{\text{eq}}$  (the time constant for charge accumulation near the electrodes that results in electric field shielding). Currently, devices are operated by switching the direction of the electric field

at a specific frequency to avoid this charge accumulation at the electrodes. By comparing  $\tau_{\text{eq}}$  to the switching time, the transport mechanism of the chromophore molecules could be more fully understood. In the case where  $\tau_{\text{eq}}$  is shorter than the switching time used in the operation of these devices, the switching time should be reduced. If after such a reduction, no measurable difference in fading time device is detected, it would be possible to conclude that the diffusion of the chromophore molecules is not affected by the application of an electric field.

### 8.2.5 Vitrimers - Transport of Thermally Exchangeable Molecules

In this project, we have successfully confirmed that NMR measured diffusion is triggered when the sample is physically manipulated, but diffusion shuts down after initial stress is relieved. Some questions still remain unanswered in regards to the type of stress that triggers the diffusion.

First, to confirm the effects seen with NMR, rheological studies are required. These measurements are currently in progress with the help of Tanya Tomkovic of Savvas Hatzikiriakos' group in Chemical and Biological Engineering of UBC.

To test the possible free crosslinker molecule explanation, a control experiment could be done. An NMR visible penetrant molecule of similar size and polarity to the used crosslinkers should be introduced to the system, but with no ability to bond to the network. If the measured diffusion of such molecule is similar to that measured in our experiments, the conclusions reached should be reconsidered, as it is possible the original measurements have only observed the crosslinker molecules in a temporary state, when they are disconnected from the polymer network.

An NMR stress applicator can be used to attempt and trigger the diffusion *in-situ*. An existing set-up already exists in the lab and could easily be adapted to this purpose. In order

to combine the stress applicator with self-diffusion measurements, the stress applicator requires some adjustments to physically fit in the magnetic field gradient set. Once this set-up is adjusted to fit in the gradient set, it will be possible to apply different types of physical stress on the sample in different temperatures and measure diffusion immediately after. It will be very interesting to see which types of loading scenario trigger the diffusion and which do not. In addition, it will be interesting to see whether applying the stress at high temperature does or does not trigger the diffusion.

## 8.3 Outlook

The investigations presented in this dissertation demonstrated the importance of transport to our understanding of material behaviour and lay the ground work for future research utilizing NMR methodology. The mechanisms suggested from this work show that diffusivity in concentrated media follows unique mechanisms that are not present in diluted solutions. Future NMR based research on additional salts and RTILs can help progress the innovation of new materials with applications such as batteries, artificial muscles and nerves, and recyclable polymers, to list just a few possibilities. The eNMR probe system presented here has demonstrated that accurate ionic conductivity of NMR visible ions can be measured directly, using a relatively simple, cost-effective, and easily manufactured device. By measuring diffusive parameters *in-situ*, the mechanisms underlying novel material properties can be explored in order to advance material science and technology.

# Bibliography

- [1] C. H. Tso, “NMR study of  $\text{PF}_6^-$  doped polypyrrole: a potential candidate for artificial muscles,” MSc, The University of British Columbia, 2010.
- [2] A. L. Michal, “Nuclear magnetic resonance characterization of solid polymer electrolyte materials,” MASc, The University of British Columbia, 2012.
- [3] V. Woehling, G. T. M. Nguyen, C. Plesse, Y. Petel, Y. Dobashi, J. D. W. Madden, C. A. Michal, and F. Vidal, “Study of the piezoionic effect and influence of electrolyte in conducting polymer based soft strain sensors,” *Multifunctional Materials*, vol. 2, p. 045002, Dec. 2019.
- [4] Y. Gao, J. Huang, Y. Liu, J. Yan, B. Mao, and S. Chen, “Ion-vacancy coupled charge transfer model for ion transport in concentrated solutions,” *Science China Chemistry*, vol. 62, pp. 515 – 520, Apr. 2019.
- [5] T. Wright, T. Tomkovic, S. G. Hatzikiriakos, and M. O. Wolf, “Photoactivated healable vitrimeric copolymers,” *Macromolecules*, vol. 52, no. 1, pp. 36 – 42, 2019.
- [6] A. Einstein, “On the theory of the Brownian movement,” *Ann. Phys.*, vol. 19, no. 4, pp. 371 – 381, 1906.
- [7] A. Fick, “Ueber diffusion,” *Annalen der Physik*, vol. 170, no. 1, pp. 59 – 86, 1855.

- [8] M. Sharma and S. Yashonath, "Size dependence of solute diffusivity and Stokes-Einstein relationship: effect of van der Waals interaction," *Diffusion Fundamentals*, vol. 6, pp. 35 – 41, 2007.
- [9] G. Peskir, "On the diffusion coefficient: The Einstein relation and beyond," *Stochastic Models*, vol. 19, no. 3, pp. 383 – 405, 2003.
- [10] J. T. Edward, "Molecular volumes and the Stokes-Einstein equation," *Journal of Chemical Education*, vol. 47, no. 4, p. 261, 1970.
- [11] J. Rauch and W. Köhler, "Collective and thermal diffusion in dilute, semidilute, and concentrated solutions of polystyrene in toluene," *The Journal of Chemical Physics*, vol. 119, no. 22, pp. 11977 – 11988, 2003.
- [12] J. L. Anderson, F. Rauh, and A. Morales, "Particle diffusion as a function of concentration and ionic strength," *The Journal of Physical Chemistry*, vol. 82, no. 5, pp. 608 – 616, 1978.
- [13] B. Jachimska, M. Wasilewska, and Z. Adamczyk, "Characterization of globular protein solutions by dynamic light scattering, electrophoretic mobility, and viscosity measurements," *Langmuir*, vol. 24, no. 13, pp. 6866 – 6872, 2008.
- [14] Z. Németh, L. Erdei, and A. Kolics, "A new approach to studying ion transport in corrosion protective coatings using an *in situ* radiotracer method," *Corrosion Science*, vol. 37, no. 7, pp. 1163 – 1166, 1995.
- [15] T. Welton, "Room-temperature ionic liquids: solvents for synthesis and catalysis," *Chemical Reviews*, vol. 99, no. 8, pp. 2071 – 2084, 1999.

- [16] E. T. Fox, E. Paillard, O. Borodin, and W. A. Henderson, “Physicochemical properties of binary ionic liquid-aprotic solvent electrolyte mixtures,” *The Journal of Physical Chemistry C*, vol. 117, no. 1, pp. 78 – 84, 2013.
- [17] K. Yuyama, G. Masuda, H. Yoshida, and T. Sato, “Ionic liquids containing the tetrafluoroborate anion have the best performance and stability for electric double layer capacitor applications,” *Journal of Power Sources*, vol. 162, no. 2, pp. 1401 – 1408, 2006.
- [18] R. D. Rogers, “Materials science: Reflections on ionic liquids,” *Nature*, vol. 447, no. 7147, pp. 917 – 918, 2007.
- [19] H. Weingärtner, P. Sasisanker, C. Daguinet, P. J. Dyson, I. Krossing, J. M. Slattery, and T. Schubert, “The dielectric response of room-temperature ionic liquids: Effect of cation variation,” *The Journal of Physical Chemistry B*, vol. 111, no. 18, pp. 4775 – 4780, 2007.
- [20] K. Ueno, H. Tokuda, and M. Watanabe, “Ionicity in ionic liquids: correlation with ionic structure and physicochemical properties,” *Physical Chemistry Chemical Physics*, vol. 12, pp. 1649 – 1658, 2010.
- [21] H. Tokuda, S. Tsuzuki, M. A. B. H. Susan, K. Hayamizu, and M. Watanabe, “How ionic are room-temperature ionic liquids? an indicator of the physicochemical properties,” *The Journal of Physical Chemistry B*, vol. 110, no. 39, pp. 19593 – 19600, 2006.
- [22] J. Dupont, “On the solid, liquid and solution structural organization of imidazolium ionic liquids,” *Journal of the Brazilian Chemical Society*, vol. 15, pp. 341 – 350, June 2004.

- [23] R. W. Jones and F. Mohling, "Accuracy of theories of the primitive model of ionic solutions," *The Journal of Physical Chemistry*, vol. 75, no. 25, pp. 3790 – 3796, 1971.
- [24] H. L. Friedman, *Ionic Solution Theory: based on Cluster expansion methods*, vol. 3. Interscience Publishers, 1962.
- [25] R. Robinson and R. Stokes, *Electrolyte Solutions*. Dover Publications, 2nd revised ed., 1951 (2002).
- [26] V. Gutmann, "Empirical parameters for donor and acceptor properties of solvents," *Electrochimica Acta*, vol. 21, pp. 661 – 670, 1976.
- [27] R. M. Adar, T. Markovich, and D. Andelman, "Bjerrum pairs in ionic solutions: A Poisson-Boltzmann approach," *The Journal of Chemical Physics*, vol. 146, no. 19, p. 194904, 2017.
- [28] Y. Marcus and G. Hefter, "Ion pairing," *Chemical Reviews*, vol. 106, no. 11, pp. 4585 – 4621, 2006.
- [29] J. Lacour and D. Moraleda, "Chiral anion-mediated asymmetric ion pairing chemistry," *Chem. Commun.*, pp. 7073 – 7089, 2009.
- [30] P. V. Wright, "Electrical conductivity in ionic complexes of poly(ethylene oxide)," *British Polymer Journal*, vol. 7, no. 5, pp. 319 – 327, 1975.
- [31] M. Armand, "Polymer solid electrolytes - an overview," *Solid State Ionics*, vol. 910, Part 2, pp. 745 – 754, 1983.
- [32] G. Ehrenstein and R. Theriault, *Polymeric Materials: Structure, Properties, Applications*. Hanser, 2001.

- [33] S. Lankalapalli and V. M. Kolapalli, "Polyelectrolyte complexes: a review of their applicability in drug delivery technology," *Indian Journal of Pharmaceutical Sciences*, vol. 71, no. 5, pp. 481 – 487, 2009.
- [34] Y. Roichman, *Charge Transport in Conjugated Polymers*. PhD, Technion - Israel Institute of Technology, 2004.
- [35] A. D. McNaught and A. W. Blackwell, *Compendium of Chemical Terminology*. Scientific Publications, 2nd ed., 1997.
- [36] R. P. Feynman, R. B. Leighton, and M. L. Sands, *The Feynman Lectures on Physics*, vol. 1. Addison-Wesley Pub. Co, 1963.
- [37] W. S. Price, *NMR Studies of Translational Motion: Principles and Applications*. Cambridge University Press, 2009.
- [38] B. Amsden, "Solute diffusion within hydrogels. Mechanisms and models," *Macromolecules*, vol. 31, no. 23, pp. 8382 – 8395, 1998.
- [39] L. Masaro and X. Zhu, "Physical models of diffusion for polymer solutions, gels and solids," *Progress in Polymer Science*, vol. 24, no. 5, pp. 731 – 775, 1999.
- [40] L. Johansson, C. Elvingson, and J. E. Löfroth, "Diffusion and interaction in gels and solutions. 3. Theoretical results on the obstruction effect," *Macromolecules*, vol. 24, no. 22, pp. 6024 – 6029, 1991.
- [41] L. Johansson and J. Löfroth, "Diffusion and interaction in gels and solutions. 4. Hard sphere Brownian dynamics simulations," *The Journal of Chemical Physics*, vol. 98, no. 9, pp. 7471 – 7479, 1993.

- [42] M. Golmohamadi and K. J. Wilkinson, "Diffusion of ions in a calcium alginate hydrogel-structure is the primary factor controlling diffusion," *Carbohydrate Polymers*, vol. 94, no. 1, pp. 82 – 87, 2013.
- [43] M. H. Rausch, L. Hopf, A. Heller, A. Leipertz, and A. P. Fröba, "Binary diffusion coefficients for mixtures of ionic liquids [EMIM][N(CN)<sub>2</sub>], [EMIM][NTf<sub>2</sub>], and [HMIM][NTf<sub>2</sub>] with acetone and ethanol by dynamic light scattering (DLS)," *The Journal of Physical Chemistry B*, vol. 117, no. 8, pp. 2429 – 2437, 2013.
- [44] S. M. Patil, D. A. Keire, and K. Chen, "Comparison of NMR and dynamic light scattering for measuring diffusion coefficients of formulated insulin: Implications for particle size distribution measurements in drug products," *The AAPS Journal*, vol. 19, pp. 1760 – 1766, Nov. 2017.
- [45] M. Holz, "Field-assisted diffusion studied by electrophoretic NMR," in *Diffusion in Condensed Matter* (P. Heitjans and J. Kärger, eds.), ch. 17, pp. 717 – 742, Berlin Heidelberg: Springer-Verlag, 2005.
- [46] G. E. Murch, "The haven ratio in fast ionic conductors," *Solid State Ionics*, vol. 7, no. 3, pp. 177 – 198, 1982.
- [47] N. A. Stolwijk, J. Kösters, M. Wiencierz, and M. Schönhoff, "On the extraction of ion association data and transference numbers from ionic diffusivity and conductivity data in polymer electrolytes," *Electrochimica Acta*, vol. 102, pp. 451 – 458, 2013.
- [48] A. R. Cooper, "The haven ratio in terms of the self-diffusion of charge," in *Transport in Nonstoichiometric Compounds* (G. Simkovich and V. S. Stubican, eds.), pp. 127 – 137, Boston, MA: Springer US, 1985.

- [49] J. E. Bostwick, C. J. Zanelotti, C. Iacob, A. G. Korovich, L. A. Madsen, and R. H. Colby, "Ion transport and mechanical properties of non-crystallizable molecular ionic composite electrolytes," *Macromolecules*, vol. 53, no. 4, pp. 1405 – 1414, 2020.
- [50] A. W. Adamson, "Chapter four - chemical thermodynamics. The first law of thermodynamics," in *A Textbook of Physical Chemistry*, pp. 101 – 144, Academic Press, 2nd ed., 1979.
- [51] H. Okuzaki, S. Takagi, F. Hishiki, and R. Tanigawa, "Ionic liquid/polyurethane/PEDOT:PSS composites for electro-active polymer actuators," *Sensors and Actuators B: Chemical*, vol. 194, pp. 59 – 63, 2014.
- [52] J. Vatamanu, Z. Hu, D. Bedrov, C. Perez, and Y. Gogotsi, "Increasing energy storage in electrochemical capacitors with ionic liquid electrolytes and nanostructured carbon electrodes," *The Journal of Physical Chemistry Letters*, vol. 4, no. 17, pp. 2829 – 2837, 2013.
- [53] T. Sato, G. Masuda, and K. Takagi, "Electrochemical properties of novel ionic liquids for electric double layer capacitor applications," *Electrochimica Acta*, vol. 49, no. 21, pp. 3603 – 3611, 2004.
- [54] P. G. Bruce and C. A. Vincent, "Effect of ion association on transport in polymer electrolytes," *Faraday Discussions of the Chemical Society*, vol. 88, pp. 43 – 54, 1989.
- [55] H. Fritz and A. Kuhn, "Comparative determination of effective transport numbers in solid lithium electrolytes," *Journal of Power Sources*, vol. 41, no. 3, pp. 253 – 261, 1993.
- [56] A. Noda, K. Hayamizu, and M. Watanabe, "Pulsed-gradient spin echo  $^1\text{H}$  and  $^{19}\text{F}$  NMR ionic diffusion coefficient, viscosity, and ionic conductivity of non-

- chloroaluminate room-temperature ionic liquids,” *The Journal of Physical Chemistry B*, vol. 105, no. 20, pp. 4603 – 4610, 2001.
- [57] J. Hou, Z. Zhang, and L. A. Madsen, “Cation/anion associations in ionic liquids modulated by hydration and ionic medium,” *The Journal of Physical Chemistry B*, vol. 115, no. 16, pp. 4576 – 4582, 2011.
- [58] Z. Zhang and L. A. Madsen, “Observation of separate cation and anion electrophoretic mobilities in pure ionic liquids,” *The Journal of Chemical Physics*, vol. 140, no. 8, 2014.
- [59] H. Tokuda, K. Hayamizu, K. Ishii, M. A. B. H. Susan, and M. Watanabe, “Physicochemical properties and structures of room temperature ionic liquids. 2. Variation of alkyl chain length in imidazolium cation,” *The Journal of Physical Chemistry B*, vol. 109, no. 13, pp. 6103 – 6110, 2005.
- [60] M. H. Levitt, *Spin Dynamics: Basics of Nuclear Magnetic Resonance*. Wiley, 2nd ed., 2008.
- [61] E. O. Stejskal and J. E. Tanner, “Spin diffusion measurements: spin echoes in the presence of a time-dependent field gradient,” *The Journal of Chemical Physics*, vol. 42, no. 1, pp. 288 – 292, 1965.
- [62] T. R. Saarinen and C. S. Johnson, “Imaging of transient magnetization gratings in NMR analogies with laser-induced gratings and applications to diffusion and flow,” *Journal of Magnetic Resonance*, vol. 78, no. 2, pp. 257 – 270, 1988.
- [63] I. Solomon, “Relaxation processes in a system of two spins,” *Physical Review*, vol. 99, pp. 559 – 565, July 1955.

- [64] K. J. Packer, "The study of slow coherent molecular motion by pulsed nuclear magnetic resonance," *Molecular Physics*, vol. 17, no. 4, pp. 355 – 368, 1969.
- [65] M. Holz and C. Müller, "Direct measurement of single ionic drift velocities in electrolyte solutions. an nmr method," *Berichte der Bunsengesellschaft für physikalische Chemie*, vol. 86, no. 2, pp. 141 – 147, 1982.
- [66] M. Holz, "Electrophoretic NMR," *Chemical Society Reviews*, vol. 23, no. 3, pp. 165 – 174, 1994.
- [67] *P&L Scientific I.S.*, 2013 (accessed February 1, 2015). <http://plscientific.se/>.
- [68] F. Hallberg, *Molecular Interactions Studied by Electrophoretic and Diffusion NMR*. PhD, KTH Royal Institute of Technology, 2010.
- [69] F. Hallberg, I. Furó, and P. Stilbs, "Ion pairing in ethanol/water solution probed by electrophoretic and diffusion NMR," *Journal of the American Chemical Society*, vol. 131, no. 39, pp. 13900 – 13901, 2009.
- [70] Q. He, Y. Liu, H. Sun, and E. Li, "Capillary array electrophoretic NMR of proteins in biological buffer solutions," *Journal of Magnetic Resonance*, vol. 141, no. 2, pp. 355 – 359, 1999.
- [71] T. R. Saarinen and C. S. Johnson, "High-resolution electrophoretic NMR," *Journal of the American Chemical Society*, vol. 110, no. 10, pp. 3332 – 3333, 1988.
- [72] U. Böhme and U. Scheler, "Hydrodynamic size and electrophoretic mobility of poly (styrene sulfonate) versus molecular weight," *Macromolecular Chemistry and Physics*, vol. 208, no. 19-20, pp. 2254 – 2257, 2007.

- [73] F. Hallberg, I. Furó, P. V. Yushmanov, and P. Stilbs, “Sensitive and robust electrophoretic NMR: Instrumentation and experiments,” *Journal of Magnetic Resonance*, vol. 192, no. 1, pp. 69 – 77, 2008.
- [74] I. Furó, “Association of molecules and ions as observed by electrokinetic and diffusion NMR.” <https://www.euract-nmr.kit.edu/downloads/Furo.pdf>, Jan. 2010.
- [75] E. Pettersson, I. Furó, and P. Stilbs, “On experimental aspects of electrophoretic NMR,” *Concepts in Magnetic Resonance Part A*, vol. 22, no. 2, pp. 61 – 68, 2004.
- [76] U. Böhme and U. Scheler, “Effective charge of poly(styrenesulfonate) and ionic strength in electrophoresis NMR investigation,” *Colloids and Surfaces A: Physicochemical and Engineering Aspects*, vol. 222, no. 1, pp. 35 – 40, 2003.
- [77] W. S. Price, F. Hallberg, and P. Stilbs, “A PGSE diffusion and electrophoretic NMR study of Cs<sup>+</sup> and Na<sup>+</sup> dynamics in aqueous crown ether systems,” *Magnetic Resonance in Chemistry*, vol. 45, no. 2, pp. 152 – 156, 2007.
- [78] M. Holz, O. Lucas, and C. Müller, “NMR in the presence of an electric current. Simultaneous measurements of ionic mobilities, transference numbers, and self-diffusion coefficients using an NMR pulsed-gradient experiment,” *Journal of Magnetic Resonance (1969)*, vol. 58, no. 2, pp. 294 – 305, 1984.
- [79] M. Gouverneur, J. Kopp, L. van Wüllen, and M. Schönhoff, “Direct determination of ionic transference numbers in ionic liquids by electrophoretic NMR,” *Phys. Chem. Chem. Phys.*, vol. 17, pp. 30680 – 30686, 2015.
- [80] U. Scheler, *Electrophoretic NMR*. \* Update based on original article by Charles S. Johnson, *Encyclopedia of Magnetic Resonance*, 1996, John Wiley & Sons Ltd. American Cancer Society, Mar. 2012.

- [81] B. Manz, P. Stilbs, B. Joensson, O. Soederman, and P. T. Callaghan, “NMR imaging of the time evolution of electroosmotic flow in a capillary,” *The Journal of Physical Chemistry*, vol. 99, no. 29, pp. 11297 – 11301, 1995.
- [82] L. Cser, G. Török, G. Krexner, M. Prem, and I. Sharkov, “Neutron holographic study of palladium hydride,” *Applied physics letters*, vol. 85, no. 7, pp. 1149 – 1151, 2004.
- [83] M. Vlach, J. Čížek, O. Melikhova, V. Kodetova, I. Stulíková, and I. Procházka, “Hydrogen trapping at defects in pd and thermally activated desorption,” *Defect and Diffusion Forum*, vol. 365, pp. 36 – 41, July 2015.
- [84] M. Moini, P. Cao, and A. J. Bard, “Hydroquinone as a buffer additive for suppression of bubbles formed by electrochemical oxidation of the CE buffer at the outlet electrode in capillary electrophoresis/electrospray ionization-mass spectrometry,” *Analytical Chemistry*, vol. 71, no. 8, pp. 1658 – 1661, 1999.
- [85] Q. He and Z. Wei, “Convection compensated electrophoretic NMR,” *Journal of Magnetic Resonance*, vol. 150, no. 2, pp. 126 – 131, 2001.
- [86] M. Bielejewski, M. Giesecke, and I. Furó, “On electrophoretic NMR. Exploring high conductivity samples,” *Journal of Magnetic Resonance*, vol. 243, pp. 17 – 24, 2014.
- [87] H. Y. Carr and E. M. Purcell, “Effects of diffusion on free precession in nuclear magnetic resonance experiments,” *Phys. Rev.*, vol. 94, pp. 630 – 638, May 1954.
- [88] S. Meiboom and D. Gill, “Modified spin-echo method for measuring nuclear relaxation times,” *Review of Scientific Instruments*, vol. 29, no. 8, pp. 688 – 691, 1958.
- [89] C. A. Michal, K. Broughton, and E. Hansen, “A high performance digital receiver for home-built nuclear magnetic resonance spectrometers,” *Review of Scientific Instruments*, vol. 73, pp. 453 – 458, 2002.

- [90] C. H. Tso, J. D. Madden, and C. A. Michal, “An NMR study of ions in polypyrrole,” *Synthetic Metals*, vol. 157, no. 1012, pp. 460 – 466, 2007.
- [91] C. Ammann, P. Meier, and A. E. Merbach, “A simple multinuclear NMR thermometer,” *Journal of Magnetic Resonance (1969)*, vol. 46, no. 2, pp. 319 – 21, 1982.
- [92] C. R. Cantor and P. Schimmel, *Biophysical Chemistry: Part II: Techniques for the study of biological structure and function*. W.H Freeman, 1980.
- [93] M. Schmuck and M. Z. Bazant, “Homogenization of the Poisson-Nernst-Planck equations for ion transport in charged porous media,” *SIAM Journal on Applied Mathematics*, vol. 75, no. 3, pp. 1369 – 1401, 2015.
- [94] P. Atkins, J. De Paula, and J. Keeler, *Atkins’ Physical Chemistry*. Oxford University Press, 2018.
- [95] M. Gouverneur, F. Schmidt, and M. Schönhoff, “Negative effective Li transference numbers in Li salt/ionic liquid mixtures: does Li drift in the “wrong” direction?,” *Phys. Chem. Chem. Phys.*, vol. 20, pp. 7470 – 7478, 2018.
- [96] M. J. Park, I. Choi, J. Hong, and O. Kim, “Polymer electrolytes integrated with ionic liquids for future electrochemical devices,” *Journal of Applied Polymer Science*, vol. 129, no. 5, pp. 2363 – 2376, 2013.
- [97] S. Z. Bisri, S. Shimizu, M. Nakano, and Y. Iwasa, “Endeavor of iontronics: From fundamentals to applications of ion-controlled electronics,” *Advanced Materials*, vol. 29, no. 25, pp. 1607054(1 – 48), 2017.
- [98] L. Chang, Y. Liu, Q. Yang, L. Yu, J. Liu, Z. Zhu, P. Lu, Y. Wu, and Y. Hu, “Ionic electroactive polymers used in bionic robots: A review,” *Journal of Bionic Engineering*, vol. 15, pp. 765 – 782, Sept. 2018.

- [99] Y. Liu, Y. Hu, J. Zhao, G. Wu, X. Tao, and W. Chen, "Self-powered piezoionic strain sensor toward the monitoring of human activities," *Small*, vol. 12, no. 36, pp. 5074 – 5080, 2016.
- [100] M. S. U. Sarwar, Y. Dobashi, E. F. Scabeni Glitz, M. Farajollahi, S. Mirabasi, S. Naficy, G. M. Spinks, and J. D. W. Madden, "Transparent and conformal 'PiezoIonic' touch sensor," *Proceedings of SPIE*, vol. 9430, pp. 943026 – 943029, 2015.
- [101] Y. Dobashi, G. Allegretto, M. S. Sarwar, E. Cretu, and J. D. Madden, "Mechanoionic transduction of solid polymer electrolytes and potential applications," *MRS Advances*, vol. 1, pp. 63 – 68, 2016.
- [102] Y. Dobashi, A. Fannir, M. Farajollahi, A. Mahmoudzadeh, A. Usgaocar, D. Yao, G. T. Nguyen, C. Plesse, F. Vidal, and J. D. Madden, "Ion transport in polymer composites with non-uniform distributions of electronic conductors," *Electrochimica Acta*, vol. 247, pp. 149 – 162, 2017.
- [103] J. Hunger, A. Stoppa, R. Buchner, and G. Hefter, "From ionic liquid to electrolyte solution: Dynamics of 1-*N*-butyl-3-*N*-methylimidazolium tetrafluoroborate/dichloromethane mixtures," *The Journal of Physical Chemistry B*, vol. 112, no. 41, pp. 12913 – 12919, 2008.
- [104] K. Fumino, V. Fossog, P. Stange, K. Wittler, W. Polet, R. Hempelmann, and R. Ludwig, "Ion pairing in protic ionic liquids probed by far-infrared spectroscopy: Effects of solvent polarity and temperature," *ChemPhysChem*, vol. 15, no. 12, pp. 2604 – 2609, 2014.

- [105] T. Vogl, S. Menne, and A. Balducci, “Mixtures of protic ionic liquids and propylene carbonate as advanced electrolytes for lithium-ion batteries,” *Physical Chemistry Chemical Physics*, vol. 16, pp. 25014 – 25023, 2014.
- [106] Y. Liu, S. Liu, J. Lin, D. Wang, V. Jain, R. Montazami, J. R. Heflin, J. Li, L. Madsen, and Q. M. Zhang, “Ion transport and storage of ionic liquids in ionic polymer conductor network composites,” *Applied Physics Letters*, vol. 96, no. 22, p. 223503, 2010.
- [107] W. Gorecki, M. Jeannin, E. Belorizky, C. Roux, and M. Armand, “Physical properties of solid polymer electrolyte PEO(LiTFSI) complexes,” *Journal of Physics: Condensed Matter*, vol. 7, pp. 6823 – 6832, Aug. 1995.
- [108] Q. Cao, X. Lu, X. Wu, Y. Guo, L. Xu, and W. Fang, “Density, viscosity, and conductivity of binary mixtures of the ionic liquid *N*-(2-hydroxyethyl)piperazinium propionate with water, methanol, or ethanol,” *Journal of Chemical & Engineering Data*, vol. 60, no. 3, pp. 455 – 463, 2015.
- [109] J. Xie, Z. Liang, and Y.-C. Lu, “Molecular crowding electrolytes for high-voltage aqueous batteries,” *Nature Materials*, Apr. 2020.
- [110] D. Coglitore, S. P. Edwardson, P. Macko, E. A. Patterson, and M. Whelan, “Transition from fractional to classical Stokes-Einstein behaviour in simple fluids,” *Royal Society Open Science*, vol. 4, no. 12, p. 170507, 2017.
- [111] K. Fujii, Y. Soejima, Y. Kyoshoin, S. Fukuda, R. Kanzaki, Y. Umebayashi, T. Yamaguchi, S. Ishiguro, and T. Takamuku, “Liquid structure of room-temperature ionic liquid, 1-ethyl-3-methylimidazolium bis-(trifluoromethanesulfonyl) imide,” *The Journal of Physical Chemistry B*, vol. 112, no. 14, pp. 4329 – 4336, 2008.

- [112] W. M. Haynes, *CRC Handbook of Chemistry and Physics, 92nd Edition*. CRC Press, 2011.
- [113] M. Kohagen, M. Brehm, Y. Lingscheid, R. Giernoth, J. Sangoro, F. Kremer, S. Naumov, C. Jacob, J. Krger, R. Valiullin, and B. Kirchner, “How hydrogen bonds influence the mobility of imidazolium-based ionic liquids. A combined theoretical and experimental study of 1-*n*-butyl-3-methylimidazolium bromide,” *The Journal of Physical Chemistry B*, vol. 115, no. 51, pp. 15280 – 15288, 2011.
- [114] K. Fujii, T. Fujimori, T. Takamuku, R. Kanzaki, Y. Umebayashi, and S. Ishiguro, “Conformational equilibrium of bis(trifluoromethanesulfonyl) imid anion of a room-temperature ionic liquid: Raman spectroscopic study and DFT calculations,” *The Journal of Physical Chemistry B*, vol. 110, no. 16, pp. 8179 – 8183, 2006.
- [115] L. J. Goujon, A. Khaldi, A. Maziz, C. Plesse, G. T. M. Nguyen, P.-H. Aubert, F. Vidal, C. Chevrot, and D. Teyssié, “Flexible solid polymer electrolytes based on nitrile butadiene rubber/poly(ethylene oxide) interpenetrating polymer networks containing either LiTFSI or EMITFSI,” *Macromolecules*, vol. 44, no. 24, pp. 9683 – 9691, 2011.
- [116] A. Jarosik, S. Krajewski, A. Lewandowski, and P. Radzinski, “Conductivity of ionic liquids in mixtures,” *Journal of Molecular Liquids*, vol. 123, pp. 43 – 50, Jan. 2006.
- [117] R. M. Fuoss and C. A. Kraus, “Properties of electrolytic solutions. IV. The conductance minimum and the formation of triple ions due to the action of Coulomb forces,” *Journal of the American Chemical Society*, vol. 55, no. 6, pp. 2387 – 2399, 1933.

- [118] D. W. McCall and D. C. Douglass, “The effect of ions on the self-diffusion of water. Ionic concentration dependence,” *The Journal of Physical Chemistry*, vol. 69, no. 6, pp. 2001 – 2011, 1965.
- [119] H. Palza, P. A. Zapata, and C. Angulo-Pineda, “Electroactive smart polymers for biomedical applications,” *Materials*, vol. 12, no. 2, 2019.
- [120] P. G. de Gennes, K. Okumura, M. Shahinpoor, and K. J. Kim, “Mechanoelectric effects in ionic gels,” *Europhysics Letters (EPL)*, vol. 50, pp. 513 – 518, May 2000.
- [121] S. M. Villa, V. M. Mazzola, T. Santaniello, E. Locatelli, M. Maturi, L. Migliorini, I. Monaco, C. Lenardi, M. Comes Franchini, and P. Milani, “Soft piezoionic/piezoelectric nanocomposites based on ionogel/BaTiO<sub>3</sub> nanoparticles for low frequency and directional discriminative pressure sensing,” *ACS Macro Letters*, vol. 8, no. 4, pp. 414 – 420, 2019.
- [122] Y. Dobashi, “Characterization of ionic polymers: towards applications as soft sensors in medicine,” MASC, University of British Columbia, 2016.
- [123] K. Paduszyński and U. Domańska, “Viscosity of ionic liquids: An extensive database and a new group contribution model based on a feed-forward artificial neural network,” *Journal of Chemical Information and Modeling*, vol. 54, no. 5, pp. 1311 – 1324, 2014.
- [124] K. Dokko, D. Watanabe, Y. Ugata, M. L. Thomas, S. Tsuzuki, W. Shinoda, K. Hashimoto, K. Ueno, Y. Umebayashi, and M. Watanabe, “Direct evidence for Li ion hopping conduction in highly concentrated sulfolane-based liquid electrolytes,” *The Journal of Physical Chemistry B*, vol. 122, no. 47, pp. 10736 – 10745, 2018.

- [125] P. Shi, M. Lin, H. Zheng, X. He, Z. Xue, H. Xiang, and C. Chen, "Effect of propylene carbonate-Li<sup>+</sup> solvation structures on graphite exfoliation and its application in Li-ion batteries," *Electrochimica Acta*, vol. 247, pp. 12 – 18, 2017.
- [126] Z. Wang, W. Gao, X. Huang, Y. Mo, and L. Chen, "Spectroscopic studies on interactions and microstructures in propylene carbonate–LiTFSI electrolytes," *Journal of Raman Spectroscopy*, vol. 32, no. 11, pp. 900 – 905, 2001.
- [127] A. Martinelli, A. Matic, P. Jacobsson, L. Börjesson, A. Fernicola, and B. Scrosati, "Phase behavior and ionic conductivity in lithium bis(trifluoromethanesulfonyl)imide-doped ionic liquids of the pyrrolidinium cation and bis(trifluoromethanesulfonyl)imide anion," *The Journal of Physical Chemistry B*, vol. 113, no. 32, pp. 11247 – 11251, 2009.
- [128] P. Meister, V. Siozios, J. Reiter, S. Klamor, S. Rothermel, O. Fromm, H.-W. Meyer, M. Winter, and T. Placke, "Dual-ion cells based on the electrochemical intercalation of asymmetric fluorosulfonyl-(trifluoromethanesulfonyl) imide anions into graphite," *Electrochimica Acta*, vol. 130, pp. 625 – 633, 2014.
- [129] X. Qi, B. Blizanac, A. DuPasquier, P. Meister, T. Placke, M. Oljaca, J. Li, and M. Winter, "Investigation of PF<sub>6</sub><sup>-</sup> and TFSI<sup>-</sup> anion intercalation into graphitized carbon blacks and its influence on high voltage lithium ion batteries," *Phys. Chem. Chem. Phys.*, vol. 16, pp. 25306 – 25313, 2014.
- [130] R.-S. Kühnel and A. Balducci, "Lithium ion transport and solvation in *N*-butyl-*N*-methylpyrrolidinium bis(trifluoromethanesulfonyl)imidepropylene carbonate mixtures," *The Journal of Physical Chemistry C*, vol. 118, no. 11, pp. 5742 – 5748, 2014.

- [131] Y. Ikezawa and T. Ariga, “*In situ* FTIR spectra at the Cu electrode/propylene carbonate solution interface,” *Electrochimica Acta*, vol. 52, no. 7, pp. 2710 – 2715, 2007.
- [132] E. Gileadi and E. Kirowa-Eisner, “Electrolytic conductivity—the hopping mechanism of the proton and beyond,” *Electrochimica Acta*, vol. 51, no. 27, pp. 6003 – 6011, 2006.
- [133] O. Markovitch and N. Agmon, “Structure and energetics of the hydronium hydration shells,” *The Journal of Physical Chemistry A*, vol. 111, no. 12, pp. 2253 – 2256, 2007.
- [134] M. Park, X. Zhang, M. Chung, G. B. Less, and A. M. Sastry, “A review of conduction phenomena in Li-ion batteries,” *Journal of Power Sources*, vol. 195, no. 24, pp. 7904 – 7929, 2010.
- [135] M. Schumaker and R. MacKinnon, “A simple model for multi-ion permeation. Single-vacancy conduction in a simple pore model,” *Biophysical Journal*, vol. 58, no. 4, pp. 975 – 984, 1990.
- [136] K.-D. Kreuer, “Proton conductivity: Materials and applications,” *Chemistry of Materials*, vol. 8, no. 3, pp. 610 – 641, 1996.
- [137] Y. Noda, K. Nakano, H. Takeda, M. Kotobuki, L. Lu, and M. Nakayama, “Computational and experimental investigation of the electrochemical stability and Li-ion conduction mechanism of  $\text{LiZr}_2(\text{PO}_4)_3$ ,” *Chemistry of Materials*, vol. 29, no. 21, pp. 8983 – 8991, 2017.
- [138] O. Gerbig, R. Merkle, and J. Maier, “Electron and ion transport in  $\text{Li}_2\text{O}_2$ ,” *Advanced Materials*, vol. 25, no. 22, pp. 3129 – 3133, 2013.

- [139] H. Mehrer, *Diffusion in Solids: Fundamentals, Methods, Materials, Diffusion-Controlled Processes*. Springer Series in Solid-State Sciences, Springer Berlin Heidelberg, 2007.
- [140] Y. Ugata, M. L. Thomas, T. Mandai, K. Ueno, K. Dokko, and M. Watanabe, “Li-ion hopping conduction in highly concentrated lithium bis(fluorosulfonyl)amide/dinitrile liquid electrolytes,” *Phys. Chem. Chem. Phys.*, vol. 21, pp. 9759 – 9768, 2019.
- [141] Y.-S. Hu, H. Li, X. Huang, and L. Chen, “Novel room temperature molten salt electrolyte based on LiTFSI and acetamide for lithium batteries,” *Electrochemistry Communications*, vol. 6, pp. 28 – 32, Jan. 2004.
- [142] S. Campbell, C. Bowes, and R. McMillan, “The electrochemical behaviour of tetrahydrofuran and propylene carbonate without added electrolyte,” *Journal of Electroanalytical Chemistry and Interfacial Electrochemistry*, vol. 284, no. 1, pp. 195 – 204, 1990.
- [143] A. Peters and N. R. Branda, “Electrochromism in photochromic dithienylcyclopentenes,” *Journal of the American Chemical Society*, vol. 125, no. 12, pp. 3404 – 3405, 2003.
- [144] N. Branda, G. Brenner, J. Finden, S. Gauthier, B. Gillon, A. Koutsandreas, V. Marshman, M. Pilapil, J. Sargent, J. Daniel, *et al.*, “Switching materials, and compositions and methods for making same,” 2013. Patent WO2013152425 A1.
- [145] A. Peters, R. McDonald, and N. R. Branda, “Regulating  $\pi$ - $\pi$ conjugated pathways using a photochromic 1,2-dithienylcyclopentene,” *Chem. Commun.*, pp. 2274 – 2275, 2002.

- [146] J. E. D. Bene, P. F. Provasi, I. Alkorta, and J. Elguero, “Resolving an apparent discrepancy between theory and experiment: spin-spin coupling constants for FCCF,” *Magnetic Resonance in Chemistry*, vol. 46, no. 11, pp. 1003 – 1006, 2008.
- [147] M. D. Mohammadi and M. Hamzehloo, “Densities, viscosities, and refractive indices of binary and ternary mixtures of methanol, acetone, and chloroform at temperatures from (298.15 - 318.15) K and ambient pressure,” *Fluid Phase Equilibria*, vol. 483, pp. 14 – 30, 2019.
- [148] L. H. Hess and A. Balducci, “1,2-butylene carbonate as solvent for EDLCs,” *Electrochimica Acta*, vol. 281, pp. 437 – 444, 2018.
- [149] J. Mazurkiewicz and P. Tomasik, “Effect of external electric field upon charge distribution, energy and dipole moment of selected monosaccharide molecules,” *Natural Science*, vol. 04, Jan. 2012.
- [150] A. Ghoufi, K. Benhamed, L. Boukli-Hacene, and G. Maurin, “Electrically induced breathing of the MIL-53(Cr) metal-organic framework,” *ACS Central Science*, vol. 3, no. 5, pp. 394 – 398, 2017.
- [151] S. Namsani and A. O. Yazaydin, “Electric field induced rotation of halogenated organic linkers in isoreticular metalorganic frameworks for nanofluidic applications,” *Mol. Syst. Des. Eng.*, vol. 3, pp. 951 – 958, 2018.
- [152] A. Hirao and H. Nishizawa, “Effect of dipoles on carrier drift and diffusion of molecularly doped polymers,” *Phys. Rev. B*, vol. 56, pp. R2904 – R2907, Aug. 1997.
- [153] S. H. Northrup, J. D. Smith, J. O. Boles, and J. C. L. Reynolds, “The effect of dipole moment on diffusion controlled bimolecular reaction rates,” *The Journal of Chemical Physics*, vol. 84, no. 10, pp. 5536 – 5544, 1986.

- [154] T. C. Chan, H. T. Li, and K. Y. Li, “Effects of shapes of solute molecules on diffusion: A study of dependences on solute size, solvent, and temperature,” *The Journal of Physical Chemistry B*, vol. 119, no. 51, pp. 15718 – 15728, 2015.
- [155] L. Lebreton, B. Slat, F. Ferrari, B. Sainte-Rose, J. Aitken, R. Marthouse, S. Hajbane, S. Cunsolo, A. Schwarz, A. Levivier, K. Noble, P. Debeljak, H. Maral, R. Schoeneich-Argent, R. Brambini, and J. Reisser, “Evidence that the great pacific garbage patch is rapidly accumulating plastic,” *Scientific Reports*, vol. 8, no. 1, p. 4666, 2018.
- [156] R. Geyer, J. R. Jambeck, and K. L. Law, “Production, use, and fate of all plastics ever made,” *Science Advances*, vol. 3, no. 7, 2017.
- [157] D. Montarnal, M. Capelot, F. Tournilhac, and L. Leibler, “Silica-like malleable materials from permanent organic networks,” *Science*, vol. 334, no. 6058, pp. 965 – 968, 2011.
- [158] M. Capelot, D. Montarnal, F. Tournilhac, and L. Leibler, “Metal-catalyzed transesterification for healing and assembling of thermosets,” *Journal of the American Chemical Society*, vol. 134, no. 18, pp. 7664 – 7667, 2012.
- [159] Y. Yang, S. Zhang, X. Zhang, L. Gao, Y. Wei, and Y. Ji, “Detecting topology freezing transition temperature of vitrimers by AIE luminogens,” *Nature Communications*, vol. 10, no. 1, p. 3165, 2019.
- [160] W. Denissen, M. Droesbeke, R. Nicolaÿ, L. Leibler, J. M. Winne, and F. E. Du Prez, “Chemical control of the viscoelastic properties of vinylogous urethane vitrimers,” *Nature communications*, vol. 8, pp. 1 – 7, Mar. 2017.

- [161] J. Peng, X. He, K. Wang, W. Tan, Y. Wang, and Y. Liu, “Noninvasive monitoring of intracellular pH change induced by drug stimulation using silica nanoparticle sensors,” *Analytical and Bioanalytical Chemistry*, vol. 388, no. 3, pp. 645 – 654, 2007.
- [162] T. Stukenbroeker, W. Wang, J. M. Winne, F. E. Du Prez, R. Nicolaÿ, and L. Leibler, “Polydimethylsiloxane quenchable vitrimers,” *Polym. Chem.*, vol. 8, pp. 6590 – 6593, 2017.
- [163] R. Baruah, A. Kumar, R. R. Ujjwal, S. Kedia, A. Ranjan, and U. Ojha, “Recyclable thermosets based on dynamic amidation and aza-Michael addition chemistry,” *Macromolecules*, vol. 49, no. 20, pp. 7814 – 7824, 2016.
- [164] K. S. Kwan, C. N. Subramaniam, and T. C. Ward, “Effect of penetrant size and shape on its transport through a thermoset adhesive: I. *n*-alkanes,” *Polymer*, vol. 44, no. 10, pp. 3061 – 3069, 2003.
- [165] L. Rovigatti, G. Nava, T. Bellini, and F. Sciortino, “Self-dynamics and collective swap-driven dynamics in a particle model for vitrimers,” *Macromolecules*, vol. 51, no. 3, pp. 1232 – 1241, 2018.
- [166] R. G. C. Arridge, *An Introduction to Polymer Mechanics*. Taylor and Francis, 1985.
- [167] S. Blonski, W. Brostow, and J. Kubat, “Molecular dynamics simulations of stress relaxation in metals and polymers,” *Phys. Rev. B*, vol. 49, pp. 6494 – 6500, 1994.
- [168] G. Zhu, H. Rezvantlab, E. Hajizadeh, X. Wang, and R. G. Larson, “Stress-gradient-induced polymer migration: Perturbation theory and comparisons to stochastic simulations,” *Journal of Rheology*, vol. 60, no. 2, pp. 327 – 343, 2016.

- [169] W. Hong, X. Zhao, J. Zhou, and Z. Suo, “A theory of coupled diffusion and large deformation in polymeric gels,” *Journal of the Mechanics and Physics of Solids*, vol. 56, no. 5, pp. 1779 – 1793, 2008.
- [170] J. R. White, “On internal stress and activation volume in polymers,” *Journal of Materials Science*, vol. 16, pp. 3249 – 3262, Dec. 1981.
- [171] W. Brostow and R. Corneliusen, *Failure of Plastics*. Hanser Pub., 1986.
- [172] M. J. C. Plancha, *Characterisation and modelling of multivalent polymer electrolytes*. Woodhead Publishing, 2010.
- [173] F. Rittig, J. Kärger, C. M. Papadakis, G. Fleischer, P. Štěpánek, and K. Almdal, “Self-diffusion investigations on a series of PEP-PDMS diblock copolymers with different morphologies by pulsed field gradient NMR,” *Phys. Chem. Chem. Phys.*, vol. 1, pp. 3923 – 3931, 1999.
- [174] W. H. Binder, “The labile chemical bond: A perspective on mechanochemistry in polymers,” *Polymer*, vol. 202, p. 122639, 2020.
- [175] X. Hu, T. Zeng, C. C. Husic, and M. J. Robb, “Mechanically triggered small molecule release from a masked furfuryl carbonate,” *Journal of the American Chemical Society*, vol. 141, no. 38, pp. 15018 – 15023, 2019. PMID: 31515994.

## Appendix A

# Vitrimer Sample Preparation

Vitrimers samples were prepared by Taylor D. Wright of Dr. Michael Wolf's lab at UBC in order to measure the diffusion of NMR visible tag molecules that are attached to the crosslinker of the vitrimer samples. The preparation involved four main steps:

1. Preparation of an exchangeable NMR visible tags 2,2,2-Trifluoroethylacetoacetate.

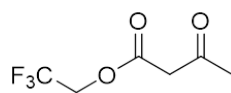


Figure A.1: 2,2,2-Trifluoroethylacetoacetate.

Trifluoroethanol (3.7 mL, 50 mmol), *m*-xylene, and 2,2,6-Trimethyl-1,3-dioxin-4-one (4.7 mL, 33 mmol) were added to an open vial and heated to 150 °C while stirring. The reaction was kept at 150 °C for thirty minutes, and then cooled to room temperature. The mixture was transferred to a 50 mL round-bottom flask and dried under vacuum. The crude oil was purified using column chromatography on silica gel with 3:1 petroleum ether to diethyl ether as the mobile phase.

2. Preparation of vinylogous urethane crosslinker (VitCL).

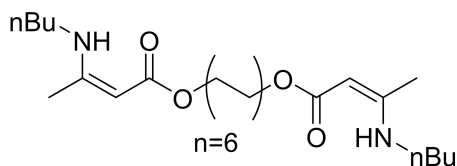


Figure A.2: 1,12-dodecane-bis- $\beta$ -ketoenamine *n*-butyl

1,12-dodecane-bis- $\beta$ -ketoenamine *n*-butyl was prepared by condensing 1,12-dodecanebisacetoacetate [5] with *n*-butylamine. 1 g, 2.7 mmol and 0.8 mL, 8.1 mmol, respectively, were added to 7 mL of THF in a 25 mL round bottom flask along with an excess of anhydrous magnesium sulfate. The system was equipped with a magnetic stir bar and condenser and allowed to reflux for three hours. The mixture was cooled, vacuum filtered, and rinsed with DCM. The eluent was dried under vacuum and then extracted using DCM and water. The organic layer was dried over anhydrous magnesium sulfate, filtered, and then dried to a pale clear oil.

3. Preparation of an exchangeable coloured, NMR visible tags.

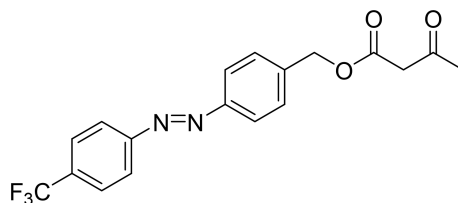


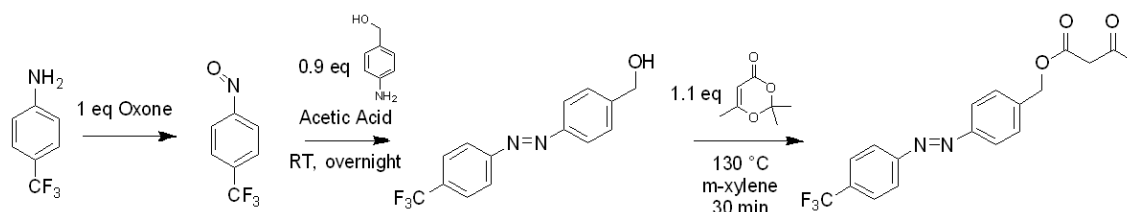
Figure A.3: 4-trifluoromethyl-4'-methylacetoacetate azobenzene

4-trifluoromethyl-4'-methylacetoacetate azobenzene an F labelled, blue light-absorbing dye was prepared by a three-step synthesis with a starting material 3-(Trifluoromethyl)aniline. A schematics of this synthesis can be seen in scheme A.1. 3-(Trifluoromethyl)aniline was reacted with 1 molar equivalent of Oxone to give the nitroso compound. To this, 0.9 equivalents of 4-aminobenzyl alcohol was added under acidic conditions and reacted at room temperature overnight. The resulting azobenzene molecule was purified, and then reacted with 1.1 molar equivalents of the acetone diketene adduct in *m*-xylenes at 130 °C for 30 minutes. The product was purified using silica gel chromatography to afford the fluorine labelled acetoacetate azobenzene.

4. Preparation of polymer network.

PDMS-NH<sub>2</sub> (1 g, 0.02 mmol), 38 mg of exchangeable vinylogous urethane crosslinker or

## Appendix A. Vitriimer Sample Preparation



Scheme A.1: Synthesis steps for the preparation of fluorine labelled acetoacetate azobenzene. This molecule functions as an exchangeable tag that is both NMR visible (due to the presence of a  $\text{CF}_3$  group) and is both visible to the naked eye (due to the azobenzene group blue light absorbing properties). Synthesis steps were planned and performed by collaborator Taylor D. Wright of UBC.

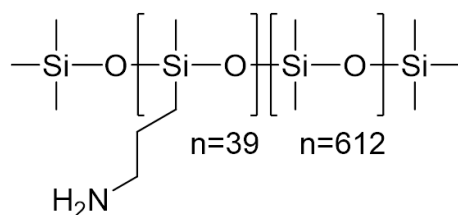


Figure A.4: PDMS- $\text{NH}_2$  polymer structure

23 mg of triethylene glycol dimethacrylate (0.08 mmol, 4 eq) or a non-exchangeable triethylene glycol dimethacrylate, *p*-toluenesulfonic acid (0.67 mg, 0.5 mol relative to moles of  $\text{NH}_2$ , as a dilute solution in THF), 5 molar equivalents of an NMR visible tag, and 2.5 mL of THF were combined in a 20 mL vial and stirred using a magnetic stir bar for 5 minutes. The mixture was found to gel rapidly if the bisacetoacetate was used directly, and as such the vinylogous urethane VitCL compound was used. The vial was degassed using a sonicator for 10 minutes, and the solution transferred to a silicone mold inside of a glass desiccator. The system was placed under  $\text{N}_2$ , covered in aluminum foil, and heated to  $60^\circ\text{C}$  using an oil bath until the THF had fully evaporated. The system was then heated at  $100^\circ\text{C}$  for 18 hours under  $\text{N}_2$ .

Polymer samples were removed from the warm molds and stored in a refrigerator when not in use.